

T.R.
ERCIYES UNIVERSITY
GRADUATE SCHOOL OF NATURAL AND APPLIED SCIENCES
DEPARTMENT OF PHYSICS

**THE SYNTHESIS OF $(\text{Bi}_2\text{O}_3)_{1-x-y-z}(\text{Dy}_2\text{O}_3)_x(\text{Eu}_2\text{O}_3)_y$
 $(\text{Tm}_2\text{O}_3)_z$ ELECTROLYTE OF THE SOLID OXIDE FUEL
CELL BY SOLID STATE REACTION**

Prepared by
Mustafa ALDORRI

Supervisor
Prof. Dr. Ayhan GÜLDESTE

M. Sc. Thesis

December 2017
KAYSERİ

T.R.
ERCIYES UNIVERSITY
GRADUATE SCHOOL OF NATURAL AND APPLIED SCIENCES
DEPARTMENT OF PHYSICS

**THE SYNTHESIS OF $(\text{Bi}_2\text{O}_3)_{1-x-y-z}(\text{Dy}_2\text{O}_3)_x(\text{Eu}_2\text{O}_3)_y$
 $(\text{Tm}_2\text{O}_3)_z$ ELECTROLYTE OF THE SOLID OXIDE FUEL
CELL BY SOLID STATE REACTION**

Prepared by
Mustafa ALDORRI

Supervisor
Prof. Dr. Ayhan GÜLDESTE

M. Sc. Thesis

December 2017
KAYSERİ

COMPLIANCE WITH SCIENTIFIC ETHICS

I hereby declare that all information in this document has been obtained and presented in accordance with academic rules and ethical conduct. I also declare that, as required by these rules and conduct, I have fully cited and referenced all material and results that are not original to this work.



Owner of thesis

MUSTAFA ALDORRI

SUITABILITY FOR GUIDE

The MS thesis entitled '**The synthesis of $(\text{Bi}_2\text{O}_3)_{1-x-y-z}(\text{Dy}_2\text{O}_3)_x(\text{Eu}_2\text{O}_3)_y(\text{Tm}_2\text{O}_3)_z$ electrolyte of the solid oxide fuel cell by solid state reaction**' has been prepared in accordance with Erciyes University Graduate Education and Teaching Institute Thesis Preparation and Writing Guide.



Student

Mustafa ALDORRI



Supervisor

Prof. Dr. Ayhan GULDESTE



Head of the Department of Physics

Prof. Dr. Mustafa GENÇASLAN

ACCEPTANCE AND APPROVAL PAGE

This study entitled 'The synthesis of $(\text{Bi}_2\text{O}_3)_{1-x-y-z} (\text{Dy}_2\text{O}_3)_x (\text{Eu}_2\text{O}_3)_y (\text{Tm}_2\text{O}_3)_z$ electrolyte of the solid oxide fuel cell by solid state reaction' Prepared by Mustafa ALDOORI under the supervision of Prof. Dr. Ayhan GULDESTE was accepted by the jury as MSc. thesis in physics department.

26/12/2017

JURY:

Supervisor : Prof. Dr. Ayhan GÜLDESTE



Juror

Prof. Dr. Mehmet ARI



Juror

Doc. Dr. Erhan KARAKÖSE



APPROVAL:

That the acceptance of this thesis has been approved by the decision of the Institute's Board of Directors with the 26/12/2017 date and 2017/55-33 numbered decision.


26/12/2017

Prof. Dr. Mehmet AKKURT

Director of Institute
Director of Institute

ACKNOWLEDGEMENTS

First, I would like to thank Allah so much, for having made everything possible by giving me strength and courage to do this work.

I offer my deepest respect and gratitude to my supervisor **Prof. Dr. Ayhan Guldeste** for his time, patience, and support during the development of this project and I would like to express my sincere thanks to **Prof. Dr. Mehmet Ari** for his time, teaching and advising most important things, it has been an honor for me to work with him. **And** I'm grateful the good brother **Dr. Yasin Polat** for helping me in my experience.

I would like to extend my thanks to the Government and the people of Turkey for their hospitality, generosity and a very good handling with me.

Finally, I would like to extend my thanks to my parents, my wife, my children and all friends.

Mustafa ALDORRI

December 2017, KAYSERİ

**THE SYNTHESIS OF $(\text{Bi}_2\text{O}_3)_{1-x-y-z}(\text{Dy}_2\text{O}_3)_x(\text{Eu}_2\text{O}_3)_y(\text{Tm}_2\text{O}_3)_z$ ELECTROLYTE
OF THE SOLID OXIDE FUEL CELL BY SOLID STATE REACTION**

Mustafa ALDORRI

**Erciyes University, Graduate School of Natural and Applied Sciences
M.Sc. Thesis, December 2017
Supervisor: Prof. Dr. Ayhan GÜLDESTE**

ABSTRACT

In this study, $(\text{Bi}_2\text{O}_3)_{1-x-y-z}(\text{Dy}_2\text{O}_3)_x(\text{Eu}_2\text{O}_3)_y(\text{Tm}_2\text{O}_3)_z$ ($x, y, z = 0.05, 0.10, 0.15, 0.20$) quaternary system solid electrolyte materials were synthesized in the atmospheric conditions by solid-state reaction and structural, thermal and conductivity properties has been studied for ten different compositions.

X-Ray diffraction analysis of the as-sintered (at 750 °C) samples indicated that cubic fcc $\delta\text{-Bi}_2\text{O}_3$ phase is formed with together small amount of monoclinic $\alpha\text{-Bi}_2\text{O}_3$ phase. After electrical conductivity measurement, $\alpha\text{-Bi}_2\text{O}_3$ phase turned into $\delta\text{-Bi}_2\text{O}_3$ phase. This phase transition clearly was detected from DTA spectrums and conductivity measurement curves at about 750 °C for some samples. DTA spectrum also reveals that cubic $\delta\text{-Bi}_2\text{O}_3$ phase is stable during cooling process from 900 °C to room temperature. This indicates that doping makes cubic $\delta\text{-Bi}_2\text{O}_3$ phase stable.

The highest electrical conductivity of $0.62 (\Omega\cdot\text{cm})^{-1}$ at 750 °C was measured for composition of $(\text{Bi}_2\text{O}_3)_{0.85}(\text{Dy}_2\text{O}_3)_{0.05}(\text{Eu}_2\text{O}_3)_{0.05}(\text{Tm}_2\text{O}_3)_{0.05}$. It has been observed that electrical conductivity decreases with increasing concentration of doped materials. However, the electrical conductivity obtained for low dopant concentration at 750 °C is comparable with conductivity of pure $\delta\text{-Bi}_2\text{O}_3$ ($\sim 1 \Omega^{-1}\cdot\text{cm}^{-1}$ at 650 °C).

Keywords: Solid oxide fuel cell (SOFC), electrolyte, Bismuth Oxide (Bi_2O_3), ionic conductivity

**(Bi₂O₃)_{1-x-y-z} (Dy₂O₃)_x (Eu₂O₃)_y (Tm₂O₃)_z KATI OKSİT YAKIT PİLİ
ELEKTROLİT'İN KATIHAL REAKSİYONU İLE SENTEZLENMESİ**

Mustafa ALDORRI

**Erciyes Üniversitesi, Fen Bilimleri Enstitüsü
Yüksek Lisans Tezi Aralık 2017
Tez Danışmanı: Prof. Dr. Ayhan GÜLDESTE**

ÖZET

Bu çalışmada, (Bi₂O₃)_{1-x-y-z} (Dy₂O₃)_x (Eu₂O₃)_y (Tm₂O₃)_z (x, y, z= 0.05, 0.10, 0.15, 0.20) dördü sistem katı elektrolit malzemeler atmosferik ortamda katıhal reaksiyonu tekniği ile sentezlendi ve yapısal, termal ve iletkenlik özellikleri on farklı kompozisyon için incelendi.

X-Ray difraksiyon analizleri, 750 °C de ısıl işleme tabi tutulmuş haliyle numunelerde az miktarda mono klinik α-Bi₂O₃ fazı ile beraber kübik fcc δ-Bi₂O₃ fazının oluştuğunu gösterdi. Elektriksel iletkenlik ölçümünden sonra α-Bi₂O₃ fazı da, δ-Bi₂O₃ fazına dönüştü. Bu faz geçişi bazı numuneler için Diferansiyel Termal Analiz (DTA) spektrumunda ve iletkenlik ölçüm eğrilerinde 750 °C civarında açık olarak tespit edildi. DTA spektrumu ayrıca, kübik δ-Bi₂O₃ fazının 900 °C den oda sıcaklığına soğuması esnasında kararlı olduğunu gösterdi. Bu, katkılamanın kübik δ-Bi₂O₃ fazını kararlı hale getirdiğini gösterir.

750°C de en yüksek elektriksel iletkenlik 0.62 (Ω.cm)⁻¹ büyüklüğünde, (Bi₂O₃)_{0.85} (Dy₂O₃)_{0.05} (Eu₂O₃)_{0.05} (Tm₂O₃)_{0.05} kompozisyonunda ölçüldü. Elektriksel iletkenliğin artan katkı maddesi konsantrasyonu ile azaldığı gözlemlendi. Bununla beraber, düşük katkı konsantrasyonu için 750 °C de elde edilmiş elektriksel iletkenlik saf δ-Bi₂O₃ fazının elektriksel iletkenliği (~1 Ω⁻¹.cm⁻¹ at 650 °C) ile mukayese edilebilir mertebededir.

Anahtar Kelimeler: Katı oksit yakıt pilleri (KOYP), elektrolit, Bizmut oksit (Bi₂O₃),
iyonik iletkenlik

CONTENTS

THE SYNTHESIS OF $(\text{Bi}_2\text{O}_3)_{1-x-y-z} (\text{Dy}_2\text{O}_3)_x (\text{Eu}_2\text{O}_3)_y (\text{Tm}_2\text{O}_3)_z$ ELECTROLYTE OF THE SOLID OXIDE FUEL CELL BY SOLID STATE REACTION

COMPLIANCE WITH SCIENTIFIC ETHICS.....	i
SUITABILITY FOR GUIDE.....	ii
ACCEPTANCE AND APPROVAL PAGE	iii
ACKNOWLEDGEMENTS	iv
ABSTRACT.....	v
ÖZET.....	vi
CONTENTS.....	vii
LIST OF SYMBOLS AND ABBREVIATIONS	x
LIST OF FIGURES	xi
LIST OF TABLES	xiv

CHAPTER 1

INTRODUCTION

1.1. General Information.....	1
1.2. Fuel Cells.....	2
1.3. Development of Fuel Cells and Today.....	4

CHAPTER 2

GENERAL INFORMATION AND PREVIOUS STUDIES

2.1. Fuel cell Structure, Advantages of the fuel cell and Working Principle.....	8
2.1.1. Application Areas of Fuel cells.....	10
2.1.2. Fuel Types	10
2.1.3. Electrolyte for solid oxide fuel cell.....	12

2.1.4. Bi ₂ O ₃ based electrolyte	13
2.1.5. Solid state reaction	14
2.1.6. Bi ₂ O ₃ crystal structure	15
2.1.7. Bi ₂ O ₃ type electrolytes and their properties.....	17
2.1.8. Synthesizing and stabilizing the phase of pure Bi ₂ O ₃	20
2.1.9. Used chemicals	22
2.1.9.1. Bismuth trioxide (Bi ₂ O ₃)	22
2.1.9.2. Europium trioxide (Eu ₂ O ₃)	24
2.1.9.3. Thulium trioxide (Tm ₂ O ₃).....	25
2.1.9.4. Dysprosium trioxide (Dy ₂ O ₃)	26
2.2. Previous studies	27

CHAPTER 3

MATERIALS AND METHODS

3.1. Preparation of samples	32
3.2. Differential Thermal and Thermogravimetric Analysis (DTA/TG)	36
3.3. X-Ray Powder Diffraction.....	37
3.4. Four Points D.C. Conductivity Measurement System.....	37
3.4.1. Calculation of Activation Energy	40

CHAPTER 4

CHARACTERIZATION OF ELECTROLYTES

4.1. (Bi ₂ O ₃) _{1-x-y-z} (Dy ₂ O ₃) _x (Eu ₂ O ₃) _y (Tm ₂ O ₃) _z Quaternary System.....	43
4.1.1. X-Ray Analysis	44
4.1.2. Thermal Analysis.....	58
4.1.3. Electrical conductivity	64
4.1.4. Calculation of Activation Energies	72
4.2. Conclusion.....	79

CHAPTER 5

CONCLUSION AND FUTURE WORKS 80
REFERENCE 82
CURRICULUM VITAE..... 89



LIST OF SYMBOLS AND ABBREVIATIONS

Å	: Unit of length used chiefly in measuring wavelengths of light
AFB	: Alkaline fuel batteries
DBFP	: Direct Boriding Fuel Pump
DEFC	: Direct Ethanol Fuel Chiller
DFAFO	: Direct Formic Acid Fuel Oil
DMFO	: Direct Methanol Fuel Oil
DTA/TG	: Differential thermal analysis / thermal gravimetry
Ea	: Activation energy
EGFP	: Electro-Galvanic Fuel Pipe
FAFC	: Phosphoric acid fuel cells
FC	: Fuel cell
kW	: Kilowatt
MCFB	: Molten carbonate fuel batteries
MFP	: Microbial Fuel Pilot
MHFP	: Metal Hydride Fuel Pipe
°C	: Celsius centigrade temperature
PAFC	: Phosphoric acid fuel cell
PEMFC	: Proton exchange membrane fuel cells
SEM	: scanning electron microscope
SOFC	: Solid oxide fuel cell
SOPF	: Solid Oxide Fuel Pump
XRD	: X-rays powder diffraction

LIST OF FIGURES

Figure 1.1. Fuel cell and cell components.....	3
Figure 1.2. Mond and Langer's fuel cell.....	4
Figure 1.3. Proton exchange membrane (PEM) fuel used in Gemini spacecraft	5
Figure 2.1. Fuel cell principles.....	8
Figure 2.2. Advantages of fuel cell	9
Figure 2.3. Types of fuel pellets.....	12
Figure 2.4. a) Projection of the structure on the xz-plane b) Projection of the structure, as given by sillen, on the xz-plane.....	15
Figure 2.5. The oxygen layer at $x= 0.25$ projected along x on the yz -plane of four unit cells. The bismuth atoms on each side of the layer are also plotted. The oxygen pattern is illustrated with single lines, while the Bi-O bonds have triple line design	16
Figure 2.6. Phase transformation temperature diagram for Bi_2O_3	18
Figure 2.7. (a) Fluorite (CaF_2), crystal braids.....	19
Figure 2.8. Crystal structure of pure Bi_2O_3	23
Figure 2.9. Crystal structure of pure Eu_2O_3	24
Figure 2.10. Crystal structure of pure Tm_2O_3	25
Figure 2.11. Crystal structure of pure Dy_2O_3	26
Figure 3.1. Agate mortar	33
Figure 3.2. Furnaces used for solid state reactions	34
Figure 3.3 Alumina crucible.....	34
Figure 3.4. Images of the produced samples before and after heating.....	34
Figure 3.5. Manual hydraulic presses and some solid electrolyte materials sintered after packaging	35
Figure 3.6. Pressing of the sample	35
Figure 3.7. Image of the Perkin Elmer DTA/TG measurement system.....	36
Figure 3.8. The image of Bruker AXS D8 Advanced type powder diffract meter	37
Figure 3.9. Computer controlled electrical conductivity measurement system	38
Figure 3.10. Alumina conductivity measurement kit.....	39

Figure 3.11. Four Points D.C. Electrical Conductivity Measurement Technique	39
Figure 3.12. $\ln\sigma - 1/T$ Chart.....	41
Figure 3.13. Second Region $\ln\sigma - 1/T$ Graph	41
Figure 4.1. XRD patterns of $(\text{Bi}_2\text{O}_3)_{0.85} (\text{Dy}_2\text{O}_3)_{0.05} (\text{Eu}_2\text{O}_3)_{0.05} (\text{Tm}_2\text{O}_3)_{0.05}$ (sample M1), (A) Before electrical conductivity measurement (B) After electrical conductivity measurement.	45
Figure 4.2. XRD patterns of $(\text{Bi}_2\text{O}_3)_{0.80} (\text{Dy}_2\text{O}_3)_{0.05} (\text{Eu}_2\text{O}_3)_{0.05} (\text{Tm}_2\text{O}_3)_{0.10}$ (sample M2), (A) Before electrical conductivity measurement (B) After electrical conductivity measurement.	46
Figure 4.3. XRD patterns of $(\text{Bi}_2\text{O}_3)_{0.75} (\text{Dy}_2\text{O}_3)_{0.05} (\text{Eu}_2\text{O}_3)_{0.05} (\text{Tm}_2\text{O}_3)_{0.15}$ (sample M3), (A) Before electrical conductivity measurement (B) After electrical conductivity measurement.	47
Figure 4.4. XRD patterns of $(\text{Bi}_2\text{O}_3)_{0.70} (\text{Dy}_2\text{O}_3)_{0.05} (\text{Eu}_2\text{O}_3)_{0.05} (\text{Tm}_2\text{O}_3)_{0.20}$ (sample M4), (A) Before electrical conductivity measurement (B) After electrical conductivity measurement.	48
Figure 4.5. XRD patterns of $(\text{Bi}_2\text{O}_3)_{0.80} (\text{Dy}_2\text{O}_3)_{0.05} (\text{Eu}_2\text{O}_3)_{0.10} (\text{Tm}_2\text{O}_3)_{0.05}$ (sample M5), (A) Before electrical conductivity measurement (B) After electrical conductivity measurement.	49
Figure 4.6. XRD patterns of $(\text{Bi}_2\text{O}_3)_{0.75} (\text{Dy}_2\text{O}_3)_{0.05} (\text{Eu}_2\text{O}_3)_{0.15} (\text{Tm}_2\text{O}_3)_{0.05}$ (sample M6), (A) Before electrical conductivity measurement (B) After electrical conductivity measurement.	50
Figure 4.7. XRD patterns of $(\text{Bi}_2\text{O}_3)_{0.70} (\text{Dy}_2\text{O}_3)_{0.05} (\text{Eu}_2\text{O}_3)_{0.20} (\text{Tm}_2\text{O}_3)_{0.05}$ (sample M7), (A) Before electrical conductivity measurement (B) After electrical conductivity measurement.	51
Figure 4.8. XRD patterns of $(\text{Bi}_2\text{O}_3)_{0.80} (\text{Dy}_2\text{O}_3)_{0.10} (\text{Eu}_2\text{O}_3)_{0.05} (\text{Tm}_2\text{O}_3)_{0.05}$ (sample M8), (A) Before electrical conductivity measurement (B) After electrical conductivity measurement.	52
Figure 4.9. XRD patterns of $(\text{Bi}_2\text{O}_3)_{0.75} (\text{Dy}_2\text{O}_3)_{0.15} (\text{Eu}_2\text{O}_3)_{0.05} (\text{Tm}_2\text{O}_3)_{0.05}$ (sample M9), (A) Before electrical conductivity measurement (B) After electrical conductivity measurement.	53
Figure 4.10. XRD patterns of $(\text{Bi}_2\text{O}_3)_{0.70} (\text{Dy}_2\text{O}_3)_{0.20} (\text{Eu}_2\text{O}_3)_{0.05} (\text{Tm}_2\text{O}_3)_{0.05}$ (sample M10), (A) Before electrical conductivity measurement (B) After electrical conductivity measurement.	54

Figure 4.11. Comparison of XRD spectrum of sample M1-M4 with bismuth oxide (δ -Bi ₂ O ₃). (A) Before conductivity measurement. (B) After conductivity measurement.	55
Figure 4.12. Comparison of XRD spectrum of sample M1, M5-M7 with bismuth oxide (δ -Bi ₂ O ₃). (A) Before conductivity measurement. (B) After conductivity measurement.	56
Figure 4.13. Comparison of XRD spectrum of sample M1, M8-M10 with bismuth oxide (δ - Bi ₂ O ₃). (A) Before conductivity measurement. (B) After conductivity measurement.	57
Figure 4.14. DTA/TG spectrum for M1 (Sample Weight: 16.783 mg).	59
Figure 4.15. DTA/TG spectrum for M2 (Sample Weight: 10.044 mg).	59
Figure 4.16. DTA/TG spectrum for M3 (Sample Weight: 14.303 mg).	60
Figure 4.17. DTA/TG spectrum for M4 (Sample Weight: 8.314 mg).	60
Figure 4.18. DTA/TG spectrum for M5 (Sample Weight: 9.683 mg).	61
Figure 4.19. DTA/TG spectrum for M6 (Sample Weight: 8.753 mg).	61
Figure 4.20. DTA/TG spectrum for M7 (Sample Weight: 5.296 mg).	62
Figure 4.21. DTA/TG spectrum for M8 (Sample Weight: 13.556 mg).	62
Figure 4.22. DTA/TG spectrum for M9 (Sample Weight: 8.747 mg).	63
Figure 4.23. DTA/TG spectrum for M10 (Sample Weight: 5.727 mg).	63
Figure 4.24. Temperature dependence of the electrical conductivity for samples M1-M10 over heating cycles.	68
Figure 4.25. Overlapped plot of the temperature dependence of the electrical conductivity for samples (M1-M4) over heating cycles.	69
Figure 4.26. Overlapped plot of the temperature dependence of the electrical conductivity for samples M1 and M5-M7 over heating cycles.	70
Figure 4.27. Overlapped plot of the temperature dependence of the electrical conductivity for samples M1 and M8-M10 over heating cycles.	71
Figure 4.28. The Arrhenius plots of electrical conductivity at low and high temperature for sample M1-M10.	77

LIST OF TABLES

Table 2.1.	Differences between fuel cells	11
Table 2.2.	Interatomic distances D_1 (Å) and their estimated standard deviations in the structure of α -Bi ₂ O ₃ . The distances computed from the structure given by Sillén are listed under D_2	17
Table 2.3.	Ionic radii of some ions	22
Table 3.1.	Mole percentages and quantities of materials used in mixtures	32
Table 4.1.	The molar percentages of Dy ₂ O ₃ , Eu ₂ O ₃ , Tm ₂ O ₃ , and Bi ₂ O ₃ base materials	43
Table 4.2.	Electrical conductivity parameters of samples M1-M4 at about 750°C.	70
Table 4.3.	Electrical conductivity parameters of samples M1 and M5-7 at about 750°C.	71
Table 4.4.	Electrical conductivity parameters of samples M1 and M8-10 at about 750°C.....	72
Table 4.5.	Activation energies calculated for each sample at low temperatures.	78
Table 4.6.	Activation energies calculated for each sample at high temperatures.	78

CHAPTER 1

INTRODUCTION

1.1. General Information

In response to population growth and technological development in the world, depending on the demand for energy is increasing rapidly. Fossil fuels are the largest part of the world's energy needs today. As a result of the use of fossil fuels, environmental issues such as global warming, climate change, and the greenhouse effect are emerging due to the release of gases such as carbon dioxide, carbon monoxide, nitrogen oxides, methane, and sulfur dioxide. The most important effect of this is global warming. Fossil fuels are the biggest cause of natural disasters that have come to the fore as a result of global warming. In addition to rising energy demand, fossil energy reserves are also rapidly declining. Since the fact that these fossil fuels are likely to be consumed in the near future, the search for alternative energy has gained importance in science circles.

While mankind is looking for the most efficient and economical solutions to meet the ever-increasing need for energy throughout history, the belief that the energy source of the times and the future will be hydrogen-based fuels is increasing day by day. Surveys show that hydrogen is about three times more expensive than other fuels in current conditions, and its use as a common energy source will depend on cost-cutting technological developments in hydrogen production.

Approximately 97% of the energy consumed in vehicles and in aircraft is still met by oil-based sources. Parameters such as the environmental conditions and the circumstance condition affect the fuel density of the vehicle. The race to commercialize hydrogen-powered vehicles in the 19th century has created a very strong competitive

environment among countries such as China, Germany, Canada, Norway, S. Korea, Japan and the United States of America.

Automobile manufacturers are continuing to develop hydrogen-working polymers and solid oxide fuel cells that will provide traction for a variety of vehicles. Fuel cell systems are designed with the required energy in mind. The mechanical components in the fuel cell must consist of components that can respond quickly to sudden and slow energy production needs. This affects power density in a large way. These dynamics are important for residential and automotive applications. The fuel cell has a great potential to be applied to various industrial, transportation sectors and residential technologies.

Portable fuel cells can be used in electric vehicles or power sources due to their high energy production. This environmentally friendly, highly efficient energy source is limiting its widespread use due to its high costs with promising future. Nowadays, many companies such as transportation, white goods, power supply manufacturer all over the world have gone to investigate and apply this subject. It is inevitable that we encounter such applications in our daily life in the near future.

1.2. Fuel Cells

Conventional electricity generation systems first use the combustion reaction to convert the energy in the fuel to electricity. Fuel and oxidizer (oxygen) must be mixed thoroughly in order for the combustion reaction to take place efficiently. After that, a series of intermediate operations are required until the electricity is generated. Every intermediate operation leads to energy loss, thus reducing the efficiency.

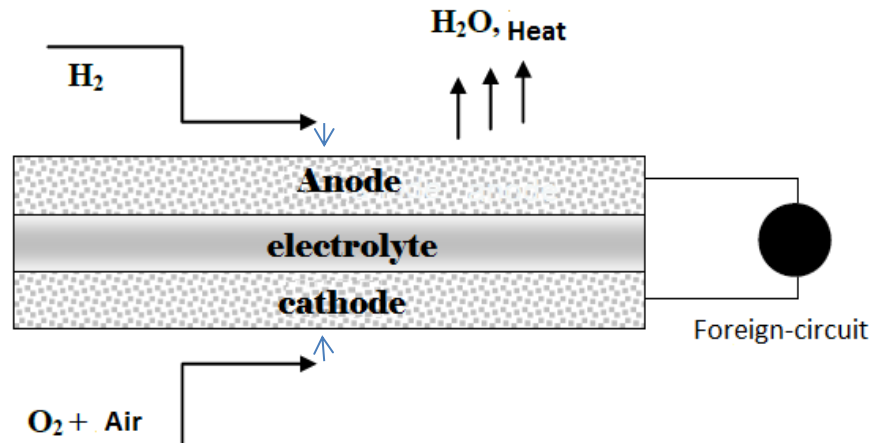


Figure 1.1. Fuel cell and cell components

In fuel cells, no combustion reaction or mechanical system is used and direct electrical energy is produced. Fuel cells are co-generation systems that produce heat and electricity by means of an anode, cathode, and ionic conductive electrolyte material using an electrochemical process using chemical energetic gaseous fuel and oxidant gas (Figure 1.1).

In fuel cells, the fuel and oxidizer are located in different regions, unlike conventional production systems. Electricity is generated by the fuel supplied by the anode and the oxidant provided by the cathode. They react in an electrolyte/electrode unit (fuel cell). Generally, as those entering the cell, the reaction products leave the cell. Fuel cells can run for as long as they provide the necessary fuel and oxidant flow. In practice, fuel cells take various names according to working temperature, electrolyte type, and fuel type.

If classification is made according to working temperature, can be classified as Low temperature (25 °C to 100 °C) fuel cell (LT-FC), medium temperature (100°C to 500°C) fuel cell (IT-FC), high temperature (500°C - 1000°C) fuel cell (HT-FC) and very high temperature (1000°C and above) fuel cell (VHT-FC). However, the most common classification is made according to the electrolyte type.

Fuel cells have various names depending on the structure of the electrolyte. These; alkaline fuel cell (AFC), Proton exchange membrane fuel cell (PEMFC), Phosphoric

acid fuel cell (PAFC), Molten carbonate fuel cell (MCFC), Direct methanol fuel cell (DMFC) and solid oxide fuel cell (SOFC).

1.3. Development of Fuel Cells and Today

The first fuel cell studies were carried out in 1838 by Sir William Grove on the H_2-O_2 cell [1]. Realizing that constant current and power were produced as a result of the reverse reaction of the electrolysis of water during his work, Grove thus coincidentally realized a great invention. The first "Fuel Cell" term was used in 1889 by Charles Langer and Ludwig Mond [1.3] (Figure 1.2).

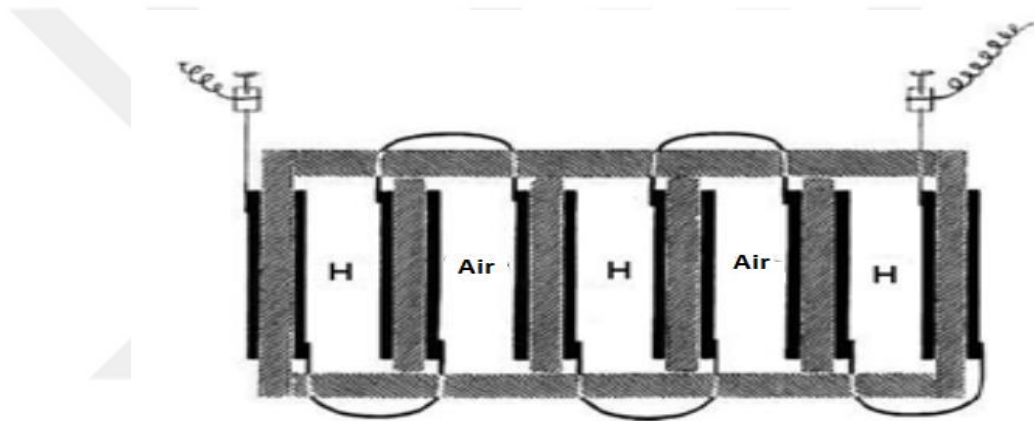


Figure 1.2. Mond and Langer's fuel cell

In 1893, Friedrich Wilhelm Ostwald investigated the role and effect of every element in the fuel cell on operation [2]. In 1896, William W. Jacques laid the foundations for molten electrolyte fuel cells. The coal is intended to produce electricity directly from the electrochemical energy. In 1937, Emil Baur succeeded in achieving the success of the solid oxide electrolyte fuel cell project initiated by famous scientist Nernst in 1900 [3].

Perhaps the most important work that enabled the fuel cell to arrive today is the work done by Thomas Bacon on alkaline fuel cells in 1959 [2,3]. The British engineer has developed a stationary fuel cell of 5 kW. Understanding the significance of this work, Pratt & Whitney has licensed this project to NASA programs. In the 1960s, Bacon's patents were used in the space research program of the United States to provide electricity and drinking water. As there was plenty of hydrogen and oxygen in the spacecraft's tanks, there was no question of finding fuel [1, 3].

The first field of application of fuel cells is space studies. In the United States, NASA's work has been used as interconnected 3 units with H₂-O₂ fuel cells in spacecraft of Apollo, Gemini, and Space Shuttle [1, 3].

A total of 93 fuel cell units were used in each unit. The total generated power is 1.4 kW and the voltage is 27-31 Volts. The weight of the cells is 111 kg [1, 3]. During the flight 1995, 450 kg of water and 325 kW of energy were produced. On the Gemini ship, a PEM type fuel cell was used (Figure 1.3). There are 32 cells in each unit and 1 kW of power is provided. On these three ships, 2 units were made to meet the needs, while the 3rd unit was prepared for urgent and special tasks.



Figure 1.3. Proton exchange membrane (PEM) fuel used in Gemini spacecraft

Today, space shuttle electricity is produced with 12 kW fuel cells. American UTC Fuel Cell Company meets NASA needs. UTC Power was the first company to produce stationary fuel cell systems for hospitals, universities and large businesses. Today, the 200 kW Pure Cell 200 systems are sold by this company [4].

UTC Power is the only company that supplies NASA with fuel cells for use in space vehicles (Apollo and space shuttle programs) and is also developing fuel cells that can be used in cars and buses. UTC Power has introduced the first automotive fuel cell with proton exchange membranes that can work even under freezing conditions [4].

Solid Oxide Fuel Cell (SOFC) powered by BMW hydrogen/gasoline fuel, which is developed for small and large scale energy production, has been produced as a

prototype vehicle and Research and development studies are ongoing [5,6]. A 100 kW capacity unit is used by Siemens Westinghouse for a long time. The efficiency achieved in these systems is 46% [7]. Today he is working on new types of fuel cells. Examples include; Ceramic electrolyte fuel cells with proton conductivity, and fuel cells used as fuel for the Zinc / Air mixture. In fuel cell technology, the fuel cell is resistant to the power density, gas impurities, and the electrode material is modified to prolong and optimize its life. Generating up to 250 kW of electricity from a single module; reducing the amount of precious metals used as catalysts, thereby increasing the yield and reducing the cost.

Development of designs that increase the performance, robustness, life, and cost of the system development of hydrogen storage systems; work continues on the development of conversion systems that will allow the use of fuels other than hydrogen.

Silent fuel cells are an alternative that can be used to provide heating and electricity needs in homes or apartments. The fuel cells that can be used in this type produce electricity from propane and natural gas, and the generated heat is recovered and used in heating systems. 3-5 kW fuel cells are suitable for domestic consumption. The US government is applying a tax reduction of \$ 1000 / kW for residential buildings for hydrogen fuel cell applications [7]. Stationary Power Generation System/High Power Generation System Applications there are hundreds of fuel cell stations in the world that are installed as fixed power sources. These energy generators; were extensively used in hospitals, in hotels, offices, schools, power stations, airports, electricity and heating systems. Companies using these systems are seeing reductions in energy expenditures of between 20% and 40%. The efficiency in Proton Exchange Membrane Fuel Cell (PEMFC) plants is around 55%. If the production of carbon dioxide and water vapor is assessed in the production of additional electricity, the energy efficiency increases to 80%. Fuel cell power generation systems take up little space. With a power plant in the minibus size, 20 kW of power can be generated [5, 7]. Examples of important applications of these plants are the 2MW of California's ONSI Company, UTC Fuel Cell of 200 kW in Alaska, and the 100 kW of Westinghouse-Canada in the Netherlands [6, 7].

Electric vehicles are at the forefront of new, clean alternative applications in the 2000s. Hybrid electric vehicles (petrol-fuel cell, motor fuel cell vehicles) are applied in the form. In these applications, fuel-cell electric vehicles are leading with many advantages and fuel cell electric vehicle application using hydrogen in future automotive technology will cover a great deal of space. Fuel cells have features that can serve as fuel for buses, trucks, cars and all kinds of vehicles. Fuel cell vehicles are cleaner and energy efficient than gasoline and motor-driven vehicles. Nowadays, considering the effects of vehicle emissions on environmental pollution, fuel cell vehicles are an environmentally friendly and profitable choice. Electric vehicles have higher efficiency than internal combustion engines. Depending on the energy content of the fuel used, the power generation in fuel cell vehicles is between 40-70%. The use of fuel cells without moving parts also reduces the noise pollution of the vehicle at a noticeable level. Another advantage is that, when hydrogen is used as fuel, only water is generated as emissions in vehicles.

While the use of pure hydrogen gas in vehicles is targeted, this preference should be investigated in short and medium term. Work on the storage of hydrogen gas continues at full speed and hydrogen storage requires high pressure, light cylinders, cryogenic liquid systems and solid metal hydride storage. Compressed hydrogen is not the best system and does not meet the volume and weight criteria required for light vehicles. With today's increasing interest in nanotechnology, carbon nanotubes targeted for use in hydrogen storage are promising for the future.

CHAPTER 2

GENERAL INFORMATION AND PREVIOUS STUDIES

2.1. Fuel cell Structure, Advantages of the fuel cell and Working Principle

A typical fuel cell consists of two electrodes, simply called anodes and cathodes; and electrolyte compressed between electrodes. These two ends have channels to distribute oxygen and hydrogen in the electrode layer. The fuel to be used is fed to the anode of the cell. Oxygen (or air) is given to the fuel cell catheter. Processing of a catalyst fuel, proton and electron are decomposed. These two pieces of fuel goes right through the separate routes. Proton passes through the electrolyte. Fuel cell a general scheme is given in Figure (2.1) [8].

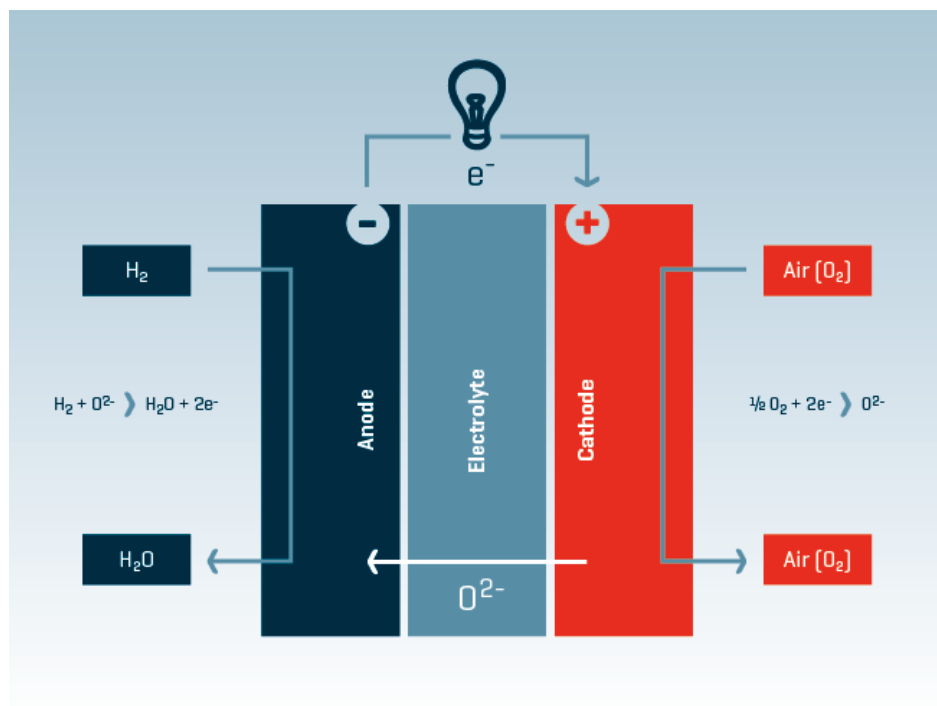


Figure 2.1. Fuel cell principles

The electrons must go through a different path in the outer circuit; they produce an electric energy that can be used before it is converted into a molecule. Completely As a result of this chemical process, the fuel pellet makes virtually no pollutants. For this reason, fuel cells are also referred to as zero emission engines [9].

The fuel-cell system generates much more electricity because it does not give a combustion reaction. The greatest feature that distinguishes this system from the platinum is that it does not require chargers for power generation and power generation will continue as fuel is supplied. In all fuel packs, water is released as a liquid or vapor product, depending on the battery operating temperature. If oxygen is used as the oxidizer, water, nitrogen, and water are used if air is used, and carbon dioxide is used when fuel is used in the composition. The water leaves the battery and thus the battery cools itself. However, at very high temperatures, the cooling equipment must be used in the cell [10].

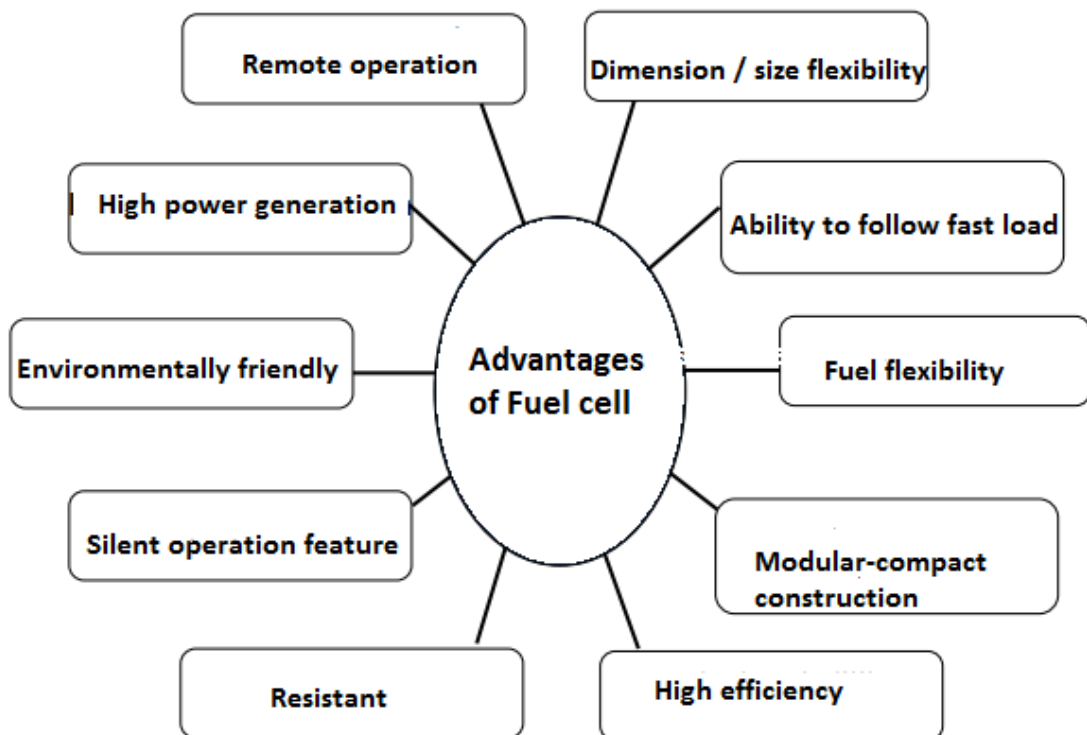


Figure 2.2. Advantages of fuel cell

2.1.1. Application Areas of Fuel cells

The Fuel cells, today, is being used for military purpose, portable vehicles, housing, space vehicles, fixed power, and transportation vehicles. They will also be power providers for fixed applications such as fuel cells, mobile applications such as portable computers and mobile phones, and power plants. Due to their high efficiency and low emissions, they will find a wide range of uses in transportation, from bicycle to public transport, from ships to airplanes [11].

Fuel cells have made significant strides in commercialization and have been commercially used in laptop computers, mobile phones and handheld cameras in the first place. Thanks to the use of fuel cells, the battery life of computers and mobile phones has reached a time of up to 30 hours, which is a short duration of two or three hours. Laptop computers, mobile phones and handheld cameras powered by fuel pillars are expected to become more widespread over the next few years. Systems such as boilers, air conditioners, and home-based electricity generation systems to be used in homes and offices are expected to be used in the near future [12].

2.1.2. Fuel Types

Fuel cell are classified by the application in working temperature, electrolyte type, and fuel type. If the operating temperature of the fuel cell is lower than 150 °C, it is called "low-temperature fuel cell" and if it is between 500 °C and 1000 °C it is called "high-temperature fuel cell". Low-temperature fuel cartridges have the potential to use hydrocarbon fuel and cheaper catalysts as opposed to good and expensive catalyst requirements such as simple fuel and platinum, such as hydrogen. The electrolyte used may be in the form of an alkaline in acidic or liquid, solid or liquid-solid mixture. The fuels used are typically hydrogen, natural gas (methane), methanol and propylene [13].

Although the operating principles of fuel cells are similar, the operating conditions and application areas differ. Fuel batteries are classified according to their electrolytes used in their bodies as follows:

- Proton Exchange Membrane Fuel Cells (PEMFC)
- Alkaline Fuel Batteries (AFB)

- Phosphoric Acid Fuel Cells (FAFC)
- Molten Carbonate Fuel Batteries (MCFB)
- Metal Hydride Fuel Pipe (MHFP)
- Electro-Galvanic Fuel Pipe (EGFP)
- Microbial Fuel Pilot (MFP)
- Direct Boriding Fuel Pump (DBFP)
- Direct Methanol Fuel Oil (DMFO)
- Direct Ethanol Fuel Chiller (DEFC)
- Direct Formic Acid Fuel Oil (DFAFO)
- Solid Oxide Fuel Pump (SOFP)

Table 2.1. Differences between fuel cells [14]

	PEMFC	AFB	FAFC	MCFB	SOFP
Electrolyte	Solid Polymer membrane	KOHLER	Liquid Phosphoric Acid	Liquid Melt carbonates	Containing Y_2O_3 zirconium
Work temperature	80°C	65°C-220°C	150°C- 220°C	650°C	600°C – 1000°C
Catalyze	Platinum	Platinum	Platinum	Nickel	Perovskite
Transferred Ion	H^+	OH^-	H^+	CO_3^{2-}	O^{2-}
Fuel Treatment	Battery Out	Battery Out	Battery Out	Inside the battery	Inside the battery
Anode Gas	Hydrogen	Hydrogen	Hydrogen	Hydrogen, Methane	Hydrogen, Methane
Cathode Gas	Pure oxygen or air	Pure Oxygen	Oxygen from air	Oxygen from air	Oxygen from air
Heat Management	Cooler	Cooler-Cogeneration	Cogeneration	Cogeneration	Cogeneration
Yields	%35-60	%50-70	%35-50	%40-55	%45-60
Other Features	Electrolyte solids being brought advantages It has. Low the temperature Other work Is an advantage.	Hydrogen and Good with oxygen performance Shows. Space Like research closed For applications Suitable.	Performance AFC Den is low.	Electrolyte corrosive And movement We could. Battery For structural stainless steel must. Expensive No metals needed.	Materials heat between expansion disproportion it may occur.

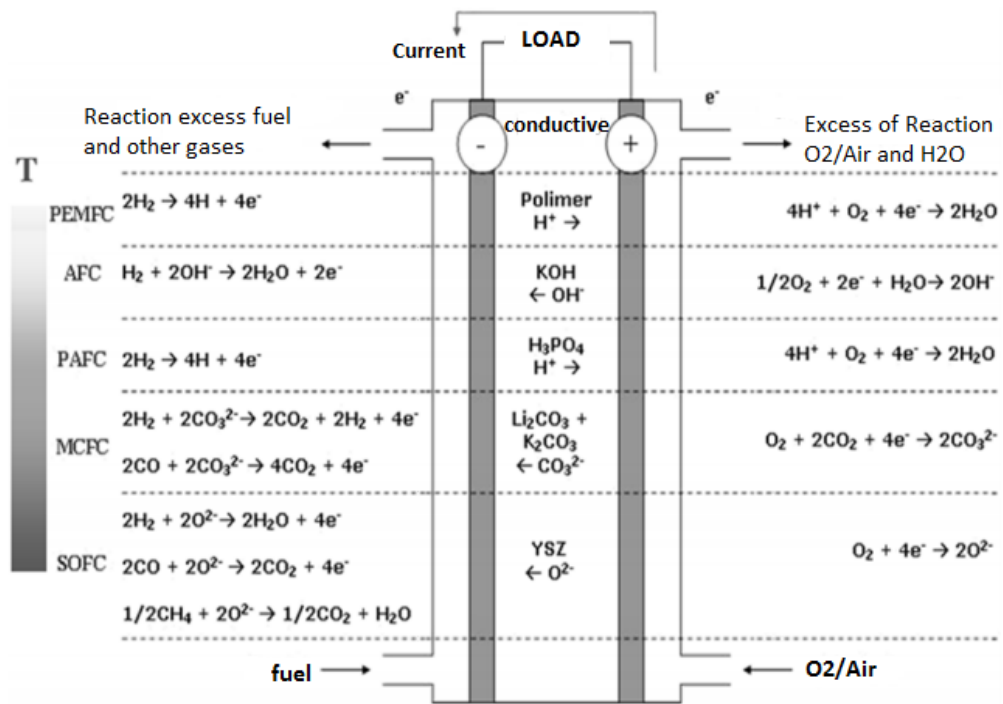


Figure 2.3. Types of fuel pellets

The operating temperatures and operating lifetimes of fuel pellets depend on the physicochemical and thermo mechanical properties of the materials used in the pile construction. The working temperature also plays an important role in the fuel cell. Also according to the fuel used, the catalyst is selected to increase the reaction speed. The chemical reaction is very slow in low temperature running fuel cylinders.

Platinum, which is very expensive as a catalyst, is used to accelerate the reaction and increase battery efficiency. This increases the battery cost. This is not the case for fuel cells operating at high temperatures. The battery operating temperature is sufficient to accelerate the reaction. Cheaper materials can be used as catalysts in high temperature bulbs [15].

2.1.3. Electrolyte for Solid Oxide Fuel Cell

Solid oxide fuel cells (SOFCs) can give effective and clean vitality transformation in an assortment of utilizations running from little helper control units to vast scale control plants. The real favorable position of SOFCs over polymer electrolyte layer power devices (PEMFCs) is their better resistance than polluting influences in the fuel, which takes into account their operation utilizing lower quality, accordingly not so much

exorbitant but rather more generally accessible, fuel. The better fuel adaptability is expected principally than the higher working temperature, which builds response rates in the fuel, additionally, increments the rates of undesired responses and makes warm worries amid warm cycling.

Consequently, the advancement and creation of materials to meet these prerequisites is a noteworthy test for the usage of financially intellect SOFCs. The key necessity for the solid electrolyte is that it has great ionic conduction to limit cell impedance, additionally has almost no electronic conduction to limit spillage streams, so control of the focus and portability of ionic and electronic charge bearers is basic. The electrolyte material should likewise be artificially and mechanically (e.g. thermal extension) good with other power module segments.

This similarity reaches out to manufacture forms, since a few procedures may be performed with numerous parts exhibit, which constrains the scope of parameters (e.g. temperature or weight) to those satisfactory for all segments. A noteworthy catalyst for the improvement of new electrolyte materials is in lessening the working temperature to 500–800 °C for the middle of the road temperature strong oxide energy components (IT-SOFCs).

Such a middle of the road working temperature will unwind a portion of the prerequisites identified with high-temperatures operation while keeping up an adequately high temperature to hold great fuel adaptability [16].

2.1.4. Bi₂O₃ Based Electrolyte

Bi₂O₃-based solid electrolyte frameworks are great oxygen anion conductors, which have been broadly examined, also assessed by numerous researchers. On account of their generally high electrical conductivity at intermediate (500-700 °C), they are utilized as artistic electrolytes in the solid oxide fuel cells (SOFC) or hydrogen SOFC for creating electrochemical energy. In the expansion, they are moreover utilized for the canalization of some heterogeneous responses, the incomplete oxidation of the hydrocarbons and the detachment of oxygen in the reactant thick layer reactors.

The assembling of photovoltaic cells, superconductors, paint shades, oxygen sensors and oxygen pumps can be given cases for other modern application regions of Bi_2O_3 -based materials.

By a wide margin, the most broadly contemplated electrolyte materials are ZrO_2 -based sort frameworks, which require high operational temperatures (800–1000 °C) to get attractive control yield. On the other hand, Bi_2O_3 -based electrolytes have high ionic conductivity amid direct temperature run (600–800 °C) when contrasted with zirconium oxide sort solid electrolytes. In any case, they are less steady under diminishing conditions and have high reactivity with the other SOFC segments; furthermore, their conductivity relies on upon the kind of Bi_2O_3 polymorphs. Along these lines, it is at present under concentrated study to enhance their properties as an electrolyte for the fuel cells applications. The ionic conductivity of these frameworks can be upgraded by two ways, to be specific stage moves and expanding cluttering in the framework by doping of different cations. Both of their conductivity and stability can be enhanced fundamentally by doping of Bi_2O_3 with the lanthanide cations [17].

2.1.5. Solid State Reaction

Is the most widely used strategy to plan polycrystalline solids from a combination of solids. Solids don't respond together at room temperature over typical time scales and it is important to warmth them to considerably higher temperatures, regularly to 1000 to 1500 °C all together for the response to happen at an apparent rate.

The components on which the attainability and rate of a strong state response depend incorporate, response conditions, basic properties of the reactants, the surface zone of the solids, their reactivity and the thermodynamic free vitality change related with the response [18].

A solid state reaction, additionally called a dry media response or a solvent less response, is a substance response in which solvents are not utilized. In an ordinary response, the responding specialists, likewise called the reactants, are put in a dissolvable before the response can happen. These reactants respond to frame another substance. After the response is finished, researchers can expel the new item from the

dissolvable. A solid state reaction, in any case, permits the reactants to artificially respond without the nearness of a dissolvable. The benefits of solid state reaction swell all through numerous businesses. It is imperative to financial matters in light of the fact that the disposal of solvents implies that items will cost less. This, thus, will make those items less expensive to purchase. With typical responses, researchers need to expel the remaining dissolvable from the subsequent item after a response has wrapped up.

Delivering materials from a solid state reaction will imply that researchers can sidestep the filtration procedure. Wiping out the dissolvable from the response implies that a solid state reaction creates more item than an ordinary response can. It likewise is all the more earth agreeable. Since there is no dissolvable, there is no waste to wipe out toward the finish of the response [19, 20].

2.1.6. Bi₂O₃ Crystal Structure

The structure of α -Bi₂O₃ comprises of layers of oxygen particles, parallel to the y and z axes at x=0.25 and x=0.75. Between these are layers of bismuth molecules arranged at x=0.00 and x=0.50 (Fig.2.4a).

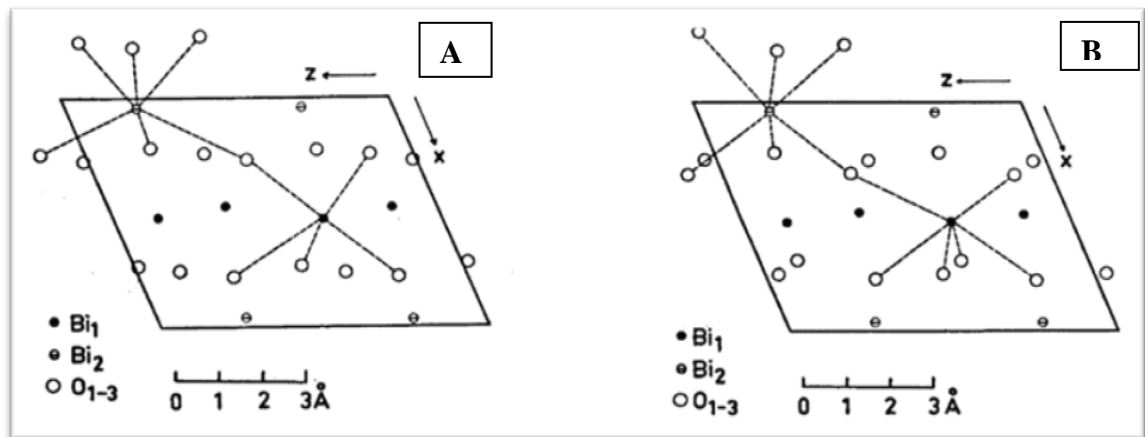


Figure 2.4. a) Projection of the structure on the xz-plane b) Projection of the structure, as given by Sillen, on the xz-plane [21].

The oxygen sheets, planar inside $\pm 0.13 \text{ \AA}$, are developed of pentagons and triangles, the sides of which are altogether associated with bismuth ions (Fig.2.4). The most limited, O-O separate in the structure is 2.78 \AA (Fig.2.4) There are two sorts of oxygen coordination around the bismuth atoms, one five-fold around Bi₁ and one six-fold

around Bi_2 (Fig. 2.4a). In the structure proposed by Sillén, both bismuth molecules were six-composed by oxygen atoms, at separations running from 2.39 to 2.55 Å [Table 2.2] in an unpredictable way (Fig. 2.4.b).

The Bi-O coordination separates in the structure exhibited in this paper might be arranged in 2 particular extents, considering an expected standard deviation in the Bi-O separations of 0.03Å [21].

I. Bi_1 - 2.08-2.29Å

II. Bi_2 -2.48-2.80Å (Table 2-2)

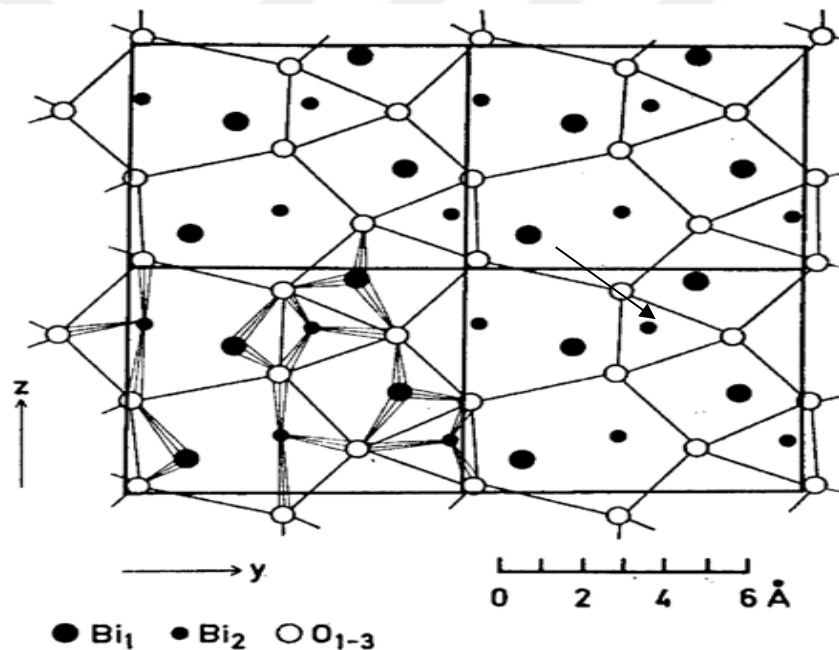


Figure 2.5. The oxygen layer at $x=0.25$ projected along x on the yz -plane of four unit cells. The bismuth atoms on each side of the layer are also plotted. The oxygen pattern is illustrated with single lines, while the Bi-O bonds have triple line design [21].

The oxygen polyhedron encompassing Bi_1 perhaps depicted as a misshaped octahedron with one of its corners evacuated. The apical Bi-O bond is surprisingly short, 2.08 Å. of the four outstanding bonds two falls in separation range I and two in range II (Table 2.2).

The coordination around Bi_2 has some likeness to that around Bi_1 . The apical corner is at a separation of 2.14 Å from the center bismuth atom, which is to some degree longer than the relating Bi_1 –O bond.

Table 2.2. Interatomic distances D_1 (Å) and their estimated standard deviations in the structure of α - Bi_2O_3 . The distances computed from the structure given by Sillén are listed under D_2 .

Bond	Distance D_1	Distance D_2
$\text{Bi}_1\text{-O}_3$	2.08(3)	2.54
- O_2	2.17(3)	2.52
- O_1	2.21(3)	2.39
- O_3	2.54(2)	2.54
- O_1	2.63(3)	2.39
- O_2	3.25(4)	2.51
$\text{Bi}_2\text{-O}_2$	2.14(3)	2.52
- O_1	2.22(3)	2.39
- O_3	2.29(2)	2.54
- O_2	2.48(3)	2.48
- O_1	2.54(3)	2.40
- O_3	2.80(2)	2.55

2.1.7. Bi_2O_3 Type Electrolytes and Their Properties

The primary research topic for improving the efficiency of electrochemical cells and improving working conditions is ionic conducting electrolytes. Bi_2O_3 based electrolytes have a very good electrical conductivity at intermediate temperature. Because of these properties, the industry is used in the production of some solid oxide electrolytes and membranes and in the production of electrochemical cells. Scientific research on the production, characterization, and applications of bismuth oxide (Bi_2O_3) phases has been ongoing for a long time. Scientific studies have concentrated on such issues as lower oxygen temperatures, higher oxygen ionic conductivity and the production and characterization of new electrolytes with higher yields, [22, 23]. Six crystal phases of pure Bi_2O_3 are available.

These are; monoclinic phase (α - Bi_2O_3), based in the Interior of the cubic (bcc) phase (γ - Bi_2O_3), surface-based cubic (fcc) phase (δ - Bi_2O_3), tetragonal (β - Bi_2O_3) phase, Orthorhombic phase (ε - Bi_2O_3) and triclinic phase (ω - Bi_2O_3). The δ -phase is known as the phase of pure α - Bi_2O_3 stable at high temperature and high conductivity phase [24].

If pure α - Bi_2O_3 , which has a melting temperature of 824 °C, is heated to about 729 °C, it becomes δ - Bi_2O_3 phase at high temperature and this phase is stable up to its melting point. The δ - Bi_2O_3 phase at 729°C is transformed to β -phase at about 650°C and to the γ - Bi_2O_3 phase at about 639°C. If the β and γ phases are cooled down to even lower temperatures, they are again transformed into α - Bi_2O_3 phase at about 500°C (Figure 2.6) [24, 25].

The three phases of the Bi_2O_3 compound; β , γ and δ -phases are unstable crystal phases that occur at high temperatures. At these three unstable phase charged O^{2-} ions are the charge carrier for the ionic conduction. These phases can be stabilized at room temperature by the incorporation of some oxide compounds into pure Bi_2O_3 by various reactions. Thus, if these phases are stabilized by doping at room temperature, a solid oxygen ion conductive electrolyte is produced which can be used at room temperature [26, 28].

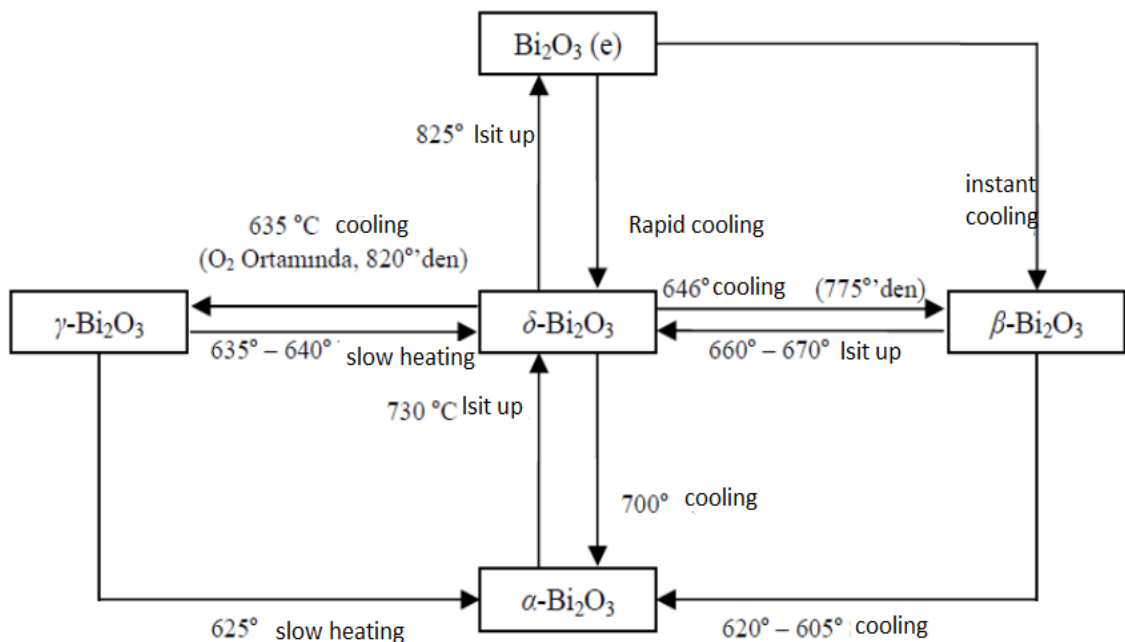


Figure 2.6. Phase transformation temperature diagram for Bi_2O_3 [25]

Studies have shown that the oxygen ionic conductivity of the α - Bi_2O_3 , β - Bi_2O_3 , and γ - Bi_2O_3 phases are lower than that of the δ - Bi_2O_3 structure [25, 28, 29]. δ - Bi_2O_3 has high oxygen ionic conductivity due to its defective fluoride (CaF_2) type crystal lattice and high oxygen ion vacancies.

The fluorite structure model is shown in Figure (2.7). The fluorite structure is in the corners and on the surfaces total 4 Ca atoms, and the sub-braid in the form of a quadrangular prism has 8 F atoms. In the case of defective fluorite structure; the sub-braid contains 6 atoms. Thus, in the unit cell of the Bi_2O_3 compound having defective fluoride structure, 4 Bi atoms, and 6 O atoms. There are 2 spaces in the underlay.

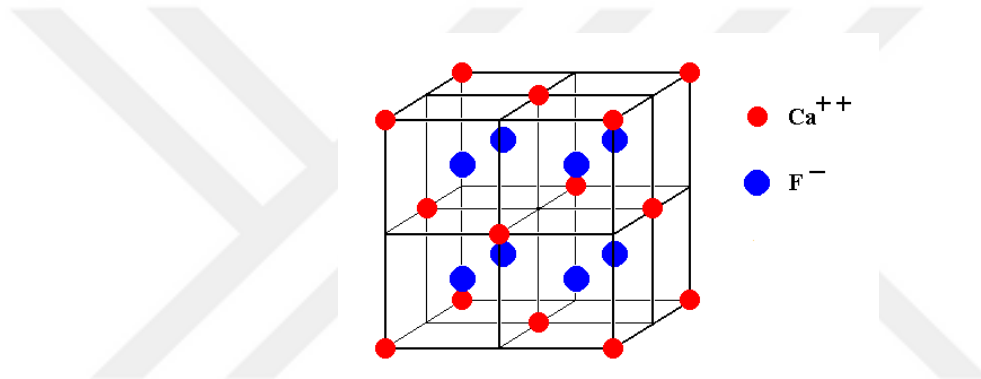


Figure 2.7. (a) Fluorite (CaF_2), crystal braids [11]

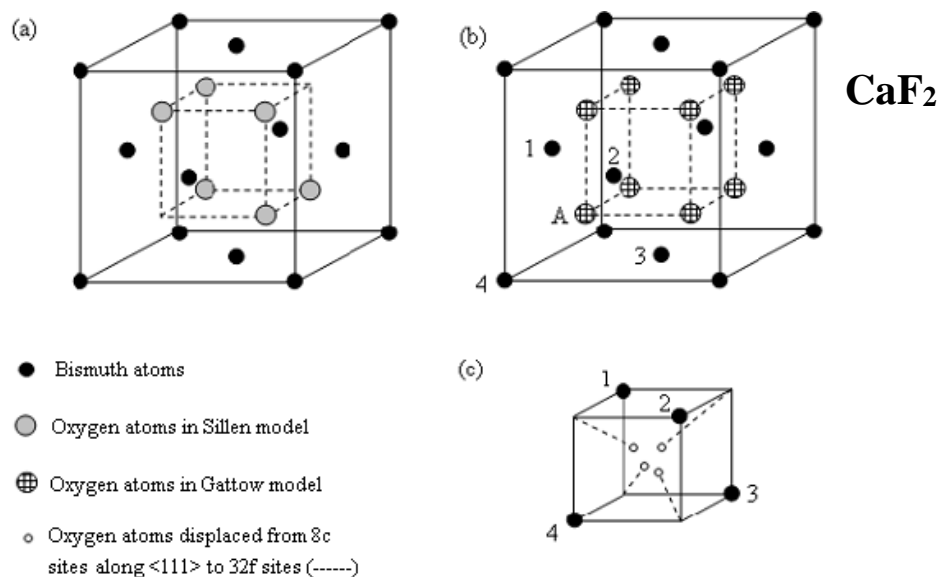


Figure 2.7. (B) Distribution of oxygen atoms and bismuth in a crystal lattice, based on the model of Sillen and Gattow

There are several models that describe the crystal lattice structure in terms of precisely the exact locations of the oxygen atoms in the sub-lattice. Some of them are important; Sillen, Gattow, and Willis are the models [30, 31].

The recent efforts to reduce costs and increase the efficiency of fuel tanks have gained momentum. One of the cost-reducing factors is reducing the working temperature of the fuel pillars. Electrolytes of the δ - Bi_2O_3 type are of great importance in fuel-cell operations. At lower temperatures, it has higher oxygen ionic conductivity than other solid electrolytes. It has the highest conductivity value around 500-800 °C compared to today's electrolytes. The pure bismuth oxide compound is stable between 725-825 °C and loses its stability when it is cooled to room temperature. Many researchers are studying how to stabilize the δ - Bi_2O_3 phase at low temperature [23, 32, 34].

It has been reported that some of the metal and alkaline earth metal oxides ($M = \text{Zr, Y, Mo, Co, W, Sr, Ca, La, Se, V, Eu, Gd, Sm, Sb, Ge, Si, Zn}$ and Pr). Stable phases are obtained at room temperature by doping into Bi_2O_3 (doping). The δ - Bi_2O_3 phase and the other phases, which are stable at high temperature with the help of additives, become stable at room temperature [29, 35].

The phases stabilized at room temperature include defects due to lack of oxygen ions in crystal structures. The conductivity value depends on a number of oxygen ions in the crystal structure and the temperature.

In this thesis, δ - Bi_2O_3 phase, which is stable at high temperature; Eu_2O_3 , Dy_2O_3 , and Tm_2O_3 have been tried to be stabilized as additives.

2.1.8. Synthesizing and stabilizing the phase of pure Bi_2O_3

In studies conducted on the pure Bi_2O_3 composition so far, it has become possible to stabilize unstable crystal modifications at room temperature and in pure state it was not possible to bring it. However, these phases can be stabilized at room temperature by adding some other oxide compounds into pure Bi_2O_3 by various reactions.

For example, if oxides such as MoO_3 , ZrO_2 , Y_2O_3 , CoO , WO_3 , SrO , CaO , La_2O_3 , SeO_2 , V_2O_5 , Eu_2O_3 , Gd_2O_3 , Sb_2O_3 , Dy_2O_3 , Sm_2O_3 , Ho_2O_3 are doped into pure Bi_2O_3 , the above-mentioned phases of Bi_2O_3 may become stable at room temperature.

The Ln_2O_3 oxide compounds of the Lanthanide group elements are the most studied additives in the stabilization of Bi_2O_3 phases at room temperature by MxO_y addition.

In the synthesis of the Bi_2O_3 phases, nature, additive ratio, heat treatment time, heat treatment temperature, cooling rate (self-cooling or rapid cooling), grinding time and density, particle sizes, etc. Parameters are effective. These variables influence structural features such as unit cell constants, stoichiometric composition, and surface properties [38, 41].

Stoichiometric compounds are generally stabilized and all cations and anion sites are filled for Bi_2O_3 stoichiometric phases [42]. The non-stoichiometric $\delta\text{-Bi}_2\text{O}_3$, $\gamma\text{-Bi}_2\text{O}_3$ and $\beta\text{-Bi}_2\text{O}_3$ phases are stabilized at room temperature by doping and crystal lattice defects are reported to be defects in the literature due to O^{2-} ion deficiency, which increases with increasing amounts of these defects.

On the other hand, as a number of additive increases, the lattice parameter of the unit cell also changes [40, 43]. The reason for this change in the lattice parameter is due to the difference in the effective ion radii between the substitution cations for the oxidation-reduction reactions in the additive cations occurring during displacement, the substitution of the Bi^+ cations for the My^+ cation and the Bi^{3+} cations of the MxO_y oxide compound (aliovalent contribution) [44, 47].

The difference in ionic radii also affects the electrical conductivity [48]. The rate of diffusion of the additive cations into the lattice is rather slow, and long heat treatment is required for the synthesis to take place [38, 44, 46, 47]. This is due to the fact that the inter-cation displacement is slow due to diffusion.

The kind of the contribution determines the phase of the synthesized phase. The ionic radii reported by Shannon and Prewitt (1969) and Jia (1991) for the cations in the adjunct compounds we use are shown in the following table (Table 2.3) [49, 50].

Table 2.3. Ionic radii of some ions [49]

Iyon	R (Å)
Bi ³⁺	1.02
O ²⁻	1.40
Dy ³⁺	0.91
Dy ²⁺	1.07
Eu ³⁺	0.95
Eu ²⁺	1.17

Bi₂O₃ also causes a color change in the oxide compound doping sample. Colors change regularly depending on the amount of additive. Pure Bi₂O₃ is light yellow color. Very small amounts of dopant are still a light yellow, depending on the color of the additive after homogenous mixing.

However, as the heat treatment is applied, a darkening of the colors from dark to reddish brown is observed. This color thickening increases as a number of additive increases. The resulting O²⁻ gaps contribute to color change. Color differences are created by electrons at the light points (color dots) through the mechanism of light absorption [44, 47, 51].

2.1.9. Used chemicals

2.1.9.1. Bismuth trioxide (Bi₂O₃)

Bismuth; Symbol Bi, atomic number 83, mass number 208.980 g/mol . the period is an element of group 5A. Electronic configuration; [Xe] 4f¹⁴5d¹⁰6s²6p³ shows this element that has metallic properties. The melting point of the element is 271.5°C and the boiling point is 1564°C. The density at room temperature is about 9.80 g/cm³.

Bismuth compounds are present in oxidation steps +3 and +5. It is the metal with the highest diamagnetic property among the other metals and the least thermal conductivity. The crystal structure is rhombohedral. Bismuth; It is a fragile metal with white, silver-pink shades of color.

Bismuth trioxide is the most important component of bismuth in terms of industry formed by the chemical composition of bismuth and oxygen.

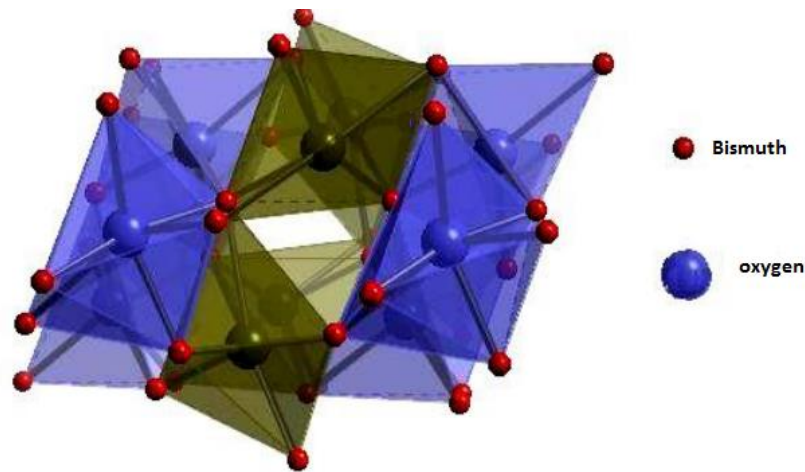


Figure 2.8. Crystal structure of pure Bi_2O_3

Bismuth trioxide with 99.9% purity was used as starting material in the study. Bismuth trioxide is a polymorph and is a yellowish powder. It dissolves in weak alkaline character and acid. The melting point of the compound is 825°C and the density is 8.9 g/ml. The compound is insoluble in water but soluble in acid. The pure Bi_2O_3 is a monoclinic phase that is stable at room temperature. This phase is expressed as $\alpha\text{-Bi}_2\text{O}_3$. The other phases of Bi_2O_3 are not stable at room temperature and are stable at high temperatures. These phases can be stabilized at room temperature by the addition of other oxides into the monoclinic $\alpha\text{-Bi}_2\text{O}_3$ by solid state reactions under certain conditions.

Crystal Properties

Formula: Bi_2O_3

Atomic Mass: 465,950 g/mol

Crystal Structure: Body Centric Cubic (bcc) at high temperature ($>730^\circ\text{C}$), (or δ -phase)

Magnetic susceptibility: $-83.0 \cdot 10^{-6} \text{ cm}^3/\text{mol}$

Physical characteristics

Color: Light yellow

Appearance: Solid crystalline

Melting Point: 817°C

Boiling point: 1.890°C

Density: 8.9 g/cm^3

2.1.9.2. Europium Trioxide (Eu₂O₃)

Europium Oxide is used as a phosphorus activator, called Europium. Color cathode-ray tubes and liquid crystal displays are known to be used in Europium oxides such as computer monitors and red phosphorus used in television production. Europium oxide is also applied to a special plastic laser material [52,53].

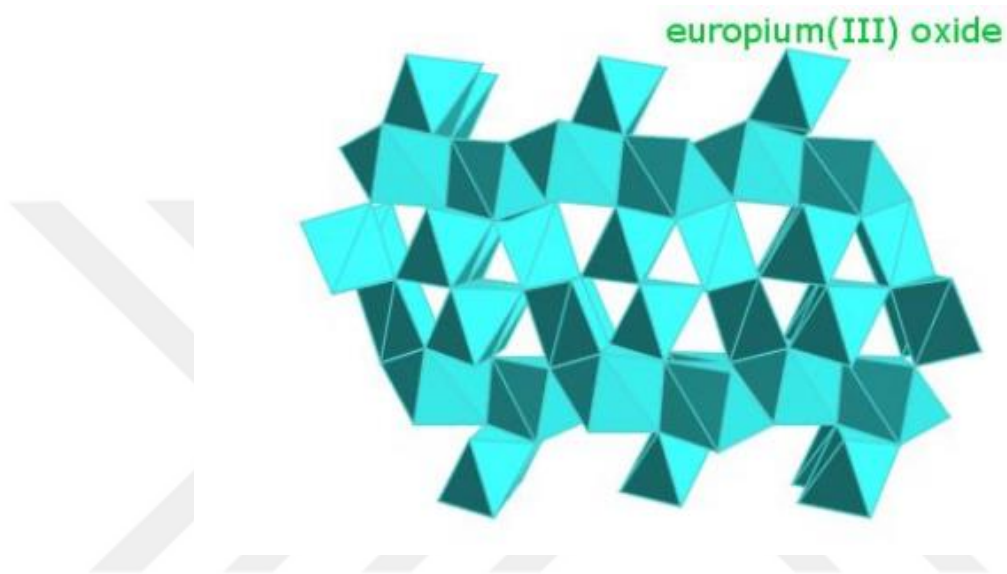


Figure 2.9. Crystal structure of pure Eu₂O₃ [54.55]

Crystal Properties

Formula: Eu₂O₃

Atomic Mass: 351.917 g/mol

Crystal Structure: Monoclinic, Cubic

Thermal conductivity 2.45 W/ (m K)

Physical characteristics

Color: White

Appearance: Solid crystalline

Melting Point: 2350°C

Boiling point: 3.790 °C

Density: 7.40 g/cm³

2.1.9.3. Thulium Trioxide (Tm₂O₃)

Thulium (III) oxide is a pale green solid compound, with the formula Tm₂O₃. It was first isolated in 1878 from an impure sample of Erbium by Per Teodor Cleve, who named it Thulia. It can be prepared in the laboratory by burning thulium metal in air, or by decomposition of their oxoacid salts, such as thulium nitrate [56].

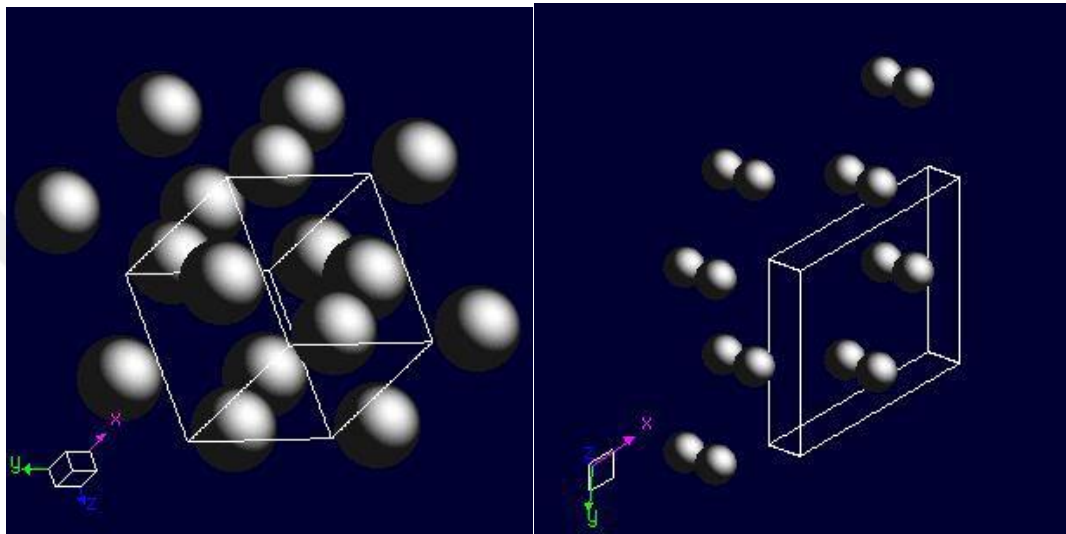


Figure 2.10. Crystal structure of pure Tm₂O₃

Crystal Properties

Formula: Tm₂O₃

Atom mass: 385.866 g/mol

Crystal structure: Cubic

Standard state: solid at 298 K

Physical characteristic

Color: silvery white

Classification: Metallic

Melting point: 2,341°C

Boiling point: 3,945°C

Density: 8.6 g/cm³

2.1.9.4. Dysprosium Trioxide (Dy₂O₃)

Dysprosium Oxide (Dy₂O₃) is a pastel yellowish-greenish, the slightly hygroscopic powder having specialized uses in ceramics, glass, phosphors, lasers and dysprosium metal halide lamps [57,58].

It can react with acids to produce the corresponding dysprosium (III) salts:

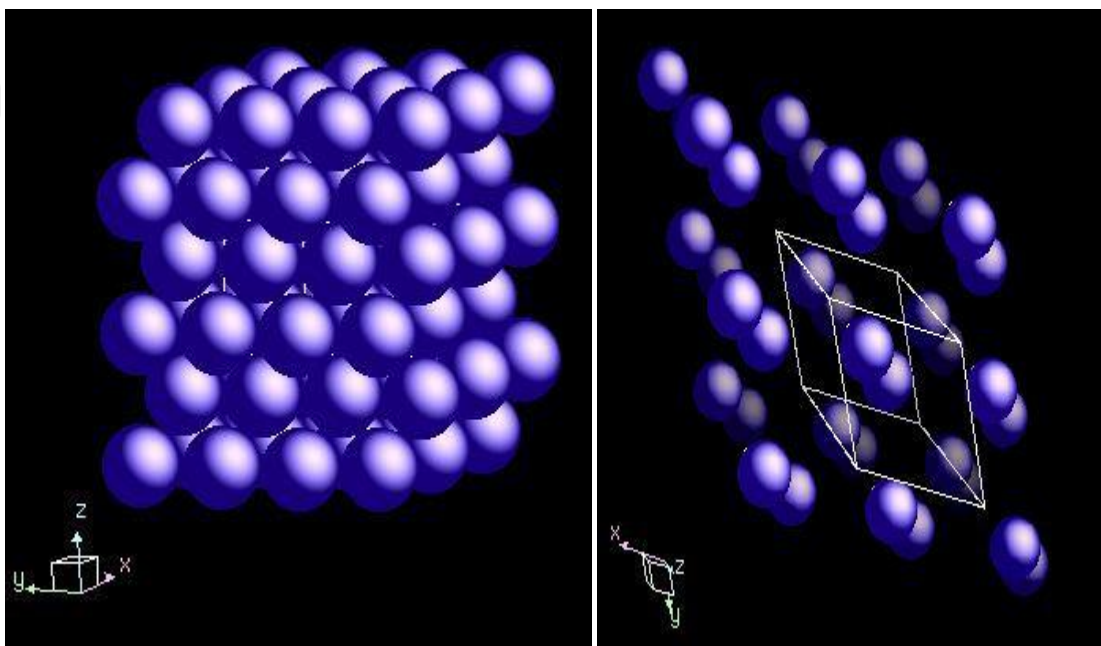
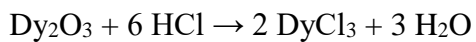


Figure 2.11. Crystal structure of pure Dy₂O₃

Crystal Properties

Formula: Dy₂O₃

Atom mass: 372.998 g/mol

Crystal structure: crystalline solid

Classification: Metallic

Physical characteristics

Color: white

Melting point: 2,408°C

Density: 7.80 g/cm³

Appearance: pastel yellowish-greenish powder.

2.2. Previous Studies

Bi_2O_3 exists in the monoclinic form at room temperature and is predominantly an electronic conductor. The high temperature ($>730^\circ\text{C}$) oxygen-ion conducting face centered cubic (fcc) phase (or δ -phase) can be stabilized with the addition of a number of other metal oxides such as Y_2O_3 , Dy_2O_3 , Er_2O_3 , Gd_2O_3 , Nb_2O_5 and Ta_2O_5 . For rare-earth doped materials, the minimum amount of the oxide phase required to stabilize the δ -phase at lower temperatures varies with the ionic radius of the stabilizing cations [59].

Takahashi et al. [60] have shown that the stabilized cubic phase had the highest ionic conductivity amongst all oxygen-ion conductors.

Amarilla et al. [61] synthesized series of Bi_2O_3 -based oxide $\text{Bi}_{2-x}\text{U}_x\text{La}_x\text{O}_{(3+3x/2)}$ by two different methods and observed, on the basis of X-ray data that crystallize with cubic or hexagonal symmetry depending on the composition and synthesis procedure. In particular, the stabilization of the fluorite-type structure as a single phase at room temperature has been achieved in the compositional range $0.154 \geq x \geq 0.091$. The annealing of materials at 600°C for 500h yields in all case a ‘tetragonal’ phase that is isolated as the only phase for $x = 0.222$, since the main objective in the development of new materials for these application is to obtain electrolytes with higher conductivities and lower activation energies at lower temperature.

In recent years much attention was focused on materials known as BIMEVOX (BI: bismuth, ME: dopant metal, V: vanadium, OX: oxygen) related to a family of materials based on a narrow composition in the $\text{Bi}_2\text{O}_3 - \text{V}_2\text{O}_5$ system ($\text{Bi}_4\text{V}_2\text{O}_{11}$) where V is partially substituted by other cations such as Cu, Ti, Zn, Co, Mo and Ni and the discovery of fast oxide ion conductivity in $\text{Bi}_4\text{V}_2\text{O}_{11}$ [62]. Ionic conductivity of $4 \times 10^{-4} \text{ Scm}^{-1}$ has been reported by Yan and Greenblatt [63] for $\text{Bi}_4\text{V}_{1.70}\text{Ti}_{0.30}\text{O}_{10.85}$ at 223°C . Despite the high conductivity, they are reduced easily in atmospheres containing low oxygen partial pressures, have an extremely narrow electrolyte domain and are useful for limited electrochemical applications in the low temperature range ($< 500^\circ\text{C}$). However, Chmielowiec et al. [64] presented a work concerns BIMEVOX based solid electrolyte doped with rare earth elements (lanthanum). According to them, addition of La_2O_3 increases the melting point and conductivity of $\text{Bi}_4\text{V}_2\text{O}_{11}$ by stabilization of high temperature good ionic conductive γ - $\text{Bi}_4\text{V}_2\text{O}_{11}$ phase up to 3% La content.

Kant et al. [65] have synthesized the Mn^{2+} -doped compounds $\text{Bi}_4\text{V}_{2-x}\text{Mn}_x\text{O}_{11-\delta}$ ($0 \leq x \leq 0.4$) by solid state reaction technique and investigated by X-ray diffraction and ionic conductivity measurement that high ionic conducting γ -phase is stabilized for $x \geq 0.2$.

Whereas the ability to introduce Ga into V-site of $\text{Bi}_4\text{V}_{2-x}\text{Me}_x\text{O}_{11-\delta}$ leads to the stabilization of β -phase in the composition range $0.2 \leq x \leq 0.4$. The highest ionic conductivity is observed in $\text{Bi}_4\text{V}_{1.8}\text{Ga}_{0.2}\text{O}_{11-\delta}$ with $\sigma = 3.40 \times 10^{-6} \text{ S/cm}$ [66].

Krok et al. [67] have investigated the conductivity behavior and cell parameter variation in the double substituted BIMEVOX system $\text{Bi}_2\text{V}_{0.9}\text{Co}_y\text{Cu}_{0.1-y}\text{O}_{5.35}$. According to them, the volume of unit cell varies due to the micro domains of Co and Cu rich region in this double substituted system. Also the low and high temperature conductivity increase with increase Co content, but overall conductivity appears to be lower due to the some type of defect trapping in the double substituted system.

Ekhelikar et al. [68] have synthesized solid solution of Y^{3+} and Gd^{3+} doped Bi_2O_3 and observed that solid solution containing 20-40 mol % of Y_2O_3 had fcc structure but Gd_2O_3 doped samples because of larger cationic radius of Gd^{3+} (0.94 Å) reveals that fcc phase is not stabilized and formed rhombohedral phase. So, FCC phase is stabilized by doping with oxides with relatively small cationic radius Y^{3+} (0.90 Å) than Bi^{3+} (1.03 Å).

Since pure or doped δ - Bi_2O_3 is the best high-temperature ionic conductor known. At the same time, when doped with stable and well known high conductivity of Zirconia several papers have been published regarding the Bi_2O_3 - ZrO_2 system. Abrahams et al. [69] concluded in the Bi_2O_3 - ZrO_2 system, the formation of $\text{Bi}_{2-x}\text{Zr}_x\text{O}_{3+x/2}$ ($0.05 < x < 0.17$) occurs when the corresponding oxide mixture are quenched after heating at 850°C for 12 h. Substitution of Zr^{4+} for Bi^{3+} in the lattice results in the introduction of interstitial oxide ions. These oxide ions will contribute to total ionic conductivity. These β_{III} -phase which has a defect fluorite structure with ordered vacancies transform to show δ - Bi_2O_3 which has a fluorite structure with disordered vacancies on the oxygen sub-lattice [70].

The composition $\text{Bi}_{1.85}\text{Zr}_{0.15}\text{O}_{3.075}$ prepared by Abrahams et al. was further structurally characterized and refined in the tetragonal system. Since the structure of $\text{Bi}_{1.85}\text{Zr}_{0.15}\text{O}_{3.075}$ is similar to that of β - Bi_2O_3 , the new phase was termed as β_{III} -phase.

Very recently, an increase of the Zr content up to $x = 0.67$ in the quenched $\text{Bi}_{2-x}\text{Zr}_x\text{O}_{3+\delta}$ with the $\beta_{\text{III}}\text{-Bi}_2\text{O}_3$ around $730\text{ }^\circ\text{C}$ and shows a segregation of a mixture of predominantly $\gamma\text{-Bi}_2\text{O}_3$ structure was reported again [71].

From the foregoing, it appears that there are considerable discrepancies regarding the compounds or solid solutions and their stability, particularly in the region with higher ZrO_2 contents.

Recently, the mechanochemical treatment of $2\text{Bi}_2\text{O}_3\text{-}3\text{ZrO}_2$ led to the gradual formation of very fine Nano crystalline phase, which resembled the high-temperature $\delta\text{-Bi}_2\text{O}_3$. When mechanochemical treated samples were heated at $820\text{ }^\circ\text{C}$.

Now, slowly cooled, yield initial $\alpha\text{-Bi}_2\text{O}_3$ and $m\text{-ZrO}_2$ phase rather than $\delta\text{-Bi}_2\text{O}_3$ at room temperature as well as quenched sintered samples contained a mixture of $\beta\text{-Bi}_2\text{O}_3$ and $m\text{-ZrO}_2$ phase confirming that ZrO_2 stabilized $\beta\text{-Bi}_2\text{O}_3$ [72].

Sood et al. [73] synthesized a system $(100-x)\text{ZrO}_2(x)\text{Bi}_2\text{O}_3$ ($x=5, 10, 15$) in which a tetragonal $\text{Bi}_{7.38}\text{Zr}_{0.62}\text{O}_{12.31}$ phase has formed in all the samples after sintering at $850\text{ }^\circ\text{C}$ for 24 h. Apart from this, ZrO_2 and Bi_2O_3 are also identified as minority phases. The volume fraction of $\text{Bi}_{7.38}\text{Zr}_{0.62}\text{O}_{12.31}$ phase increases with increasing concentration of Bi_2O_3 .

Park et al. [74] designed bilayer SDC (Samaria-doped ceria) / ESB (Erbia-stabilized bismuth oxide) electrolyte. In this bilayer electrolyte SDC layer prevents the ESB layer from decomposing at very low PO_2 and have a higher t_i transference number than single electrolyte layer. Also, the conductivity of this bilayer ESB/SDC is higher because of the formation of higher conductivity ESB phase in the SDC grain boundaries.

Zdujić et al. [75] synthesized non crystalline $\text{Bi}_{0.78}\text{Hf}_{0.59}\text{Zr}_{0.63}\text{O}_{3.61}$ solid solution with a fluorite-type $\delta\text{-Bi}_2\text{O}_3$ structure by prolonged mechanochemical treatment of a powder mixture in a zirconia medium. The high value of electrical conductivity is, close to 0.1 Scm^{-1} make the mechanochemical synthesized solid solution a promising high oxide ion conductivity material.

Similarly S.N.et al. [76] synthesized materials $\text{Bi}_2\text{O}_3\text{-Nb}_2\text{O}_5$ binary systems successfully via a mechanochemical method at lower temperature than the solid state. Electrical

measurements indicated that there was no significant difference in the conductivities synthesized by the two different methods.

As we know, the unit cell of the fluorite-type oxide consists of the so called M_4O_8 structure. The metal ion is surrounded by eight O-ions and O-ion is surrounded by four metal ions to form a tetragonal arrangement. The ratio of metal ionic radius to oxygen ionic radius should be greater than 0.732 in order to form a stable fluorite structure. Although the ratio of Bi ionic radius (1.17 Å) to oxygen ionic radius (1.38 Å) is 0.848, the high oxygen vacancy concentration still destabilizes the fluorite structure. In order to stabilize the fluorite structure, it is needed to reduce average cationic radius. The sintered $(YO_{1.5})_{0.1}(WO_3)_{0.15}(BiO_{1.5})_{0.75}$ consists of a cubic fluorite structure and a very small amount of rhombohedral Y_6WO_{12} . The addition of Y_2O_3 reduces the mismatch in cation size and gives the average cationic radius of the matrix 1.06 Å [77].

Since, the ionic conductivity in Bi_2O_3 based materials depend on the mobility of anion in the fluorite structure as mentioned above. The high mobility is due to high polarizability of Bi_3^+ . So, the polarizability of the cations plays an important role in ionic conductivity. Also, all of the dopants typically used to stabilize the cubic structure of Bi_2O_3 are less polar than Bi_3^+ .

Polarizability is proportional to the cube of ionic radius [78]. The lanthanide dopants ($Ln = Yb, Er, Ho, Dy$) have both smaller ionic radii and lower polarizabilities than the host Bi ions. So, the conductivity in cubic bismuth oxide is reduced due to substitution of highly polarizable bismuth ions with less polarizable lanthanide ions in the cation sub lattice. Dysprosium, which has the highest radius and highest polarizability among all dopants, exhibited the least decay in conductivity.

With the excellence in oxide ion conductivity of Bi_2O_3 based materials have turned out to be best for many application like separation of oxygen from air, SOFC, chemical sensor etc. A considerable number of studies have been done on the crystal structure, ionic conductivity of bismuth oxide based materials.

However, the mechanical properties of the materials have been investigated in the application of devices by Paydar et al. [79] According to them the addition of 3Y-TZP particles in BICUVOX enhance the mechanical properties by distributing the particles

along grain boundaries of BICUVOX. These distributions reduce the grain size without degrading the ionic conductivity.

Singhal and Kendall [80] note that stabilized zirconia and ceria possessing the fluorite structure has been the most favored SOFC electrolytes with perovskites, brownmillerites and hexagonal structured oxides as more recent alternatives. Among the candidate materials, zirconia is a relatively cheap base material and is by far the most popular electrolyte material for SOFC. Among the available electrolyte materials, operating temperature is very important to electrolyte performance.



CHAPTER 3

MATERIALS AND METHODS

3.1. Preparation of Samples

In order to synthesize the $(\text{Bi}_2\text{O}_3)_{1-x-y-z} (\text{Dy}_2\text{O}_3)_x (\text{Eu}_2\text{O}_3)_y (\text{Tm}_2\text{O}_3)_z$ phases, which is called the quaternary system, at different molar ratios in percentages, $5 \leq x, y, z \leq 20$, in the stoichiometric range has been used. In this study, ten samples coded M (M1-M10) were prepared by using standard solid state reaction technique. Sample label and their composition are given in Table 3.1. The chemical formula of the compound formed here is; $\text{Bi}_{1-x-y-z}\text{Dy}_x\text{Eu}_y\text{Tm}_z\text{O}_3$.

Table 3.1. Mole percentages and quantities of materials used in mixtures

Sample label	Bi_2O_3 mol (%)	Bi_2O_3 (g)	Tm_2O_3 mol (%)	Tm_2O_3 (g)	Eu_2O_3 mol (%)	Dy_2O_3 (g)	Total Mass (g)
M1	85	3.960635	5	0.192933	5	0.186499	4.516025
M2	80	3.727656	10	0.385866	5	0.186499	4.475979
M3	75	3.494678	15	0.578799	5	0.186499	4.435934
M4	70	3.261699	20	0.771732	5	0.186499	4.395888
M5	80	3.727656	5	0.192933	10	0.186499	4.459005
M6	75	3.494678	5	0.192933	15	0.186499	4.401985
M7	70	3.261699	5	0.192933	20	0.186499	4.344965
M8	80	3.727656	5	0.192933	5	0.372997	4.469545
M9	75	3.494678	5	0.192933	5	0.559496	4.423065
M10	70	3.261699	5	0.192933	5	0.745994	4.376585

Appropriate quantities of the required constituent oxides of high purity fine powders were thoroughly mixed. The mixtures were milled for a 30 min in agate mortar to obtain a homogeneous mixture and grain shrinkage (Figure 3.1).

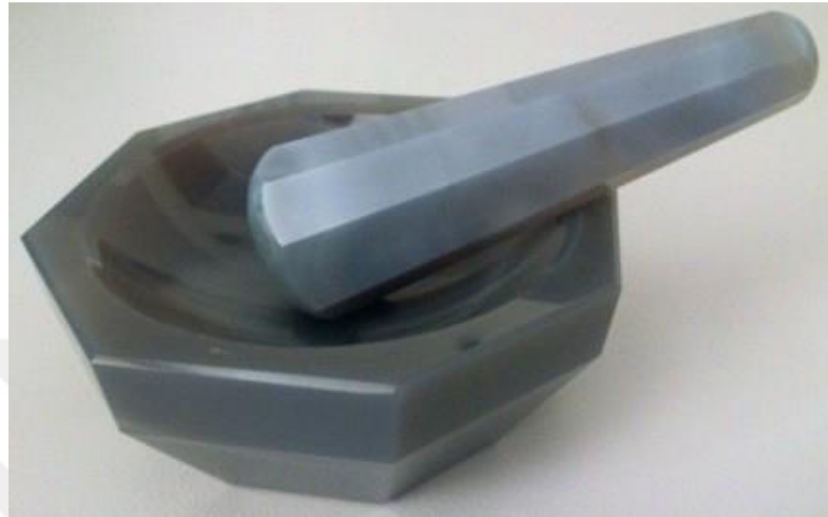


Figure 3.1. Agate mortar

Solid state reactions were carried out in a furnaces and alumina crucibles operating in an open atmosphere (Figure 3.2). Alumina crucibles were heat treated for 100 hours and at 750 °C before starting the reaction process. The empty masses of crucibles were measured before and after this heat treatment (Figure 3.3). This process was repeated until the masses of the crucibles had the same values before and after the heat treatment. The purpose here is to bring the crucible to a fixed scale. With this method, the weighting to be made during the heat treatment applied to the specimens and the expected sample mass changes will only belong to the specimens.

This mixture was annealed at 750 °C for 100 h in alumina crucible which has been prepared as mentioned above, and slowly cooled until room temperature was reached. Figure 3.4 shows images of the produced samples before and after annealing.

In order to perform X-ray diffraction (XRD) measurements after the heat treatment step, a certain amount of powder was sampled to determine whether any phase was formed and to measure the electrical conductivities of the phases formed. Afterwards, powder samples were cold pressed into pallets and electrical conductivities were measured from pallets. Pressing was carried out with Specac brand press machine (Figure 3.5).



Figure 3.2. Furnaces used for solid state reactions



Figure 3.3 Alumina crucible



Figure 3.4. Images of the produced samples before and after heating



Figure 3.5. Manual hydraulic presses and some solid electrolyte materials sintered after packaging

The samples placed in a mold having a diameter of 13 mm (Figure 3.5), were pressed at a pressure of 7 tons/cm^2 . Again, all the tablets formed as shown in (Figure 3.6) were prepared to be at least 1 mm thick. After this step, conductivity measurements can be started.

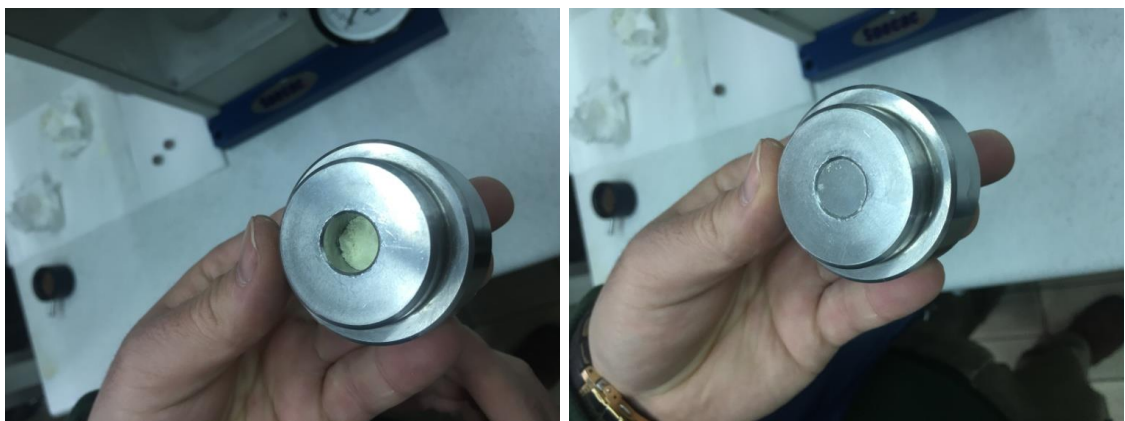


Figure 3.6. Pressing of the sample

3.2. Differential Thermal and Thermogravimetric Analysis (DTA/TG)

DTA (Differential thermal analysis) is a technique for recording the difference in temperature between a substance and a reference material as a function of time or temperature as the two specimens are subjected to identical temperature regimes in an environment heated or cooled at a controlled rate.

TGA (Thermogravimetric Analysis) sometimes performed simultaneously with DTA measures the weight loss or gain as a function of temperature with high accuracy. The TGA trace appear as steps, one can deal with the derivative of TGA (DTG) with respect to time or temperature and this trace consist from peaks.

In particular, the phase transformation temperatures, thermal stability and other related thermal properties of the materials synthesized have been investigated by measuring simultaneously with the DTA/TG system. In these measurements, a Perkin Elmer DTA/TG system (Figure 3.7) was used. Measurements were carried out from room temperature to temperatures of 800 °C-900 °C with a ramping rate of 10 °C/min, in dynamic inert gas atmospheres, in platinum sample containers, with an α -Al₂O₃ inert reference. Amount of sample used for measurement was about 5-20 mg.



Figure 3.7. Image of the Perkin Elmer DTA/TG measurement system

3.3. X-Ray Powder Diffraction

In a powder diffractometer, an X-Ray beam strikes a flat surface of a powder at an angle θ , and simultaneously the intensity of the diffracted X-Ray beam at an angle 2θ is detected. With this so called θ - 2θ scan, the positions of diffraction peak are resolved, and from the position and the intensity of these peaks the structure of major phases and the presence of unknown phases can be revealed.

X-ray powder diffraction (XRD) technique has been used extensively to characterize the phases present. For this purpose, a Bruker AXS Brand D8 Advanced powder diffractometer (Figure 3.8) which can scan diffraction pattern in a computer-controlled process has been employed. Ni-filtered Cu- K_{α} ($\lambda=1.5418\text{\AA}$) radiation was produced from a 40 kV and 40 mA X-Ray tube. Diffract meter is an apparatus used to determine the angles at which diffraction occurs for powdered specimens. Diffraction angle, 2θ was scanned from 10° to 90° with a step of 0.002° . XRD-Diffraction pattern has been evaluated by using Bruker Diffract plus Eva package programs.



Figure 3.8. The image of Bruker AXS D8 Advanced type powder diffract meter

3.4. Four Points D.C. Conductivity Measurement System

For electrical conductivity measurements of the specimens, the standard four-point contact technique has been used. Four-point DC measuring system used in this work, enclose a PC, IEEE-488.2 Bus, Interface card, multimeter (Keithley brand 2700), programmable current source (Keithley brand 2400) and a package programs specially

designed for this purpose. All measurements were carried out with DAQ (Data Acquisition) control system.

Platinum wires, 0.5 mm in diameter, were stuck directly to the pellets with high conductivity silver paste. Often direct contact was preferred to avoid from the contact resistance. The distance between the contact points was about kept 2mm.

The electrical conductivity of solid electrolytes (powder and thin layer) has been measured as a function of temperature. In order to determine the actual temperature of the conductivity during measurement, a k-type thermocouple was placed at a distance of 2-3 mm away from the sample (Figure 3.10).



Figure 3.9. Computer controlled electrical conductivity measurement system

For conductivity measurements, ceramic conductivity measurement kit (Figure 3.10), a specially designed and manufactured by our research group, was used

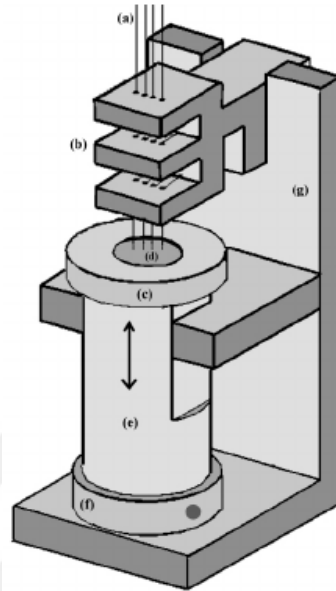


Figure 3.10. Alumina conductivity measurement kit

The conductivity versus temperature characteristics was obtained by injecting a current of $0.5\mu\text{A}$ through the outermost contacts and measuring the voltage drop between the inner contacts (Figure. 3.11). To determine the sample conductivity as a function of temperature, sample was heated in furnace from room temperature to $1100\text{ }^\circ\text{C}$ with a ramping rate of $1.2\text{ }^\circ\text{C}/\text{min}$ to avoid any possible temperature gradient.

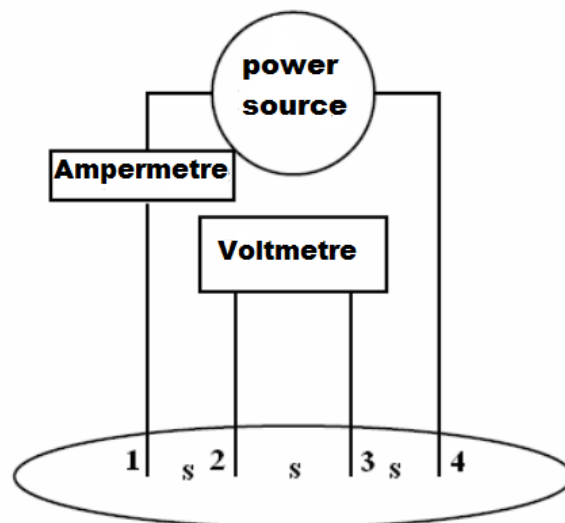


Figure 3.11. Four Points D.C. Electrical Conductivity Measurement Technique

3.4.1. Calculation of Activation Energy

Activation energy is the energy required to initiate a reaction, such as diffusion. Activation energies were calculated by determining the electrical conductivity values of the samples with the highest conductivity, one of the material characteristics.

In addition to that, the electrons and anions are a negative charge, electron cavities and cations are positive charge carriers. The conductivity equation for these load carriers is given by the Arrhenius equation in Eq. (3.1) [82, 83, 84, 85].

$$\sigma = \sigma_0 \cdot e^{\frac{-E_a}{R.T}} \quad (K_B=R/N_A) \quad (3.1)$$

Where σ is the conductivity and σ_0 is the pre-conductivity value in units of kelvin. R is the ideal gas constant ($R=8.63 \times 10^{-5} \text{ eV} \cdot \text{K}^{-1} \cdot \text{atom}^{-1}$) and E_a represent the activation energy in the conductivity equation.

In the conductivity mechanism of ionic conductors, ions move from the lattice points where they are present to other vacant lattice points, leading to conductivity. In this case, the activation energy, in this ionic conduction mechanism that occurs with the movement of ions, is the threshold energies that ions need to move from one position to another vacant position. The activation energy can be determined from the previously given conductivity equation (3.1) by taking ln of both side of equation [84-86].

$$\ln(\sigma) = -\left(\frac{E_a}{R}\right) \cdot \frac{1}{T} + \ln \sigma_0 \quad (3.2)$$

$$\ln\left(\frac{\sigma_1}{\sigma_2}\right) = -\left(\frac{E_a}{R}\right) \cdot \left(\frac{1}{T_1} - \frac{1}{T_2}\right) \quad (3.3)$$

The conductivity variation in this equation is obtained by experimental methods. The graph to be drawn $\left(\ln(\sigma) - \frac{1}{T}\right)$ with the obtained data is as shown in Figure (3.13).

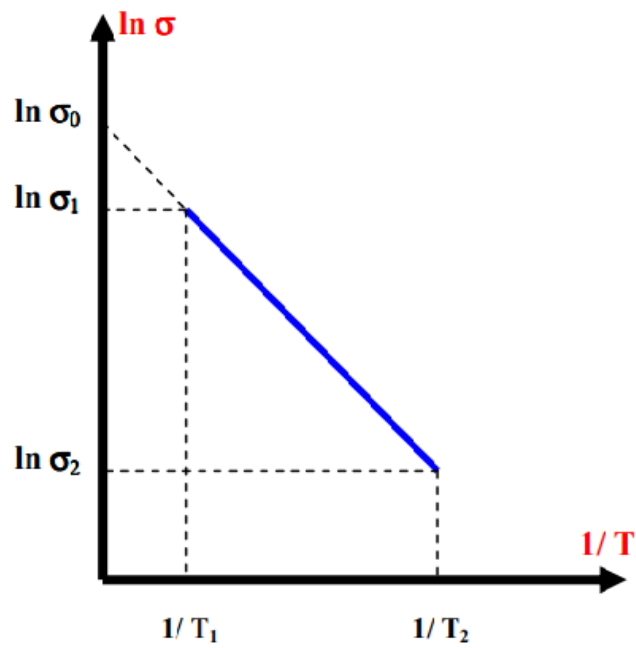


Figure 3.12. $\ln(\sigma) - \frac{1}{T}$ Chart

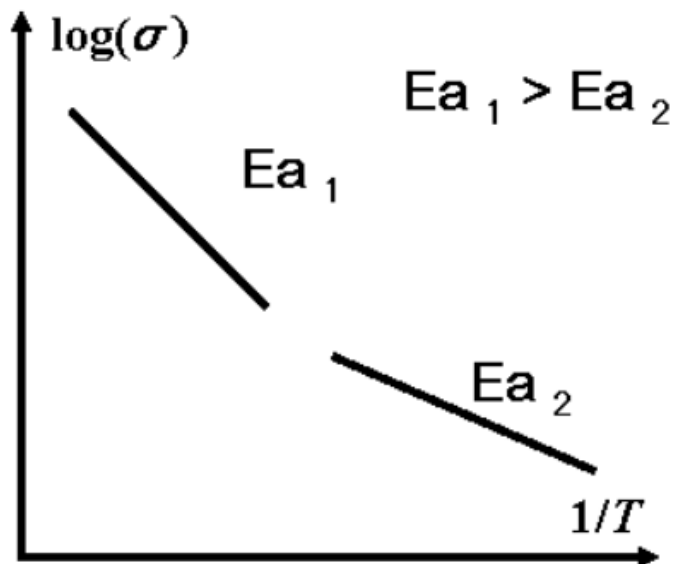


Figure 3.13. Second region $\ln(\sigma) - \frac{1}{T}$ graph

In this calculation, the temperatures T_1 and T_2 are in absolute temperature in term of Kelvin (K) and σ_1 and σ_2 are the conductivity at these temperature respectively.

Conductivity is usually given in units of $(\Omega \cdot \text{cm})^{-1}$. The obtained activation energy value is based on eV.

The constant activation energy indicates that the conductivity mechanism remains constant over the temperature range at which it is constant. When the mechanism of conductivity changes, the energy value also changes. The change in the mechanism of conductivity also refers to the effects of crystal structure and the change in the state of carrier loads.

In studies of Arrhenius curves of materials with oxygen-ionic conductivity, it is widely known that Arrhenius curves of these materials are bi-polar [87-90]. The curve shows a steady increase in the range of a certain temperature range and shows a high conductivity with a sudden jump at a critical temperature and shows a constant slope from this point. It has been reported that phase transformation takes place around this temperature, which is caused by fracture of the conductivity curve. This can be shown in the graphs in Figure (3.13).

CHAPTER 4

CHARACTERIZATION OF ELECTROLYTES

4.1. $(\text{Bi}_2\text{O}_3)_{1-x-y-z} (\text{Dy}_2\text{O}_3)_x (\text{Eu}_2\text{O}_3)_y (\text{Tm}_2\text{O}_3)_z$ Quaternary System

The $(\text{Bi}_2\text{O}_3)_{1-x-y-z} (\text{Dy}_2\text{O}_3)_x (\text{Eu}_2\text{O}_3)_y (\text{Tm}_2\text{O}_3)_z$ quaternary system with a nominal composition of, $x=5$ mole; $y=5$ mole; $z=5, 10, 15, 20$ molar ratios, $x=5$ mole ; $y=5, 10, 15, 20$ molar ratios, $z=5$ mole; and $x=5, 10, 15, 20$ molar ratios; $y=5$ mole; $z=5$ mole in percentages, were prepared by solid state reaction. Mole ratios of compounds used for each sample (M1-M10) are listed in Table 4.1.

Samples were heated up with a ramping rate of $8\text{ }^\circ\text{C}/\text{min}$. from room temperature to desired annealing temperature of $750\text{ }^\circ\text{C}$, and annealed at $750\text{ }^\circ\text{C}$ for 100 h. Then it has been left to cool down to room temperature by simply turning of the furnace.

XRD, DTA/TG/DTG analyses and Four-point DC conductivity measurements of the prepared samples were carried out. The following are the results of the analyses and electrical conductivity measurements obtained for each sample.

Table 4.1. The molar percentages of Dy_2O_3 , Eu_2O_3 , Tm_2O_3 , and Bi_2O_3 base materials

Sample	Dy_2O_3 (mol%)	Eu_2O_3 (mol%)	Tm_2O_3 (mol%)	Bi_2O_3 (mol%)
M1	5	5	5	85
M2	5	5	10	80
M3	5	5	15	75
M4	5	5	20	70
M5	5	10	5	80
M6	5	15	5	75
M7	5	20	5	70
M8	10	5	5	80
M9	15	5	5	75
M10	20	5	5	70

4.1.1. X-Ray Analysis

X-ray diffraction (XRD) patterns of all prepared samples (M1-M10) as synthesized and after conductivity measurement are given in Figure 4.1-4.10. X-ray diffraction patterns of a series of compound of $\text{Bi}_2\text{O}_3)_{0.90-z} (\text{Dy}_2\text{O}_3)_{0.05} (\text{Eu}_2\text{O}_3)_{0.05} (\text{Tm}_2\text{O}_3)_z$ with an increasing $(\text{Tm}_2\text{O}_3)_z$ ($z=0.05-0.20$) shows that Bi_2O_3 based solid electrolytes with fcc fluorite type structure of bismuth oxide (δ - Bi_2O_3) may be obtained easily. δ - Bi_2O_3 is a dominant phase together with monoclinic α - Bi_2O_3 phase or impurities for low Tm_2O_3 , but impurities decrease when Tm_2O_3 has increased in as synthesized sample (Figure 4.1-4.4).

X-ray diffraction patterns taken after the conductivity measurements reveal that all samples convert to the δ - Bi_2O_3 phase and α - Bi_2O_3 phase disappeared. The reason for that probably high temperature exposed during conductivity measurement. At high temperature some ions will gain mobility and easily they are droved by the electrical force provided by electrical field used for conductivity measurement. Thus reorganization of atoms at a stable phase will be possible.

X-ray diffraction patterns of a series of compound of $(\text{Bi}_2\text{O}_3)_{0.90-y} (\text{Dy}_2\text{O}_3)_{0.05} (\text{Eu}_2\text{O}_3)_y (\text{Tm}_2\text{O}_3)_{0.05}$ with an increasing $(\text{Eu}_2\text{O}_3)_y$ ($y=0.05-0.20$) shows that α - Bi_2O_3 phase and some impurities is being formed together with δ - Bi_2O_3 when concentration of Eu_2O_3 increase in as synthesized sample. After the conductivity measurements, all samples reduce to δ - Bi_2O_3 phase due to high temperature exposed during conductivity measurement (Figure 4.5-4.7).

For the last series of compound of $\text{Bi}_2\text{O}_3)_{0.90-x} (\text{Dy}_2\text{O}_3)_x (\text{Eu}_2\text{O}_3)_{0.05} (\text{Tm}_2\text{O}_3)_{0.05}$ with an increasing $(\text{Dy}_2\text{O}_3)_x$ ($x=0.05-0.20$), minor amount of impurity phases has been detected except for δ - Bi_2O_3 on X-ray diffraction patterns, when concentration of Dy_2O_3 has been increased in as synthesized sample (Figure 4.8-4.10). These impurity phases cleared away after the conductivity measurement.

From the evaluation of X-ray diffraction patterns, it can be concluded that all composition used here allows to get δ - Bi_2O_3 , which has intrinsic oxide ion vacancies critical for ionic conductivity, after the conductivity measurement (Figure 4.11-4.13).

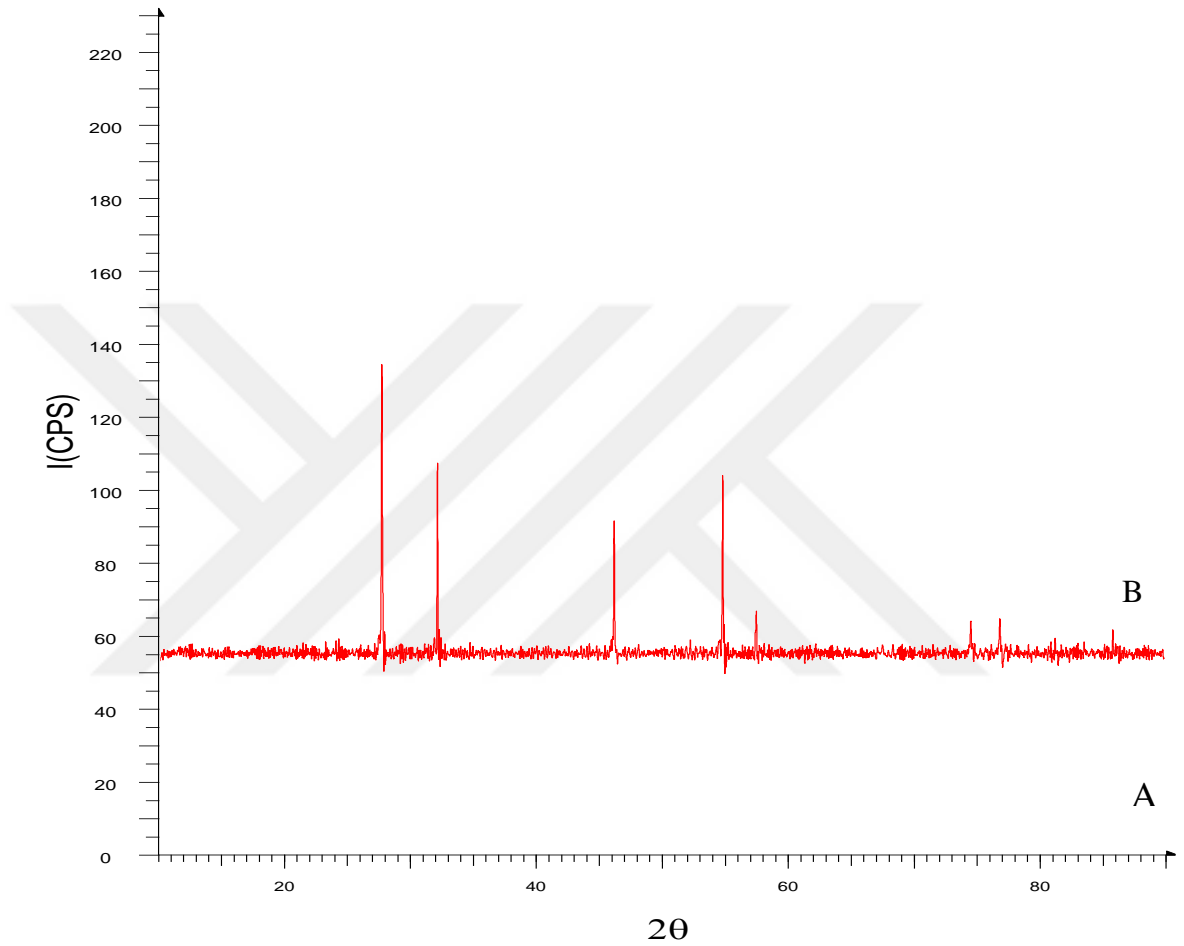


Figure 4.1. XRD patterns of $(\text{Bi}_2\text{O}_3)_{0.85} (\text{Dy}_2\text{O}_3)_{0.05} (\text{Eu}_2\text{O}_3)_{0.05} (\text{Tm}_2\text{O}_3)_{0.05}$ (sample M1), (A) Before electrical conductivity measurement (B) After electrical conductivity measurement.

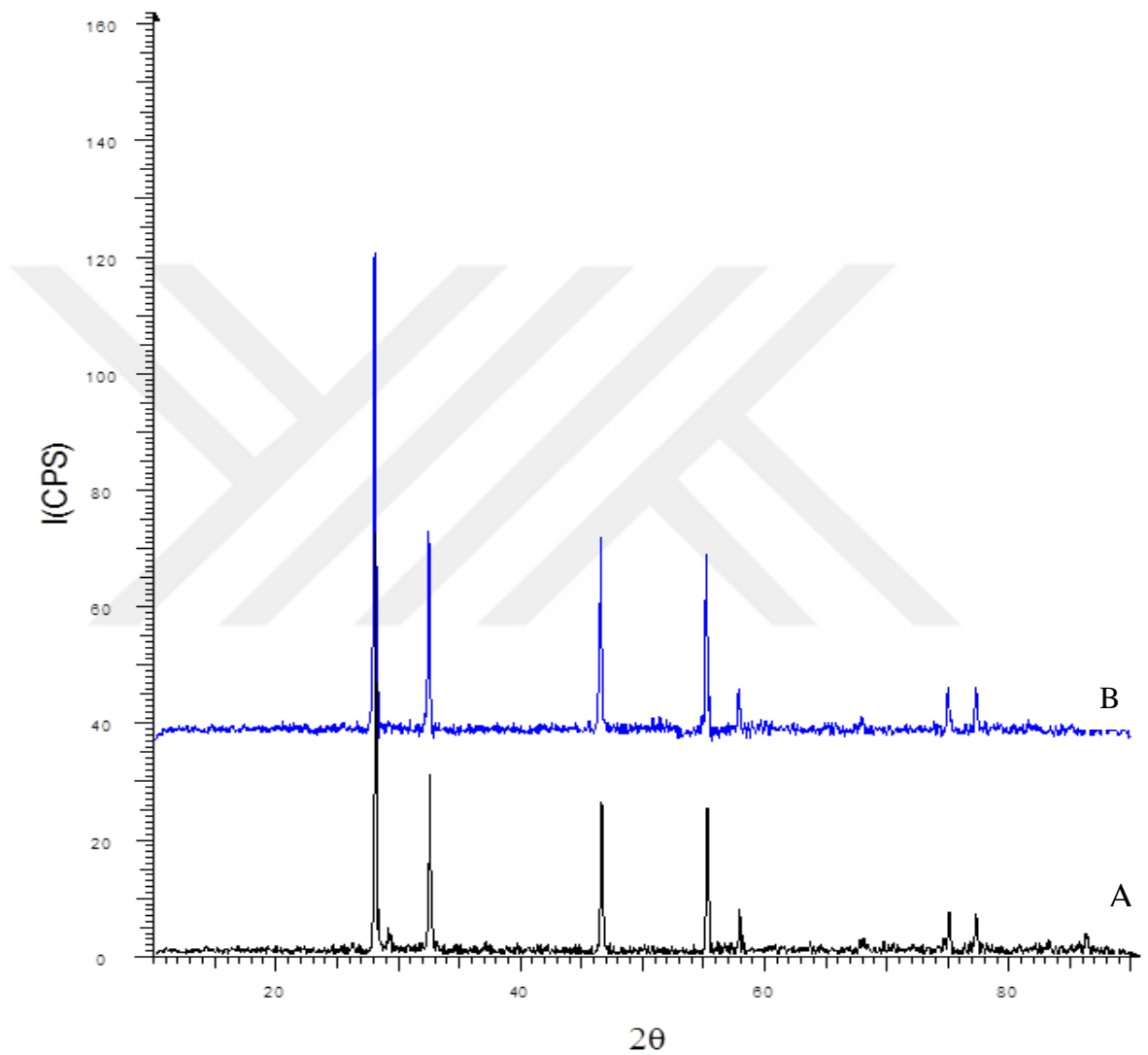


Figure 4.2. XRD patterns of $(\text{Bi}_2\text{O}_3)_{0.80} (\text{Dy}_2\text{O}_3)_{0.05} (\text{Eu}_2\text{O}_3)_{0.05} (\text{Tm}_2\text{O}_3)_{0.10}$ (sample M2), (A) Before electrical conductivity measurement (B) After electrical conductivity measurement.

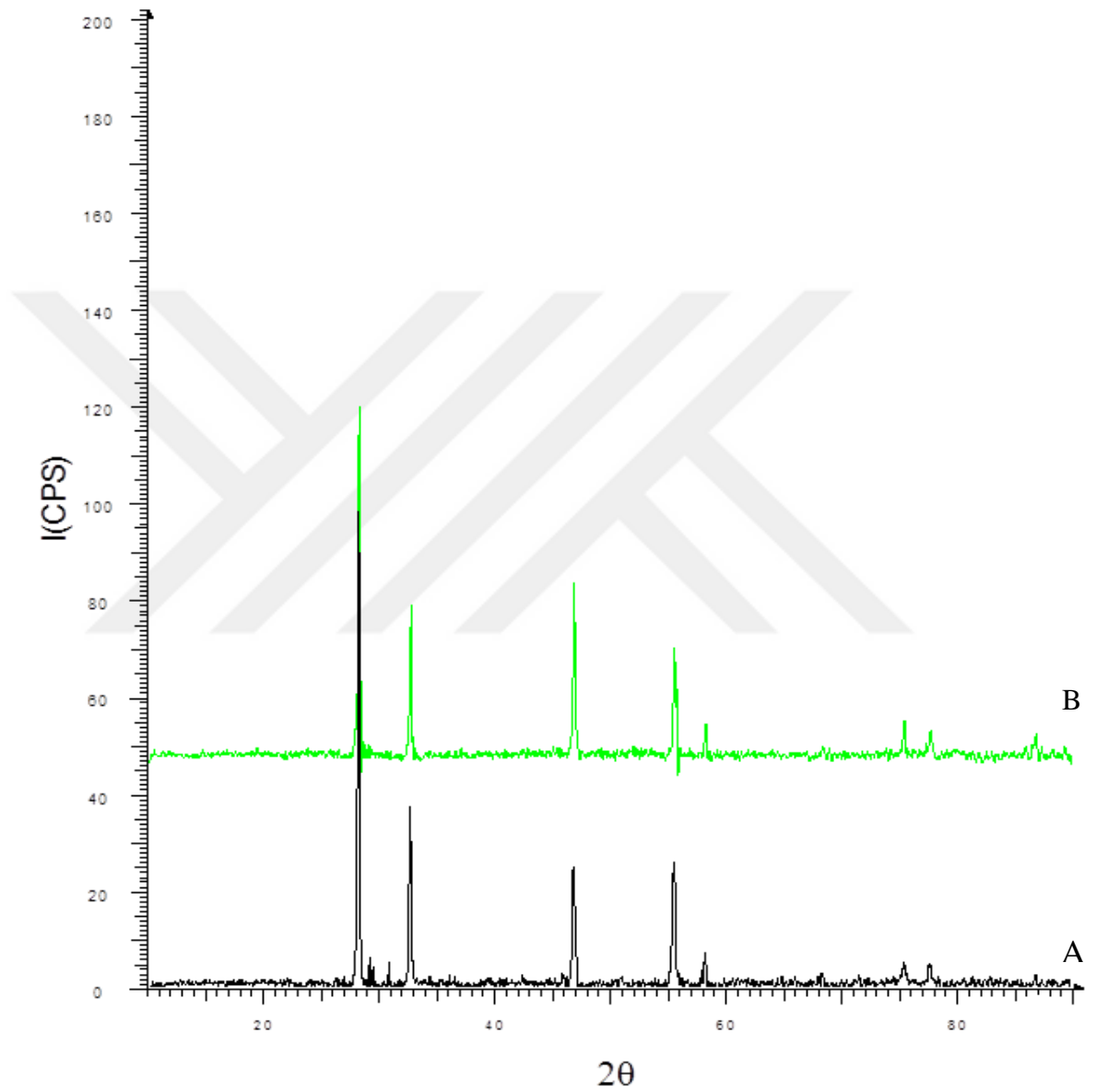


Figure 4.3. XRD patterns of $(\text{Bi}_2\text{O}_3)_{0.75} (\text{Dy}_2\text{O}_3)_{0.05} (\text{Eu}_2\text{O}_3)_{0.05} (\text{Tm}_2\text{O}_3)_{0.15}$ (sample M3), (A) Before electrical conductivity measurement (B) After electrical conductivity measurement.

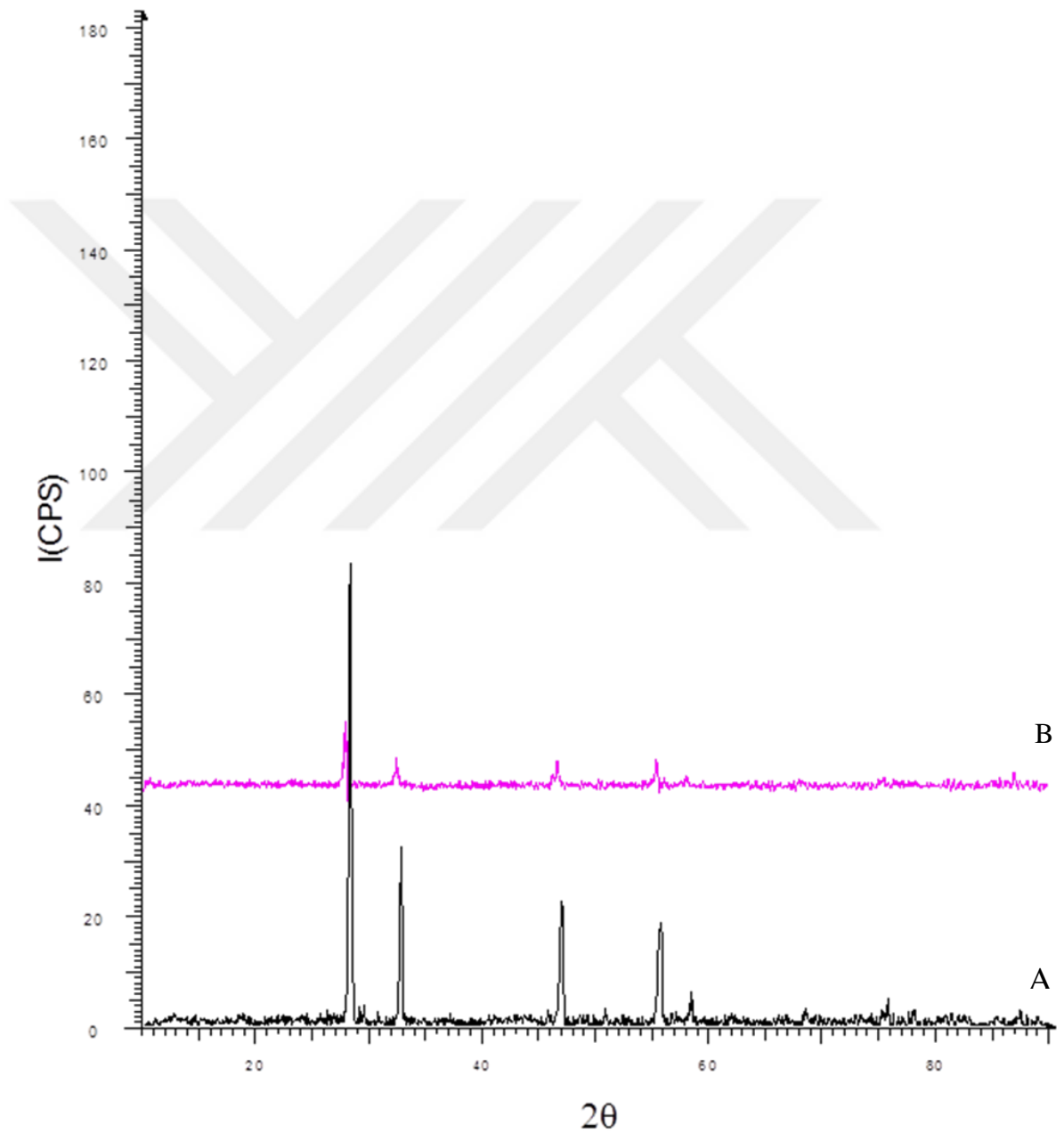


Figure 4.4. XRD patterns of $(\text{Bi}_2\text{O}_3)_{0.70} (\text{Dy}_2\text{O}_3)_{0.05} (\text{Eu}_2\text{O}_3)_{0.05} (\text{Tm}_2\text{O}_3)_{0.20}$ (sample M4), (A) Before electrical conductivity measurement (B) After electrical conductivity measurement.

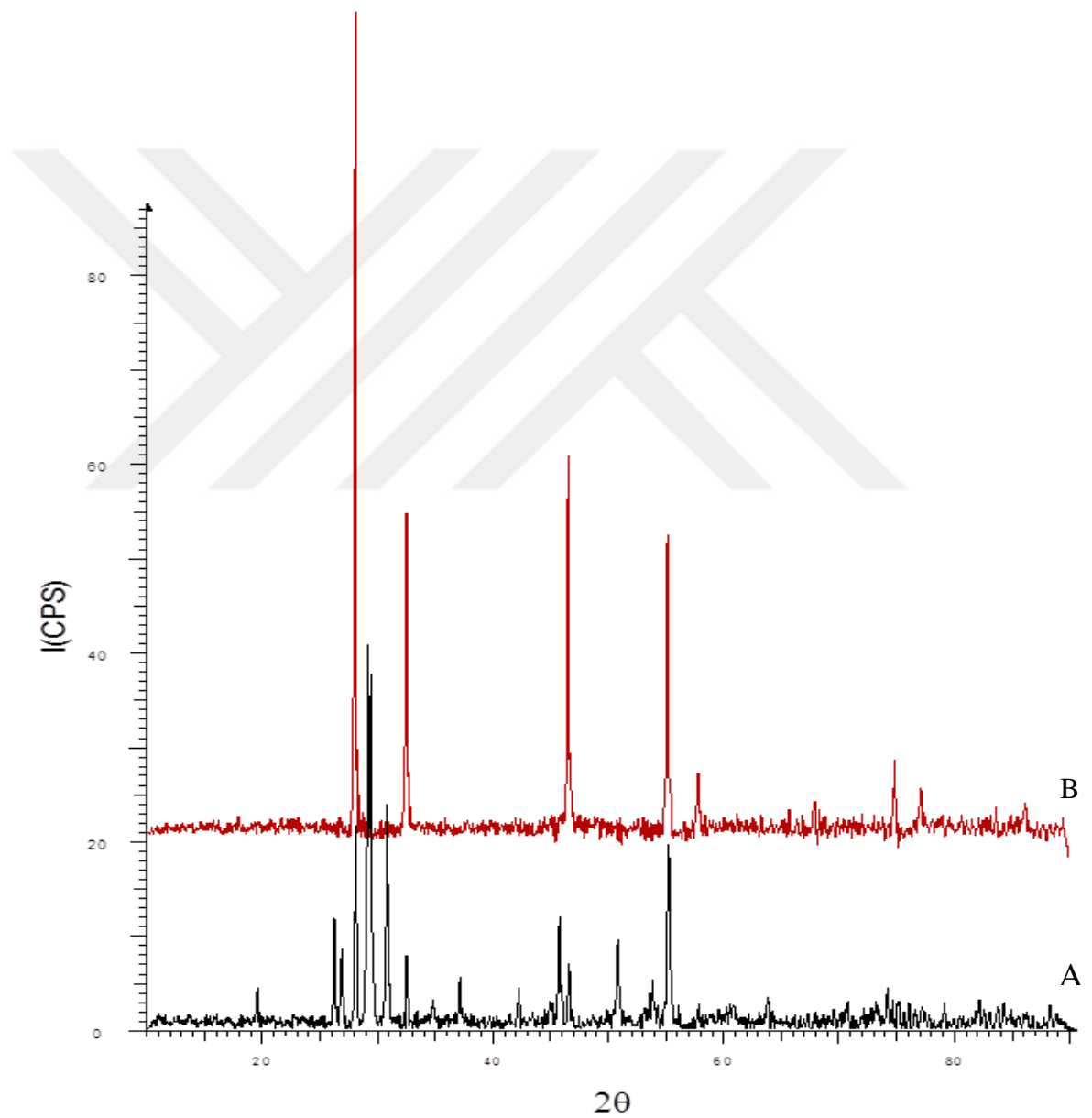


Figure 4.5. XRD patterns of $(\text{Bi}_2\text{O}_3)_{0.80} (\text{Dy}_2\text{O}_3)_{0.05} (\text{Eu}_2\text{O}_3)_{0.10} (\text{Tm}_2\text{O}_3)_{0.05}$ (sample M5), (A) Before electrical conductivity measurement (B) After electrical conductivity measurement.

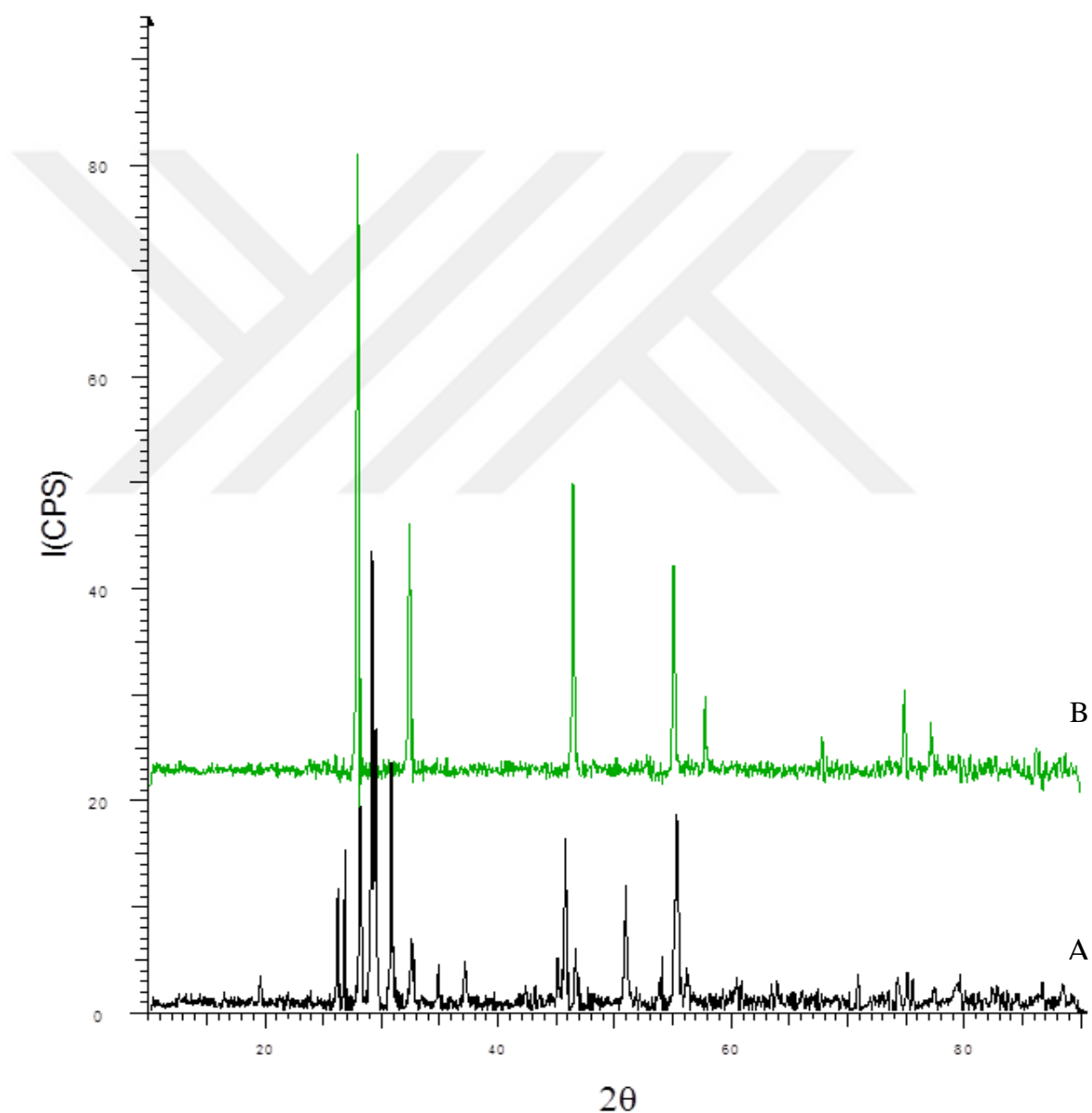


Figure 4.6. XRD patterns of $(\text{Bi}_2\text{O}_3)_{0.75} (\text{Dy}_2\text{O}_3)_{0.05} (\text{Eu}_2\text{O}_3)_{0.15} (\text{Tm}_2\text{O}_3)_{0.05}$ (sample M6), (A) Before electrical conductivity measurement (B) After electrical conductivity measurement.

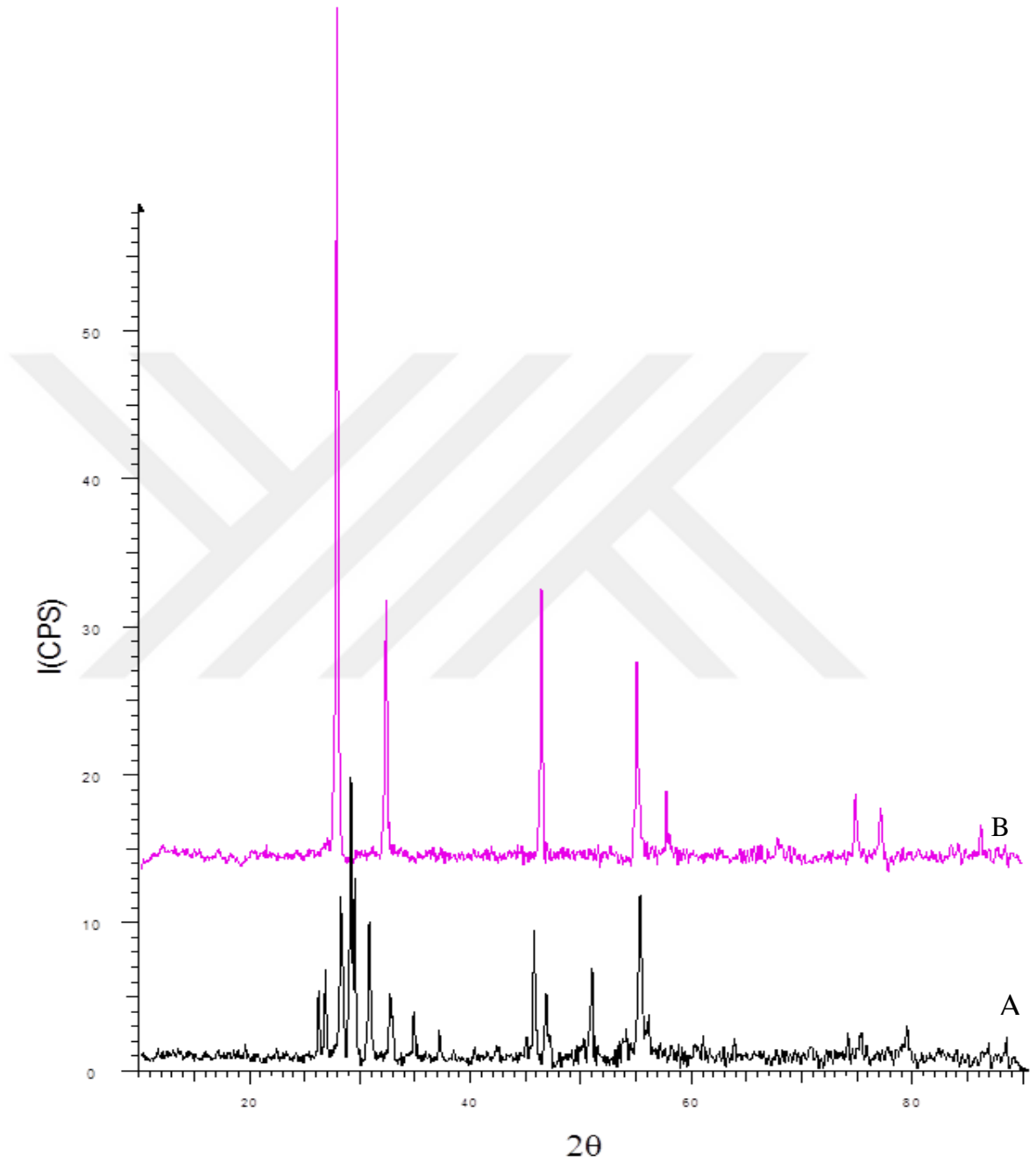


Figure 4.7. XRD patterns of $(\text{Bi}_2\text{O}_3)_{0.70} (\text{Dy}_2\text{O}_3)_{0.05} (\text{Eu}_2\text{O}_3)_{0.20} (\text{Tm}_2\text{O}_3)_{0.05}$ (sample M7), (A) Before electrical conductivity measurement (B) After electrical conductivity measurement.

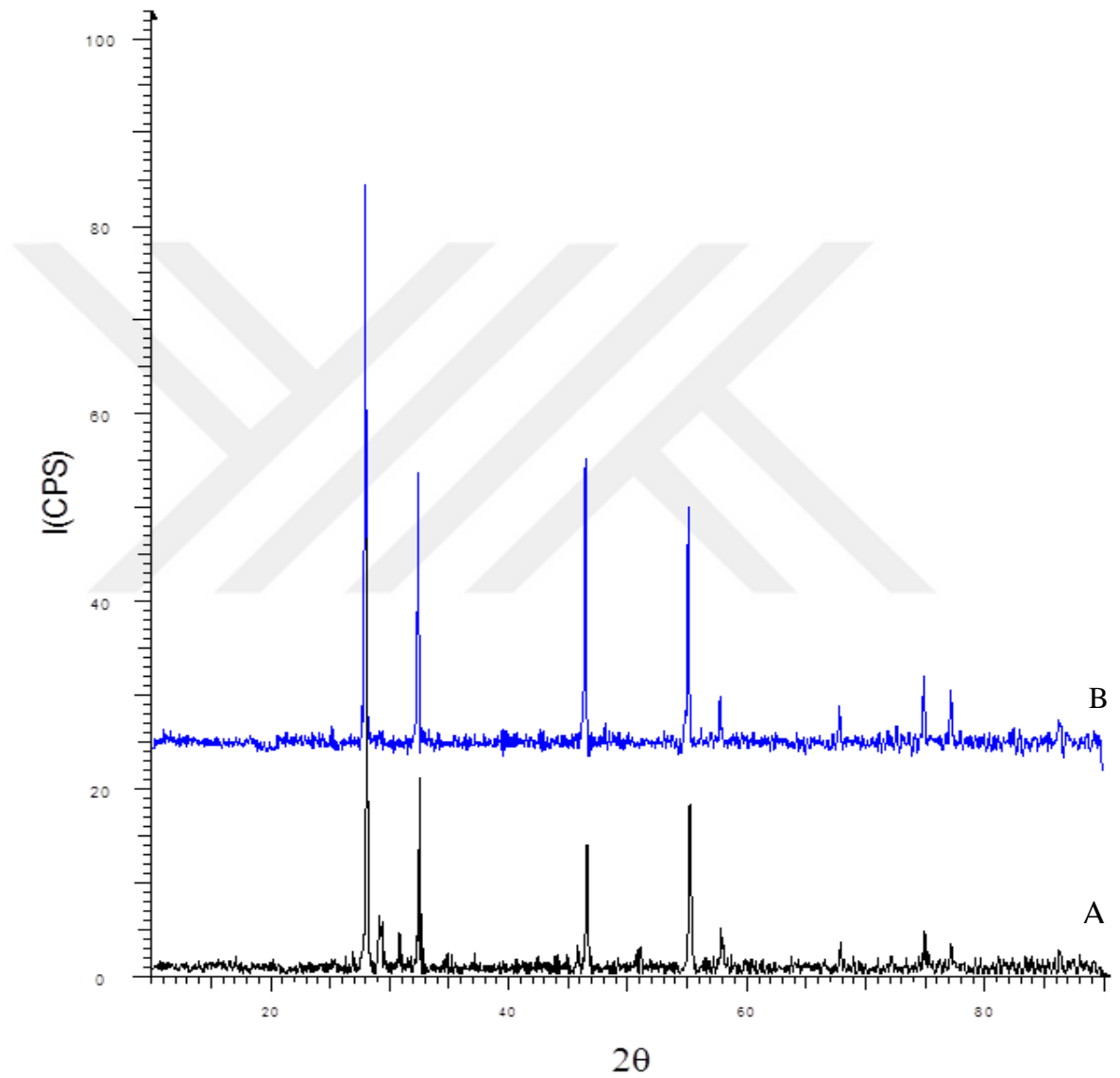
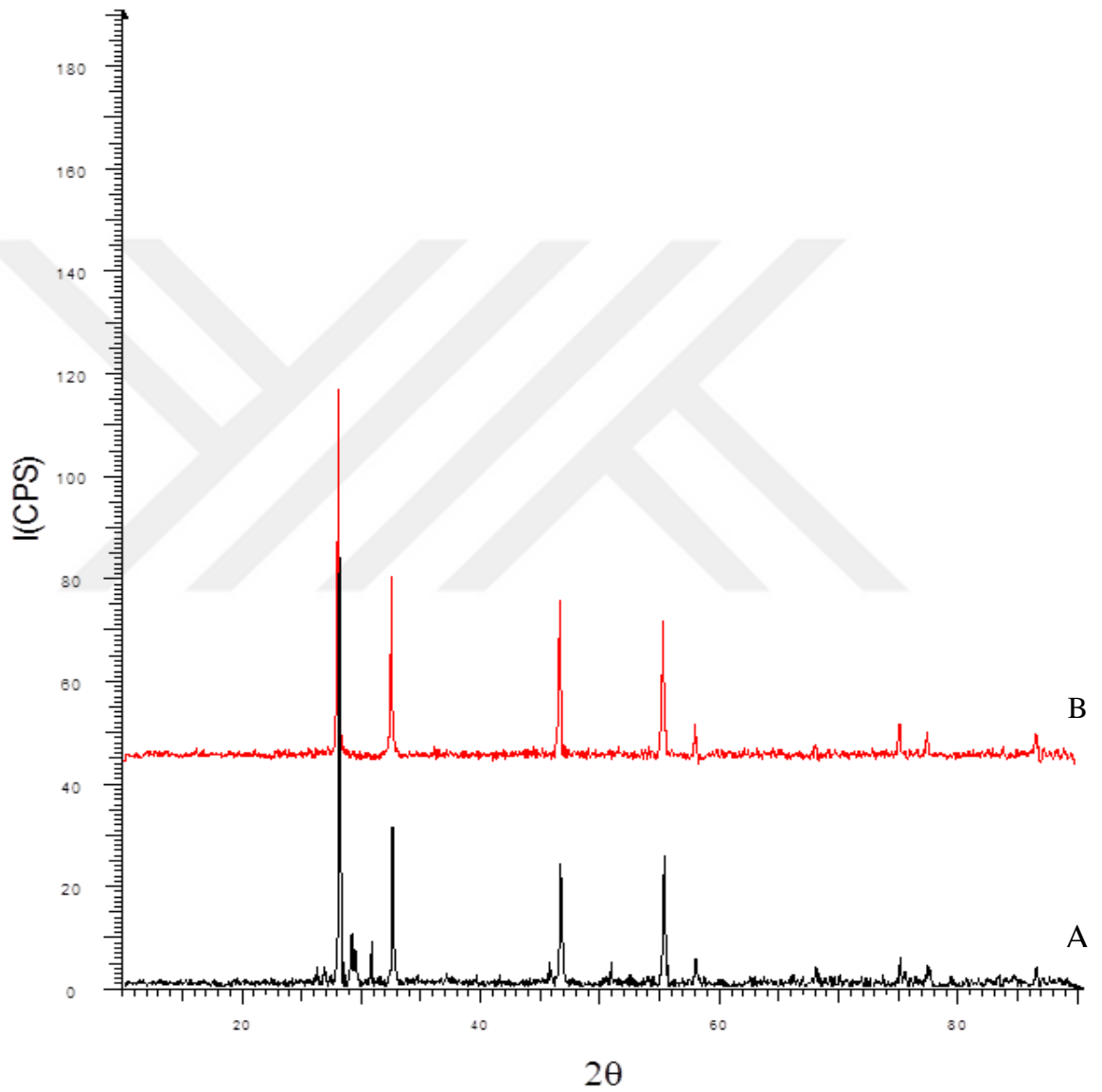


Figure 4.8. XRD patterns of $(\text{Bi}_2\text{O}_3)_{0.80} (\text{Dy}_2\text{O}_3)_{0.10} (\text{Eu}_2\text{O}_3)_{0.05} (\text{Tm}_2\text{O}_3)_{0.05}$ (sample M8), (A) Before electrical conductivity measurement (B) After electrical conductivity measurement.



Figurer 4.9. XRD patterns of $(\text{Bi}_2\text{O}_3)_{0.75} (\text{Dy}_2\text{O}_3)_{0.15} (\text{Eu}_2\text{O}_3)_{0.05} (\text{Tm}_2\text{O}_3)_{0.05}$ (sample M9), (A) Before electrical conductivity measurement (B) After electrical conductivity measurement.

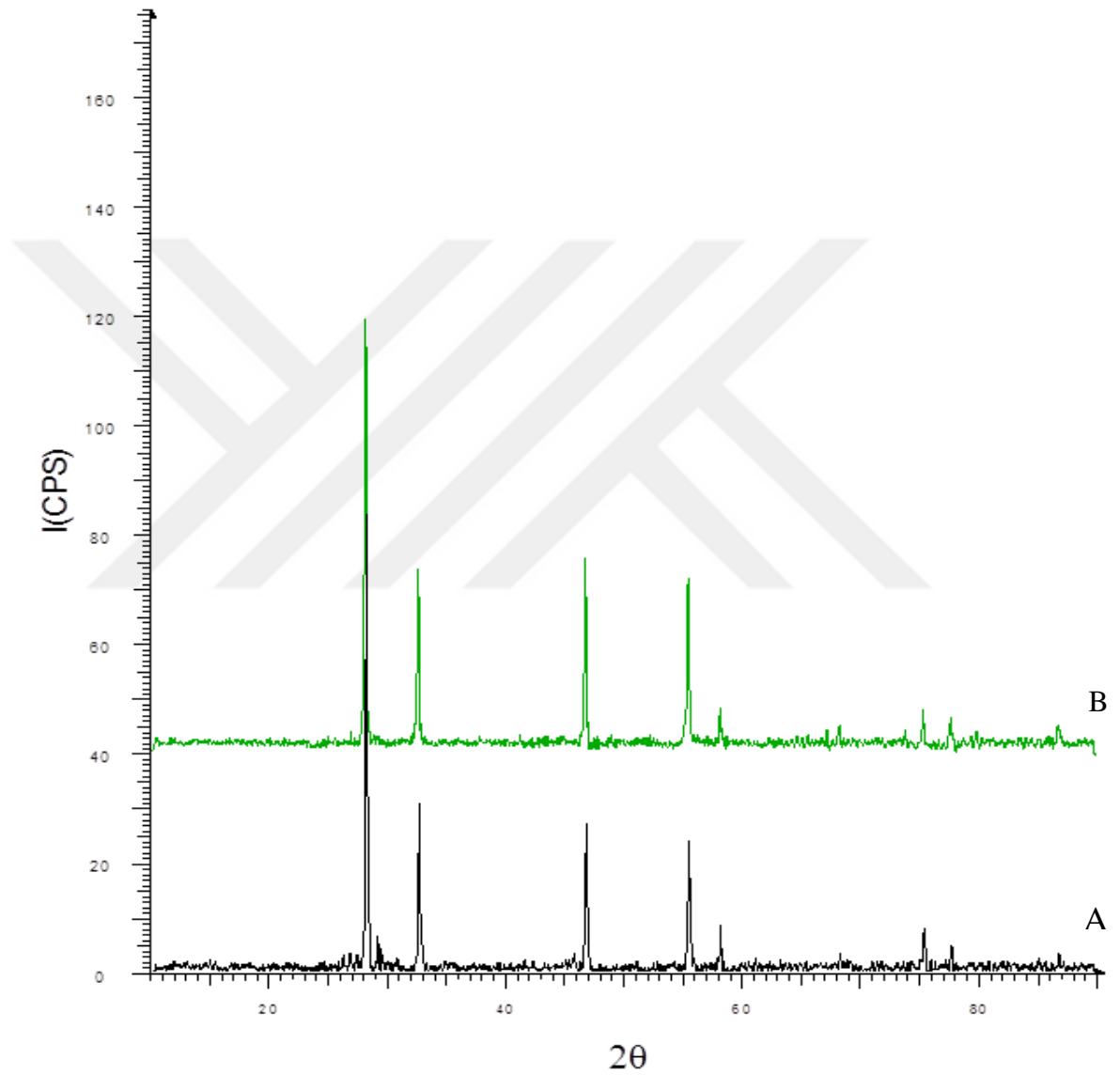


Figure 4.10. XRD patterns of $(\text{Bi}_2\text{O}_3)_{0.70} (\text{Dy}_2\text{O}_3)_{0.20} (\text{Eu}_2\text{O}_3)_{0.05} (\text{Tm}_2\text{O}_3)_{0.05}$ (sample M10), (A) Before electrical conductivity measurement (B) After electrical conductivity measurement.

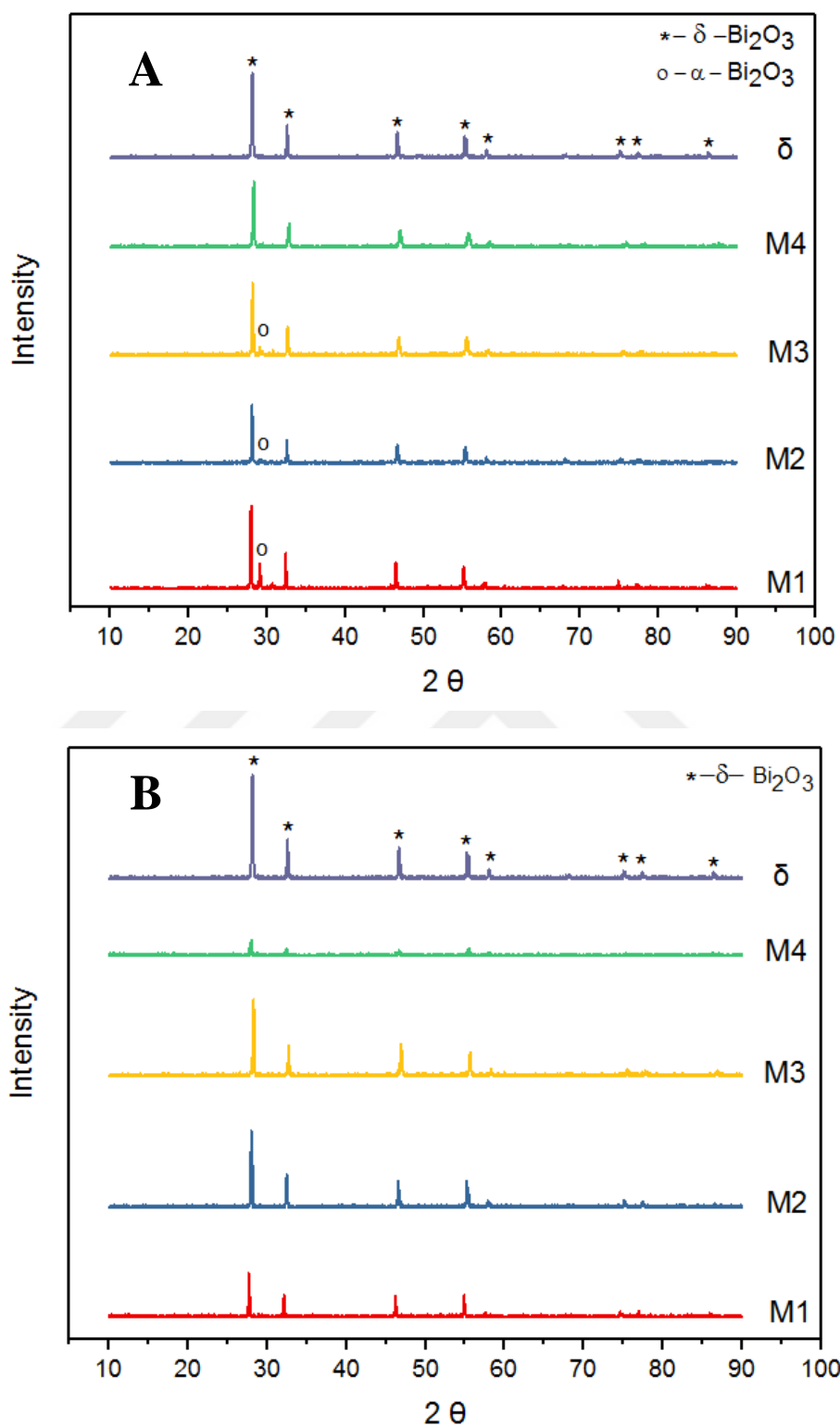


Figure 4.11. Comparison of XRD spectrum of sample M1-M4 with bismuth oxide (δ - Bi_2O_3). (A) Before conductivity measurement. (B) After conductivity measurement.

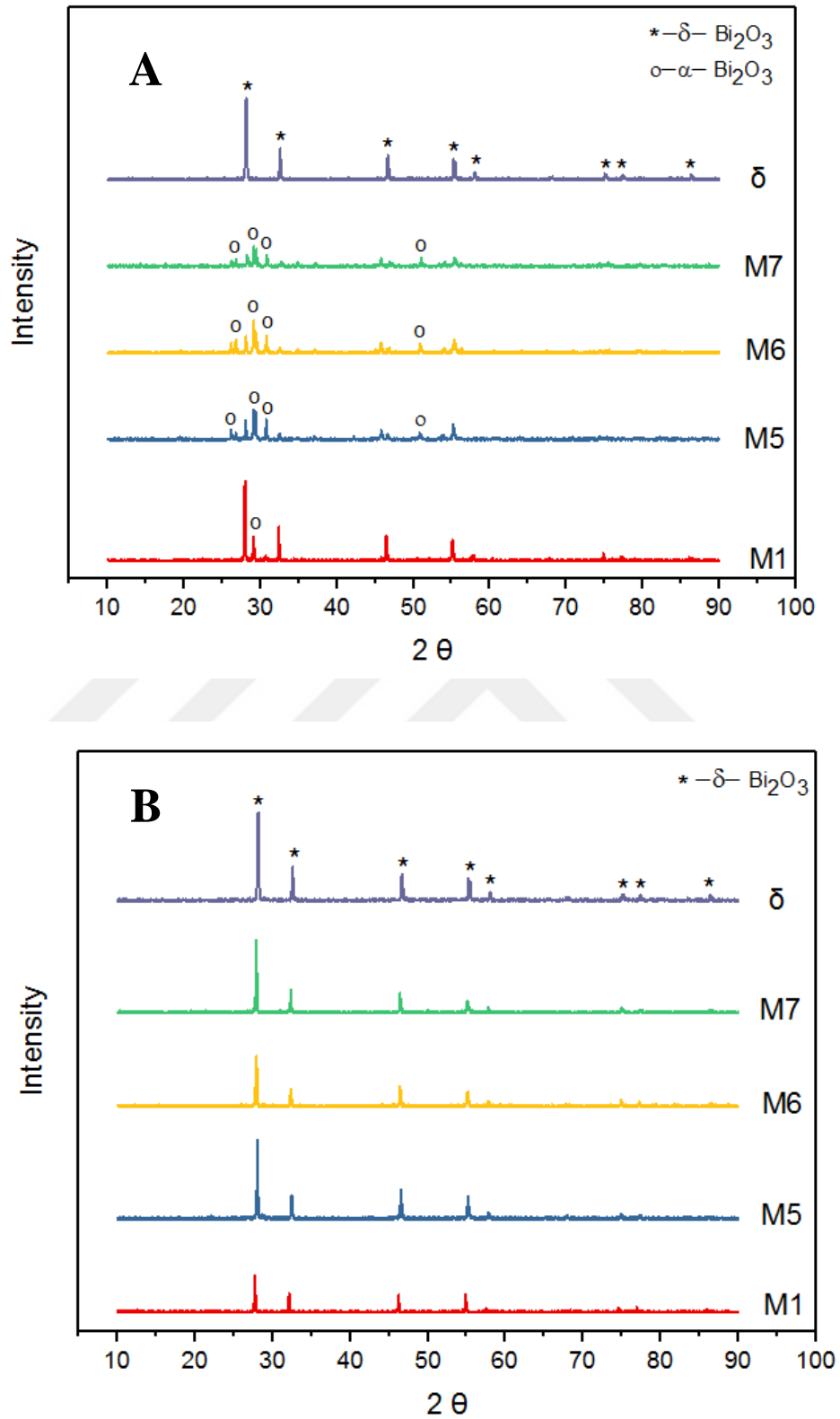


Figure 4.12. Comparison of XRD spectrum of sample M1, M5-M7 with bismuth oxide (δ - Bi_2O_3). (A) Before conductivity measurement. (B) After conductivity measurement.

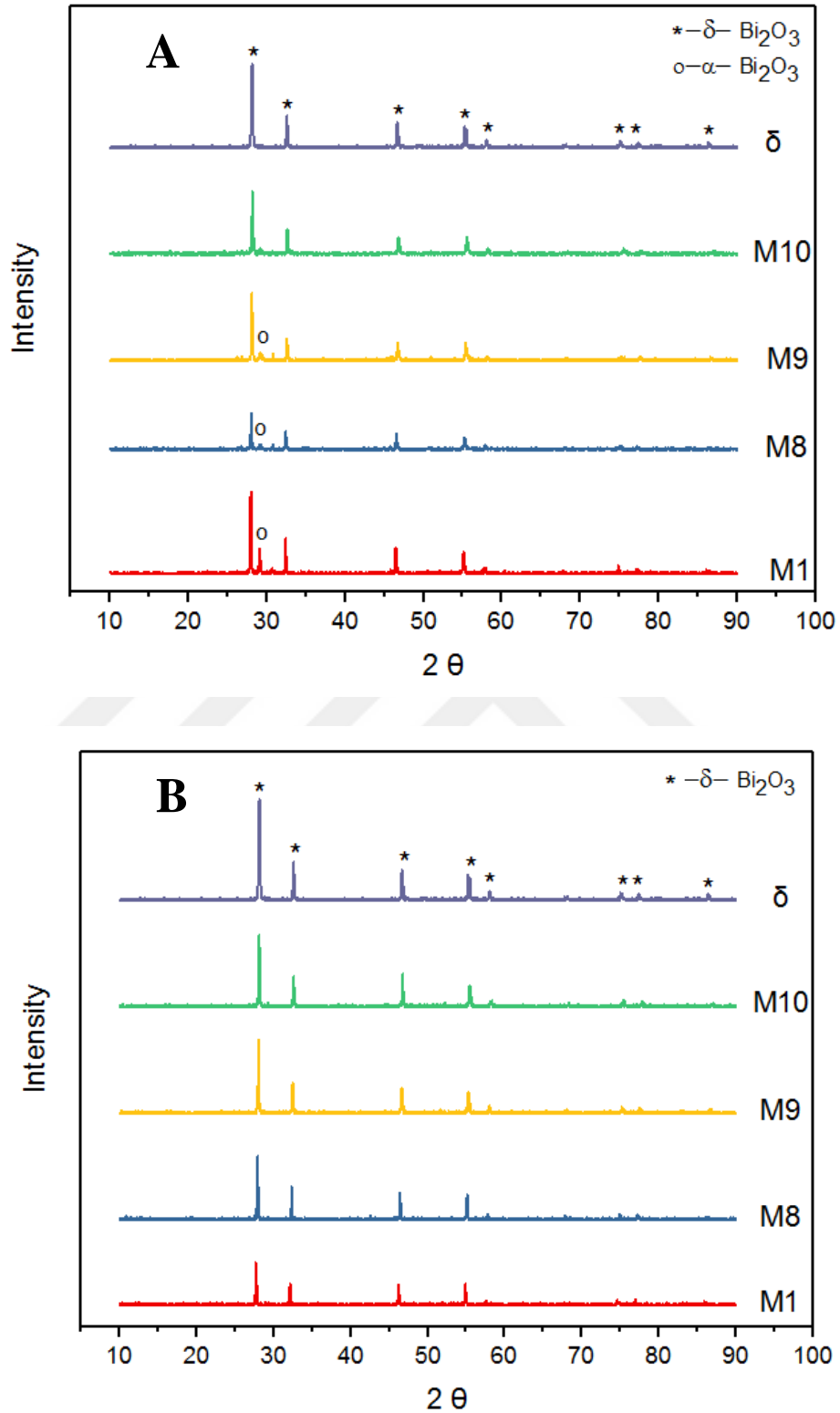


Figure 4.13. Comparison of XRD spectrum of sample M1, M8-M10 with bismuth oxide (δ - Bi_2O_3). (A) Before conductivity measurement. (B) After conductivity measurement.

4.1.2. Thermal Analysis

DTA/TG spectrums of all prepared samples (M1-M10) are given in Figure 4.14-4.24. All spectrum were taken before conductivity measurement.

On heating (upper curve), DTA spectrum of sample M1 shows one endothermic heat effect at about 730 °C which indicates the phase transition of α -Bi₂O₃ to δ -Bi₂O₃. During cooling (bottom curve), there is no deldectable phase transition (Figure 4.14). This reveals that δ -Bi₂O₃ formed during heating is stable.

For sample M2 and M3, no recognizable heat effect detected during either heating or cooling due to miserable volume fraction of α -Bi₂O₃ detected from XRD pattern (Figure 4.14).

For sample M4 a pike looks like one exothermic heat effect at about 450 °C detected on cooling curve, but this is not an exothermic heat effect. This temperature is not the phase transition temperature for Bi₂O₃. However, it was recognized from XRD pattern of sample M4 after conductivity measurement all peaks slightly shifted small 2θ angles and the intensity of all peaks decreased.

For sample M5 only one endothermic heat effect occur at about 750 °C on heating curve which corresponds to transformation of α -phase to δ -phase on heating curve.

However sample M6 and M7 there is no deldectable phase transition in despite of large amount of α -Bi₂O₃ phase. It can be attributed sample weight which is less than 10 mg.

For sample M8 only one endothermic heat effect occur at about 740 °C on heating curve which corresponds to transformation of α -phase to δ -phase on heating curve.

But sample M9 and M10 there is no deldectable phase transition may be because of very small amount of volume fraction of α -Bi₂O₃ or sample weight which is less than 10 mg. TG curve reveals a very slow and gradual mass decrease. The observed mass change in the TG curve corresponds to volatilization of the Bi₂O₃.

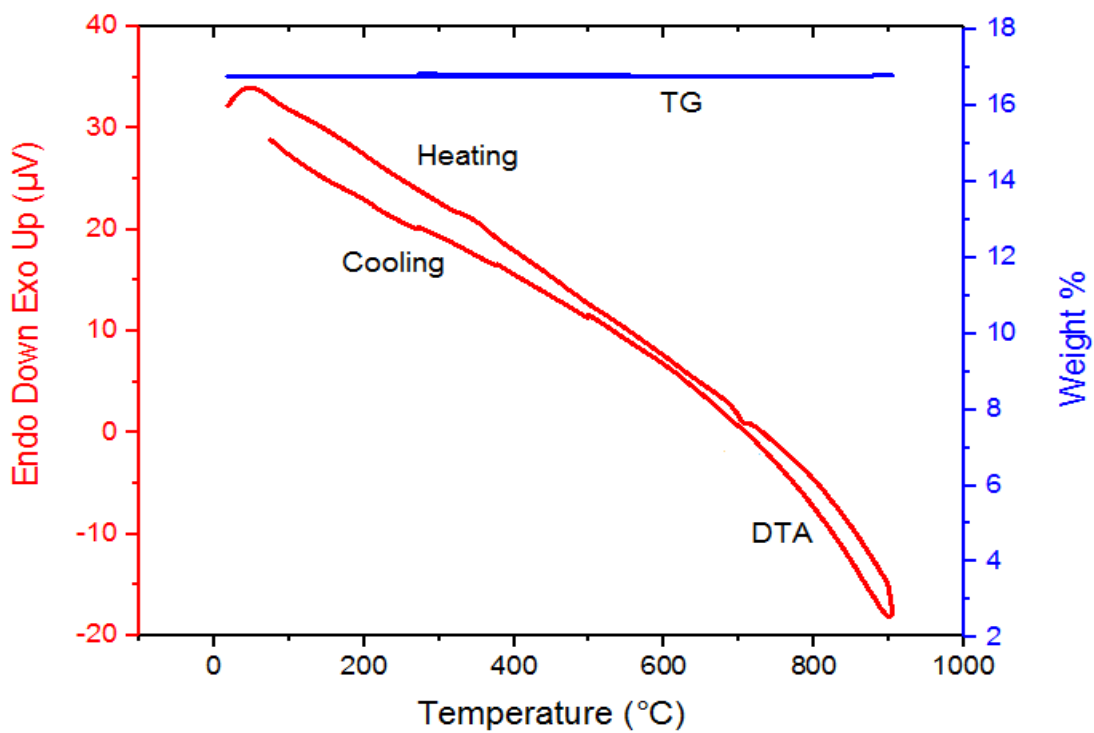


Figure 4.14. DTA/TG spectrum for M1 (Sample Weight: 16.783 mg).

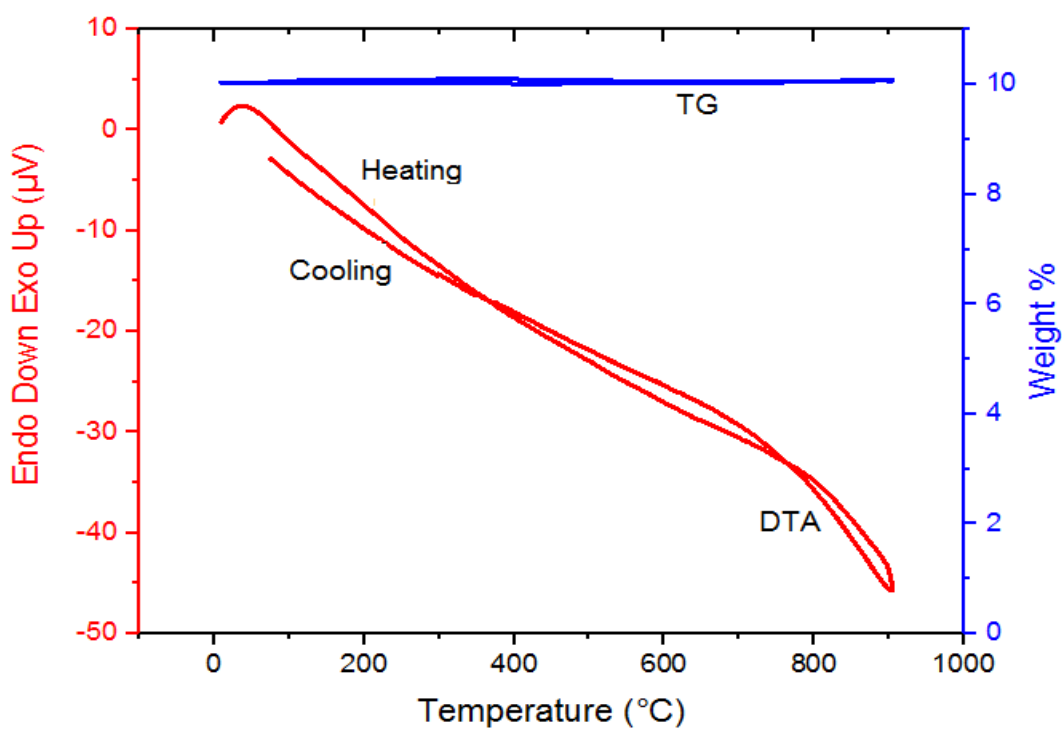
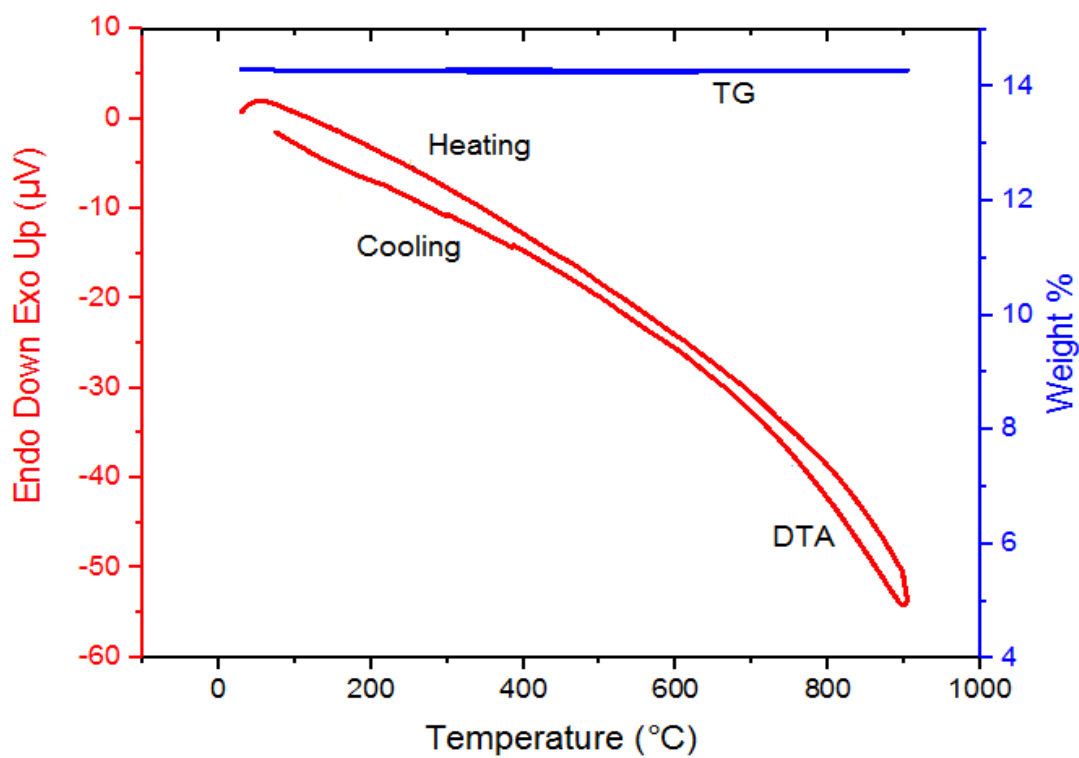
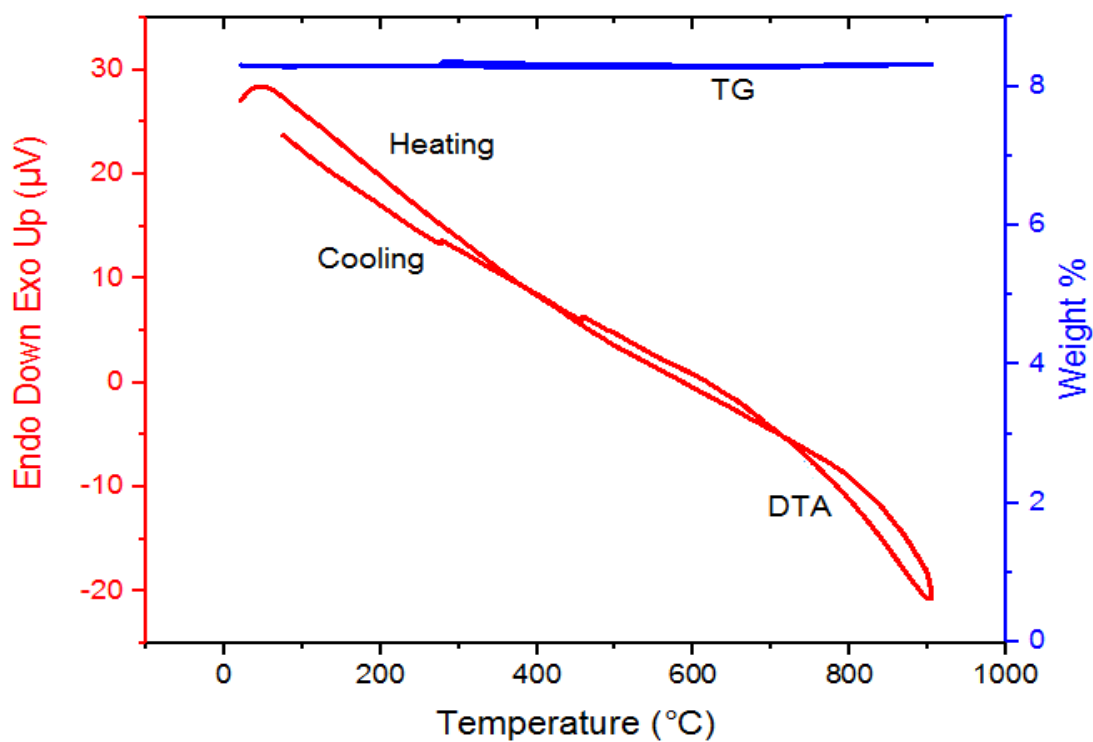


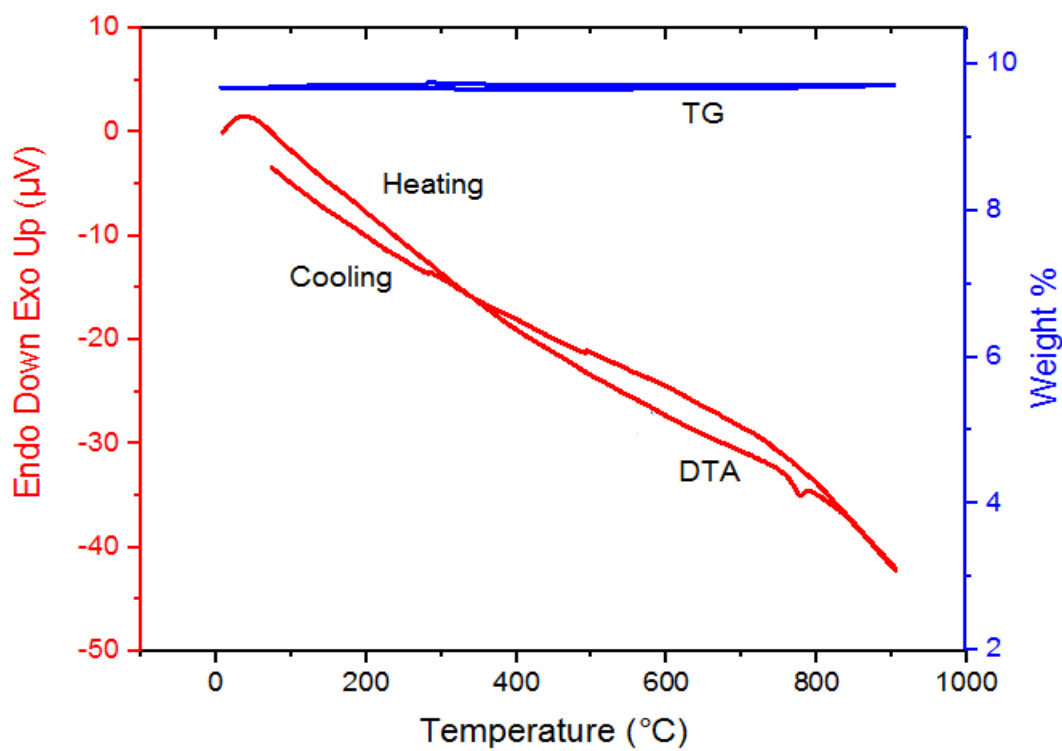
Figure 4.15. DTA/TG spectrum for M2 (Sample Weight: 10.044 mg).



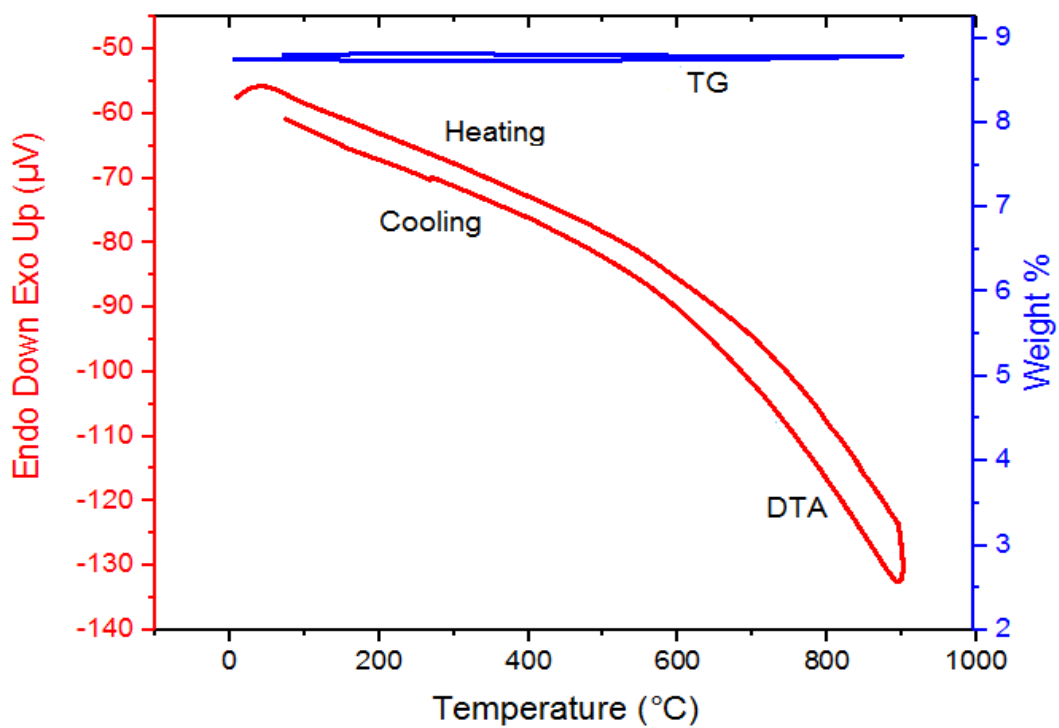
Figurer 4.16. DTA/TG spectrum for M3 (Sample Weight: 14.303 mg).



Figurer 4.17. DTA/TG spectrum for M4 (Sample Weight: 8.314 mg).



Figurer 4.18. DTA/TG spectrum for M5 (Sample Weight: 9.683 mg).



Figurer 4.19. DTA/TG spectrum for M6 (Sample Weight: 8.753 mg).

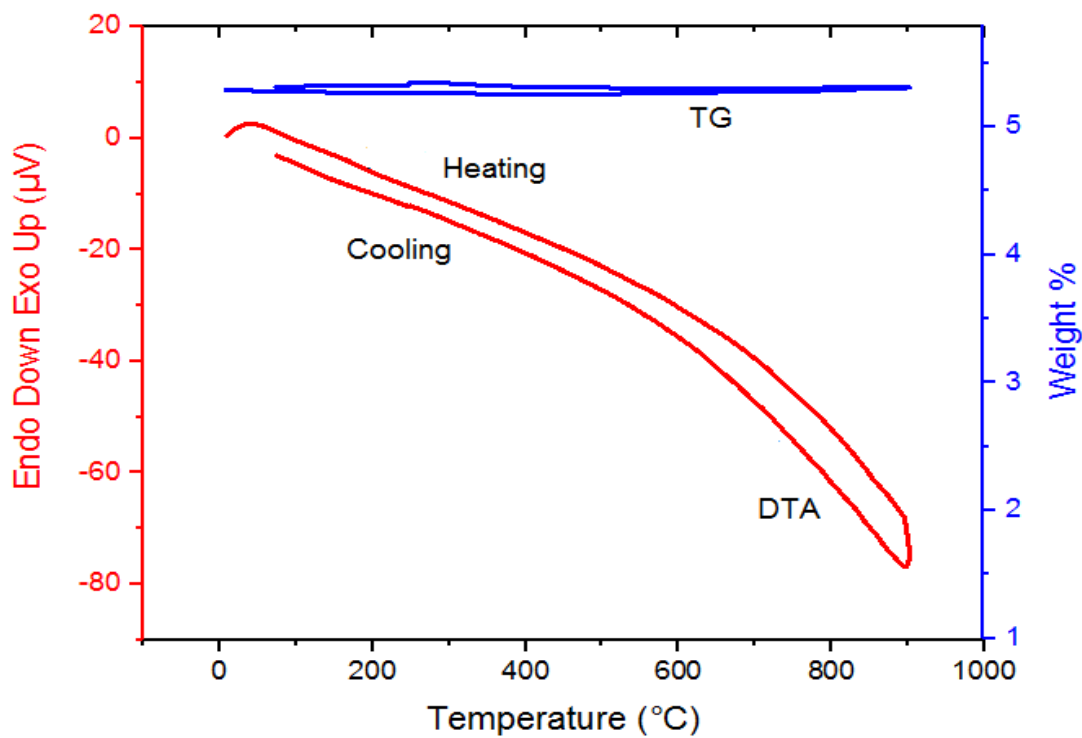


Figure 4.20. DTA/TG spectrum for M7 (Sample Weight: 5.296 mg).

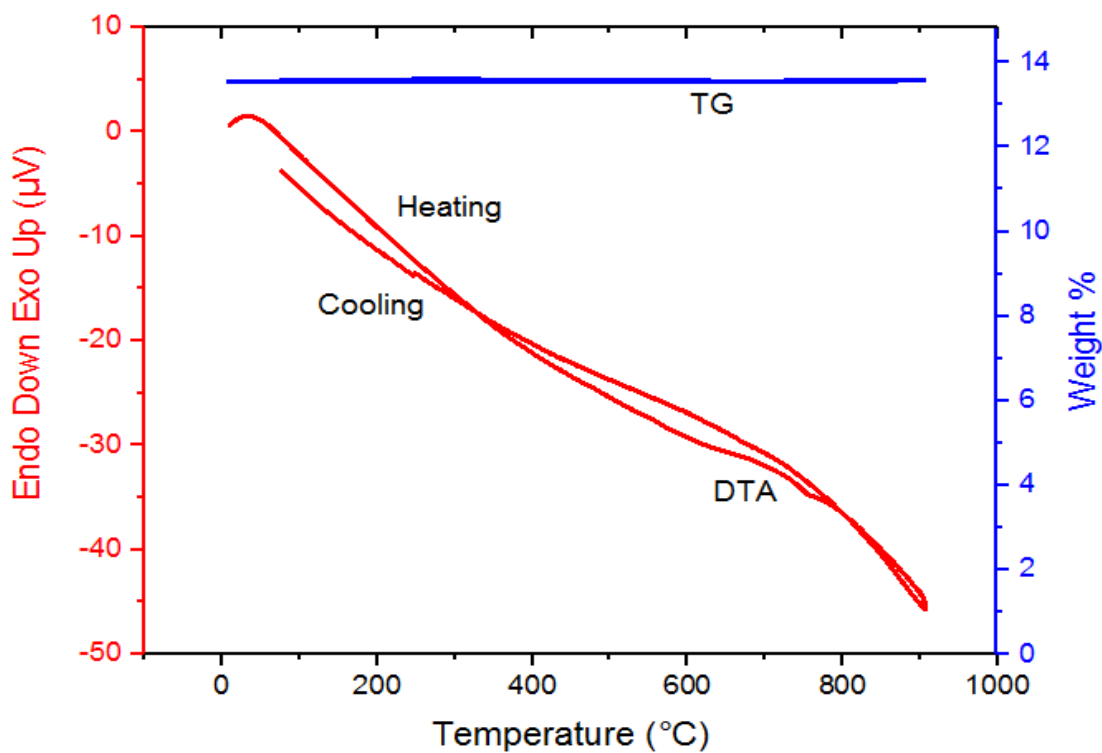


Figure 4.21. DTA/TG spectrum for M8 (Sample Weight: 13.556 mg).

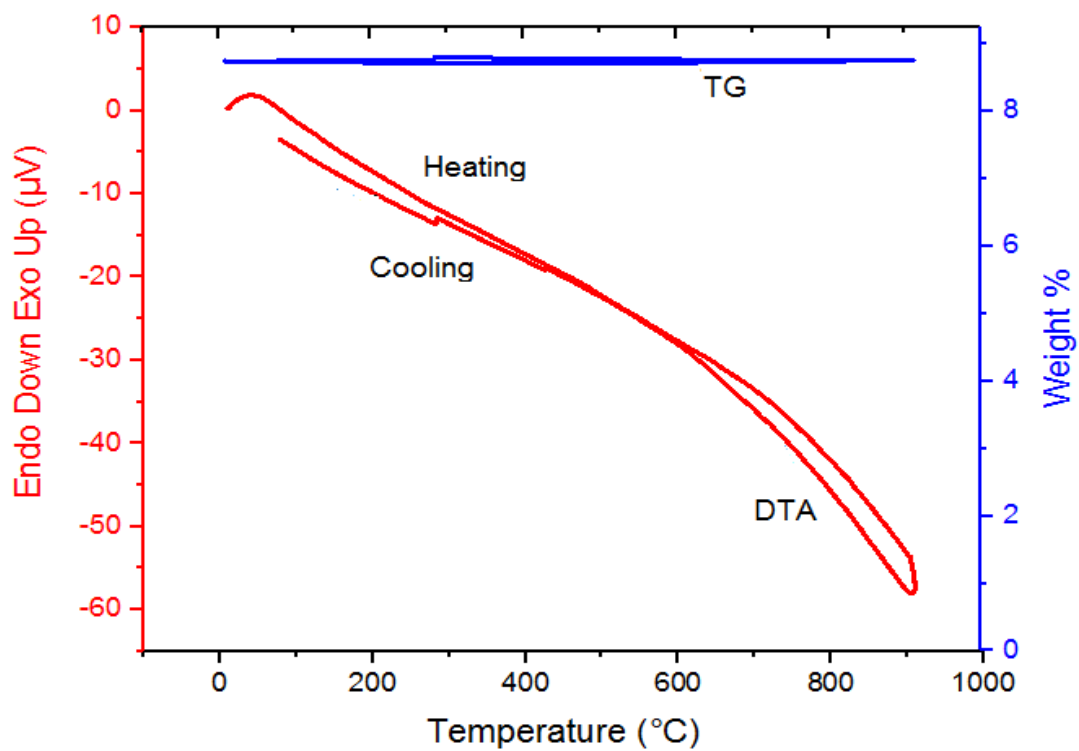


Figure 4.22. DTA/TG spectrum for M9 (Sample Weight: 8.747 mg).

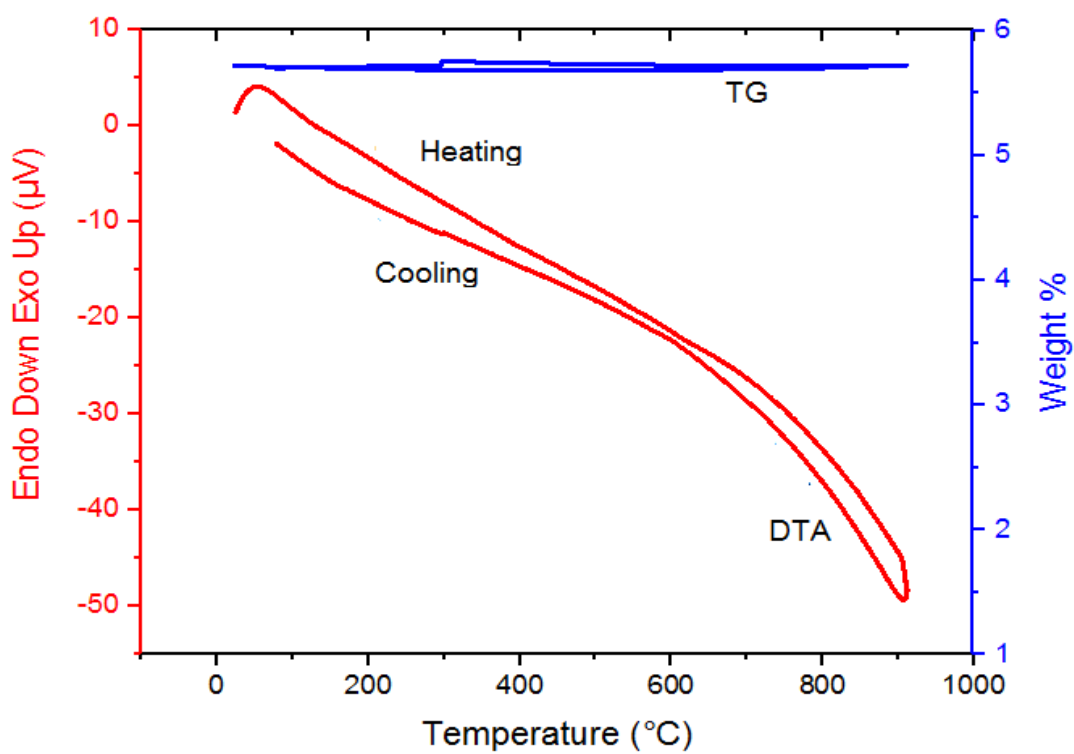
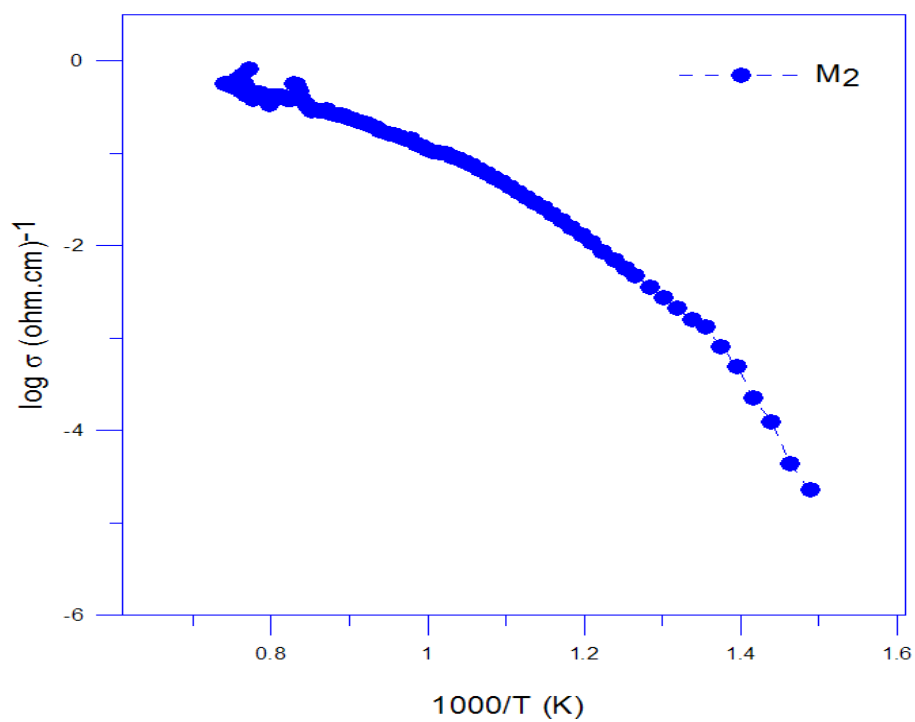
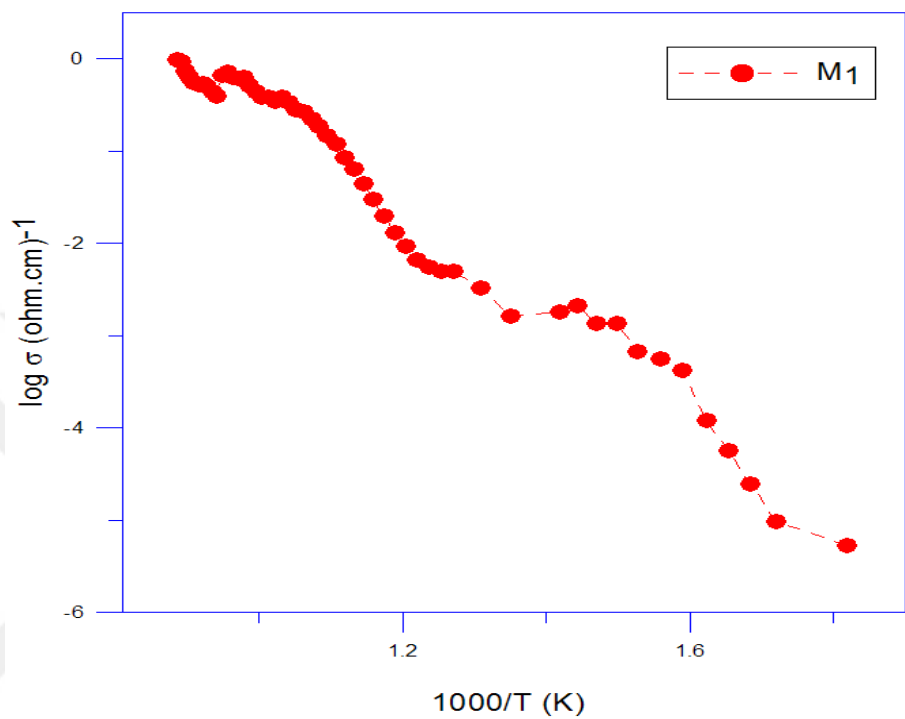
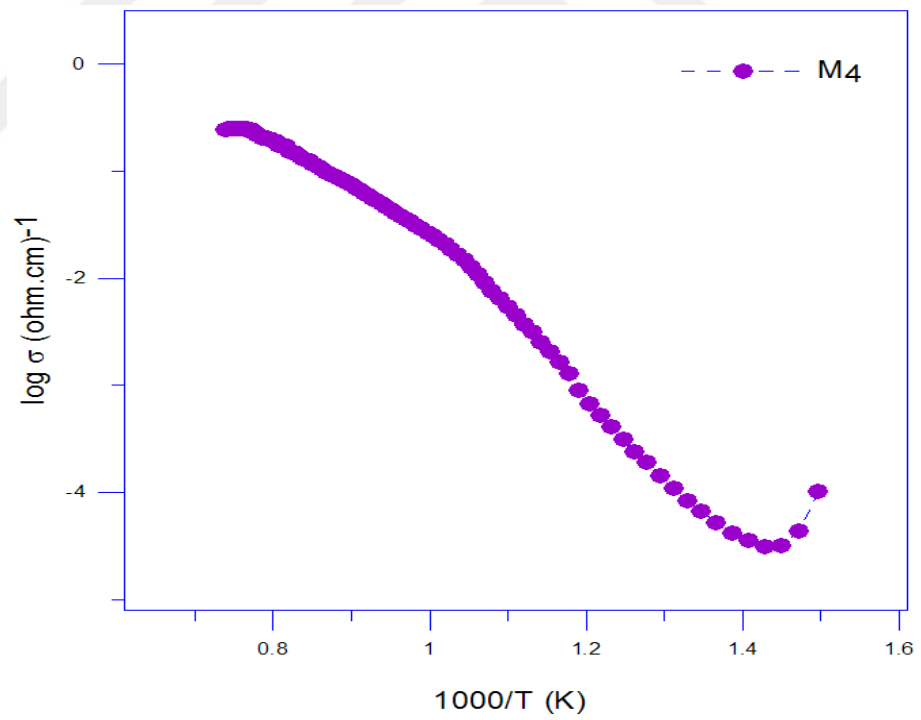
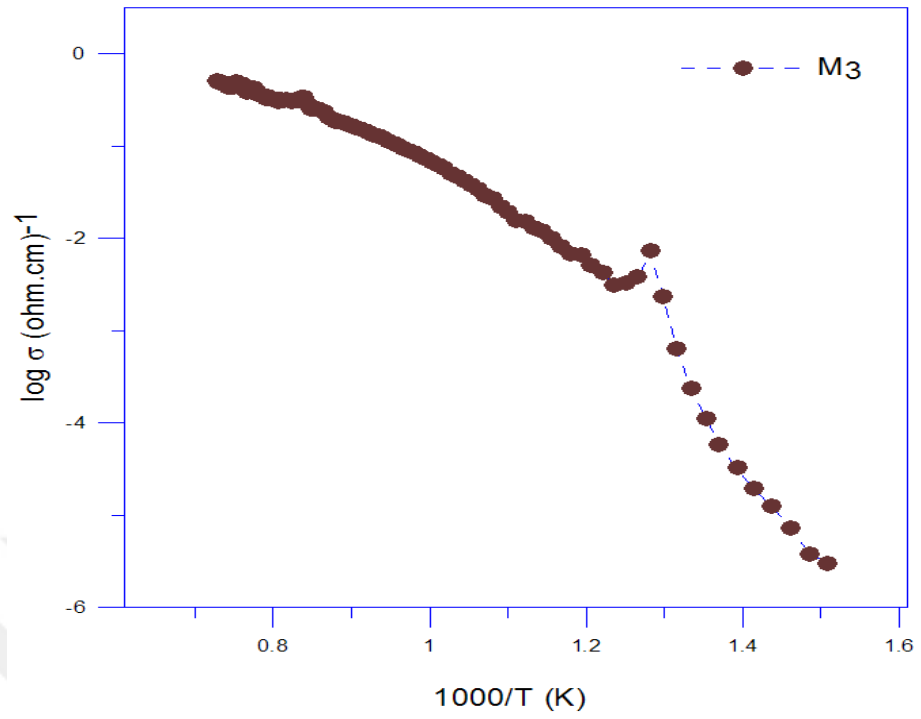


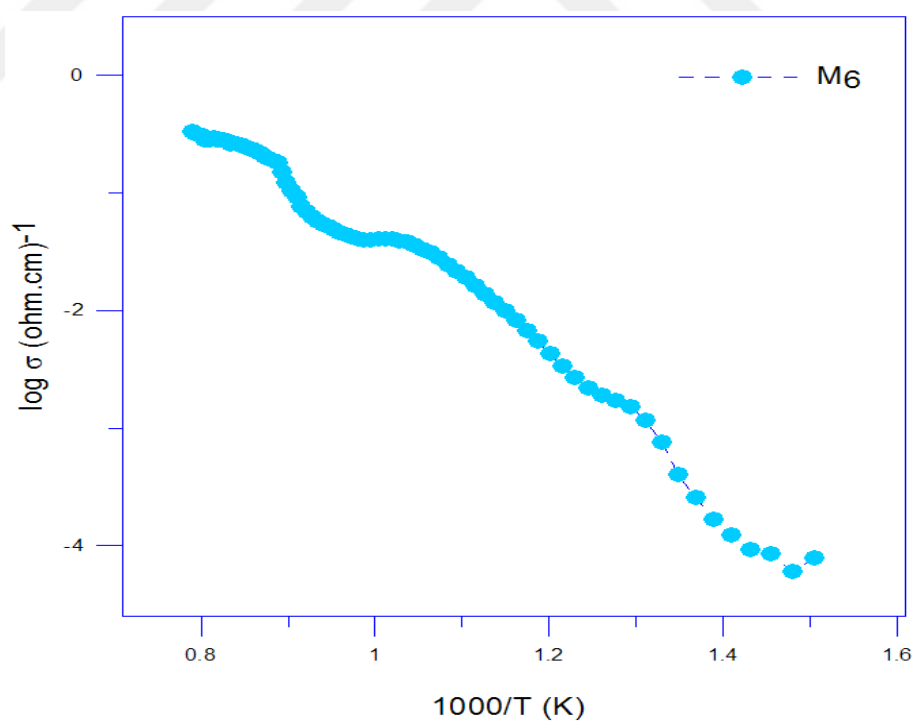
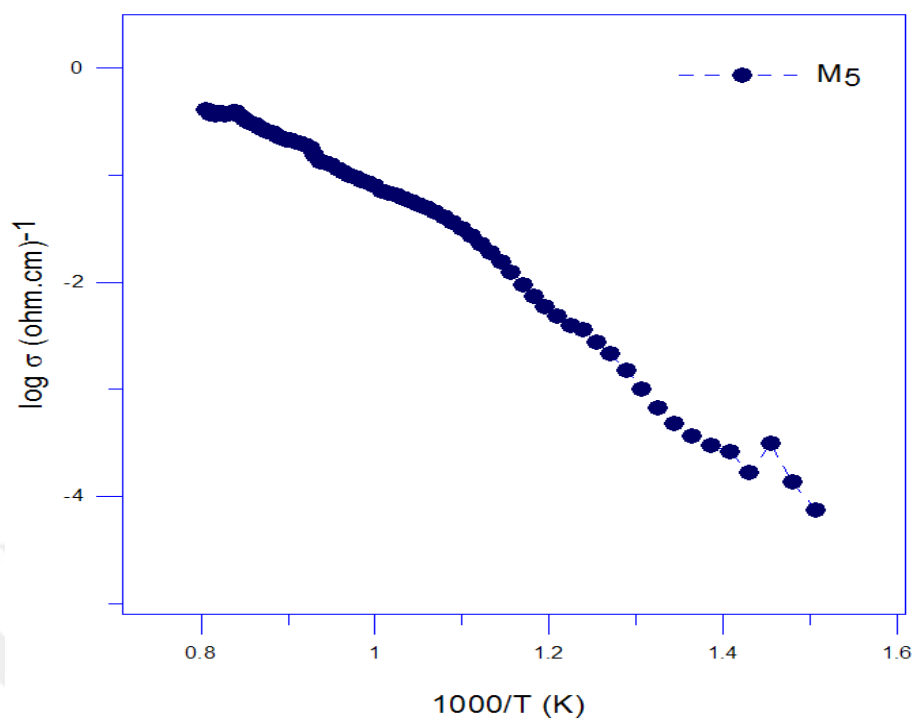
Figure 4.23. DTA/TG spectrum for M10 (Sample Weight: 5.727 mg).

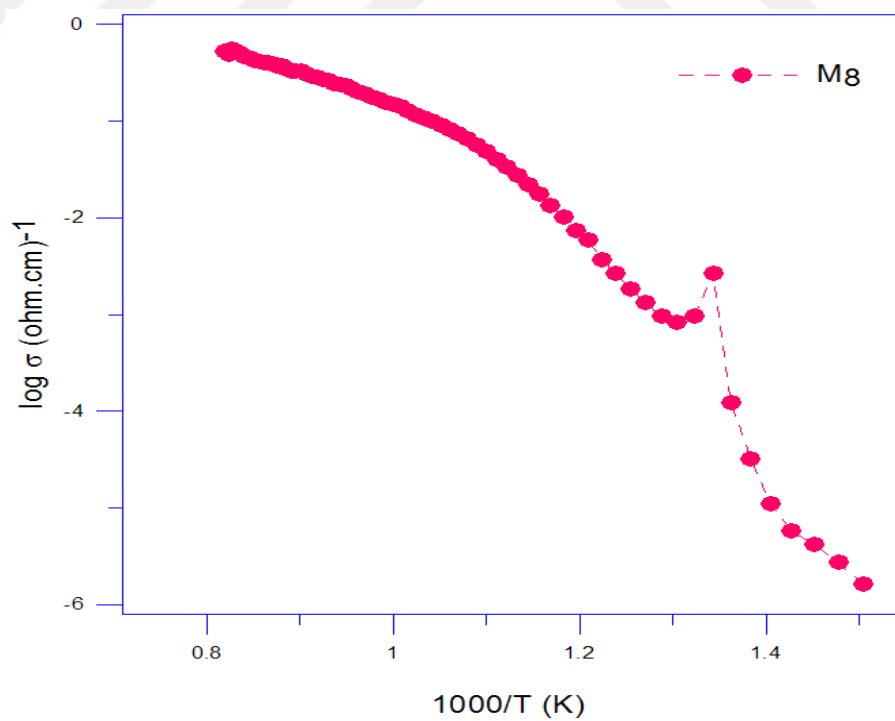
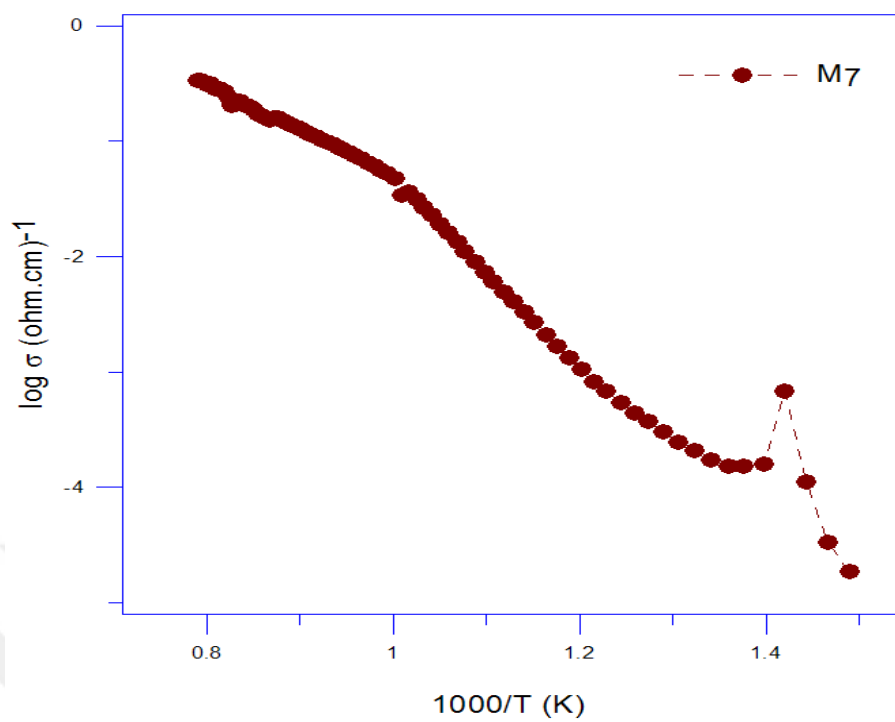
4.1.3. Electrical conductivity

Temperature dependence of conductivity for all sample (M1-M10) over heating cycles are given in Figure 4.24.









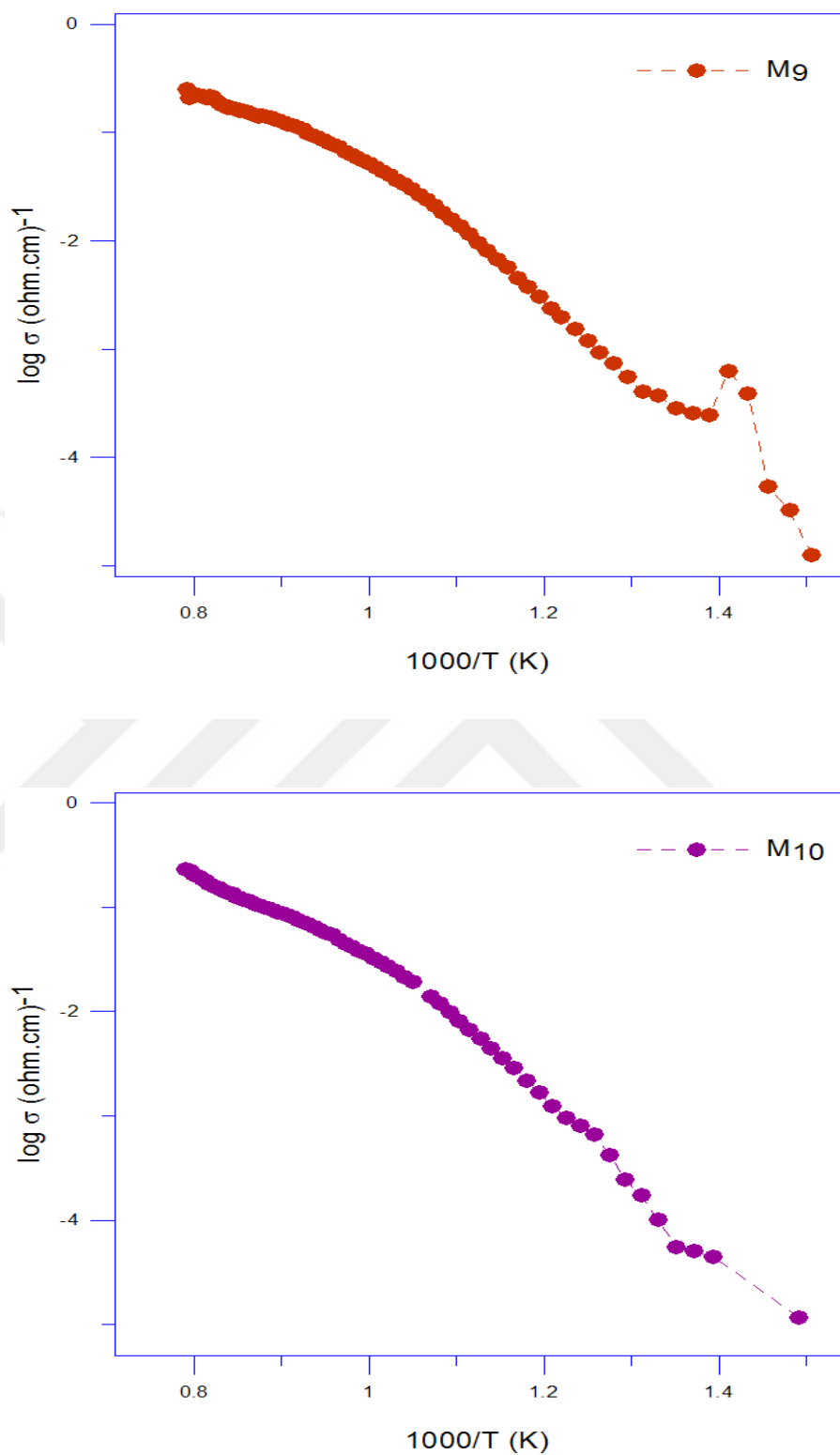


Figure 4.24. Temperature dependence of the electrical conductivity for samples M1-M10 over heating cycles.

Overlap graph of the temperature dependence of the electrical conductivity for samples (M1-M4) over heating cycles is given below (Figure 4.25).

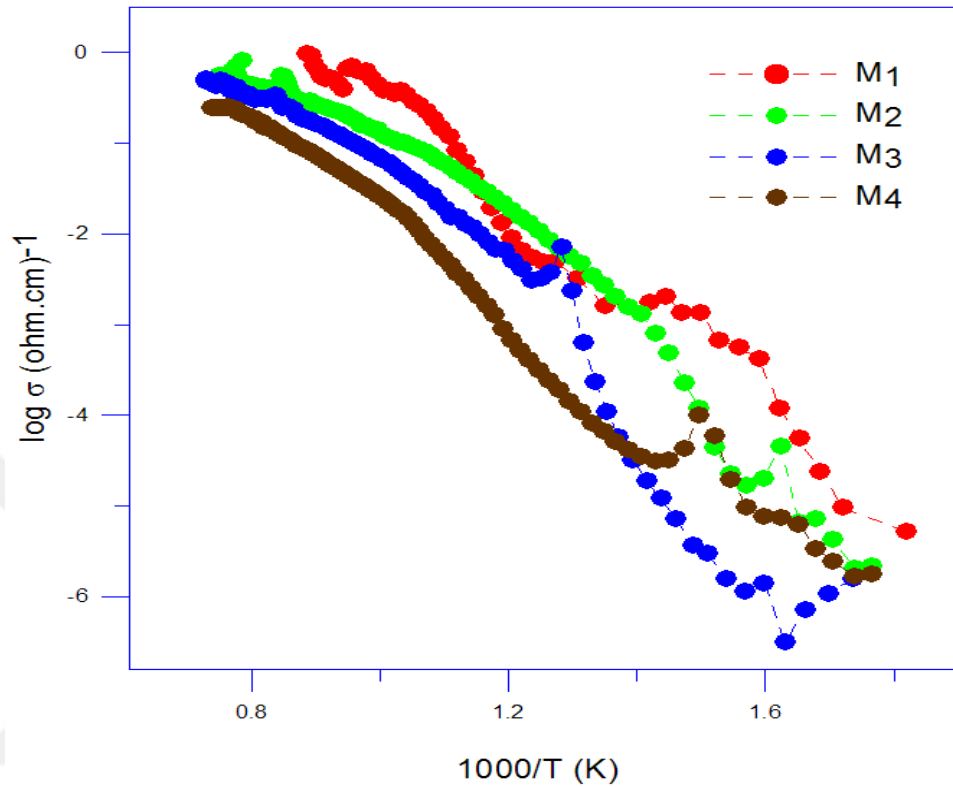


Figure 4.25. Overlapped plot of the temperature dependence of the electrical conductivity for samples (M1-M4) over heating cycles.

The comparison of the electrical conductivity measurement results of samples M1, M2, M3 and M4 shows that electrical conductivity decreases with an increasing amount of Tm_2O_3 at high temperature of above $900^\circ C$ in the $(Bi_2O_3)_{1-x-y-z} (Dy_2O_3)_x (Eu_2O_3)_y (Tm_2O_3)_z$ quaternary system that has been doped with 0.05 Dy_2O_3 and 0.05 Eu_2O_3 at%. At low temperature about $770^\circ C$, electrical conductivity is almost same for M1 and M2 and considerably higher than M3 and M4 those have the same electrical conductivity at this temperature. The electrical conductivity values of sample M1-M4 at about $750^\circ C$ are summarized in Table 4.2.

Table 4.2. Electrical conductivity parameters of samples M1-M4 at about 750°C.

sample	Dy ₂ O ₃	Eu ₂ O ₃	Tm ₂ O ₃	Bi ₂ O ₃	σ ($\Omega\cdot\text{m}$) ⁻¹	Log σ	Temperature °C
M1	5%	5%	5%	85%	6.20E-01	-0.2072961	750±7
M2	5%	5%	10%	80%	1.42E-01	-0.8480262	750±7
M3	5%	5%	15%	75%	8.93E-02	-1.0491506	750±7
M4	5%	5%	20%	70%	3.39E-02	-1.4704179	750±7

Overlap graph of the temperature dependence of the electrical conductivity for samples M1 and M5-7 over heating cycles is given below (Figure 4.26).

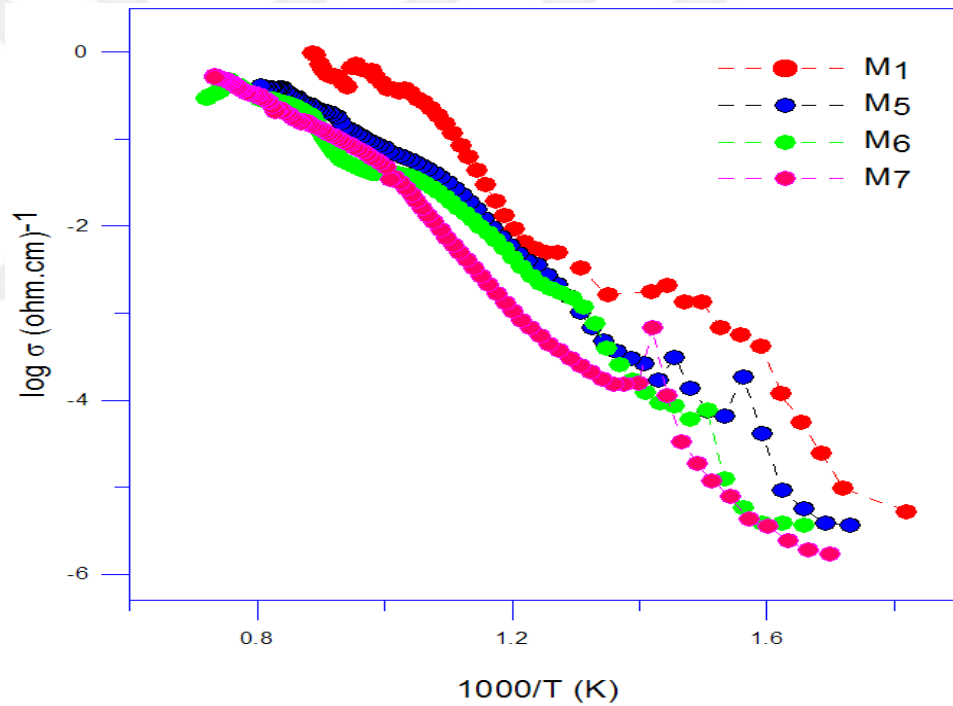


Figure 4.26. Overlapped plot of the temperature dependence of the electrical conductivity for samples M1 and M5-M7 over heating cycles.

The comparison of the electrical conductivity measurement results of samples M1, M5, M6 and M7 shows that electrical conductivity decreases with an increasing amount of Eu₂O₃ for all temperatures scanned in the (Bi₂O₃)_{1-x-y-z} (Dy₂O₃)_x (Eu₂O₃)_y (Tm₂O₃)_z quaternary system that has been doped with 0.05 Dy₂O₃ and 0.05 Tm₂O₃ at%.

The electrical conductivity values of sample M1 and M5-7 at about 750 °C are given in Table 4.3.

Table 4.3. Electrical conductivity parameters of samples M1 and M5-7 at about 750°C.

Sample	Dy ₂ O ₃	Eu ₂ O ₃	Tm ₂ O ₃	Bi ₂ O ₃	σ ($\Omega\cdot\text{m}$) ⁻¹	Log σ	Temperature
M1	5%	5%	5%	85%	6.20E-01	-0.2072961	750±7
M5	5%	10%	5%	80%	9.46E-02	-1.02417836	750±7
M6	5%	15%	5%	75%	4.21E-02	-1.37616541	750±7
M7	5%	20%	5%	70%	6.09E-02	-1.215331422	750±7

Overlap graph of the temperature dependence of the electrical conductivity for samples M1 and M8-M10 over heating cycles is given below (Figure 4.27).

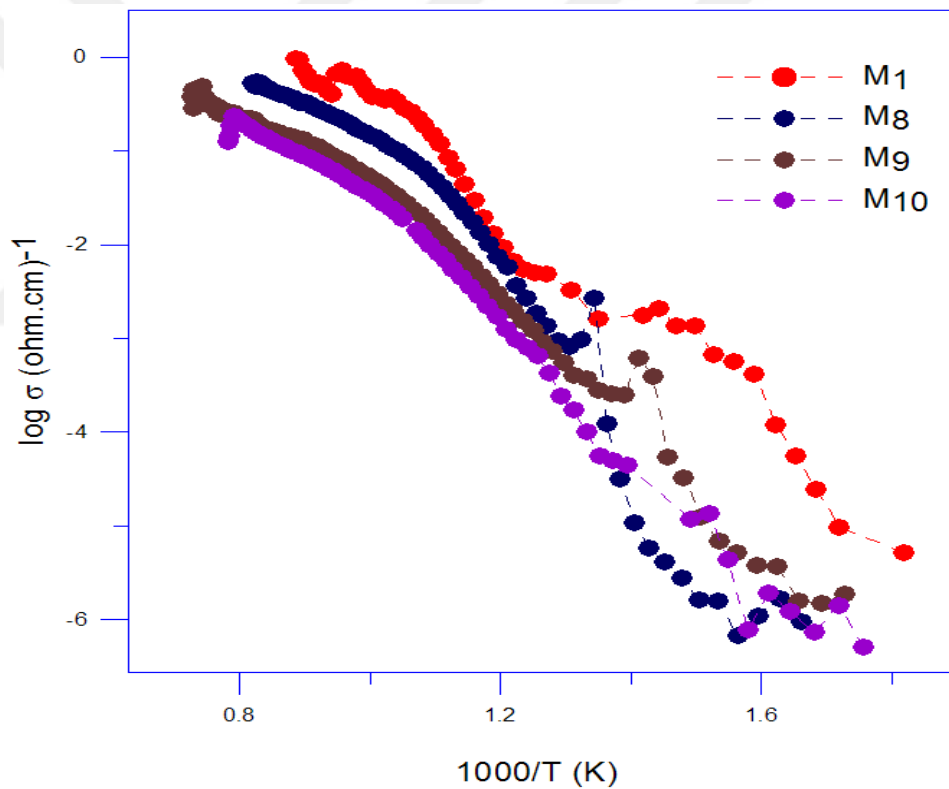


Figure 4.27. Overlapped plot of the temperature dependence of the electrical conductivity for samples M1 and M8-M10 over heating cycles.

The comparison of the electrical conductivity measurement results of samples M1, M8, M9 and M10 shows that electrical conductivity decreases with an increasing amount of Dy₂O₃ at temperature of above 750 °C in the (Bi₂O₃)_{1-x-y-z} (Dy₂O₃)_x (Eu₂O₃)_y (Tm₂O₃)_z quaternary system that has been doped with y=0.05 Eu₂O₃ and z=0.05 Tm₂O₃ at%.

However, the highest electrical conductivity was detected on sample M8 at about 750 °C. The electrical conductivity values of sample M1 and M8-M10 at about 750°C are given in Table 4.4.

Table 4.4. Electrical conductivity parameters of samples M1 and M8-10 at about 750°C.

sample	Dy ₂ O ₃	Eu ₂ O ₃	Tm ₂ O ₃	Bi ₂ O ₃	σ ($\Omega\cdot\text{m}$) ⁻¹	Log σ	Temperature
M1	5%	5%	5%	85%	6.20E-01	-0.2072961	750±6
M8	10%	5%	5%	80%	1.75E-01	-0.75679521	750±6
M9	15%	5%	5%	75%	6.62E-02	-1.17918826	750±6
M10	20%	5%	5%	70%	4.52E-02	-1.34470172	750±6

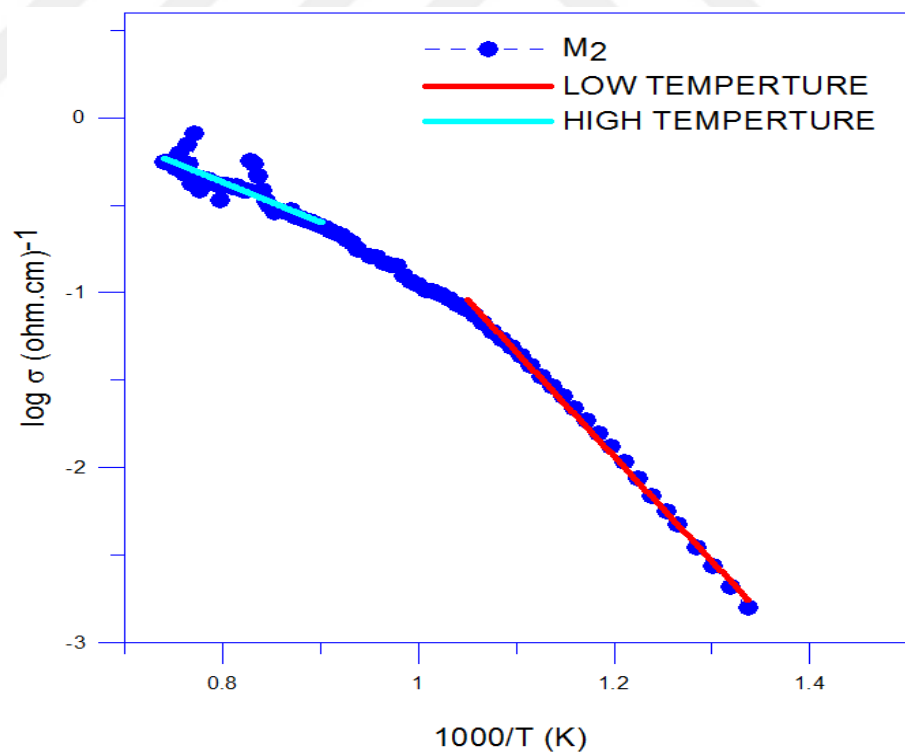
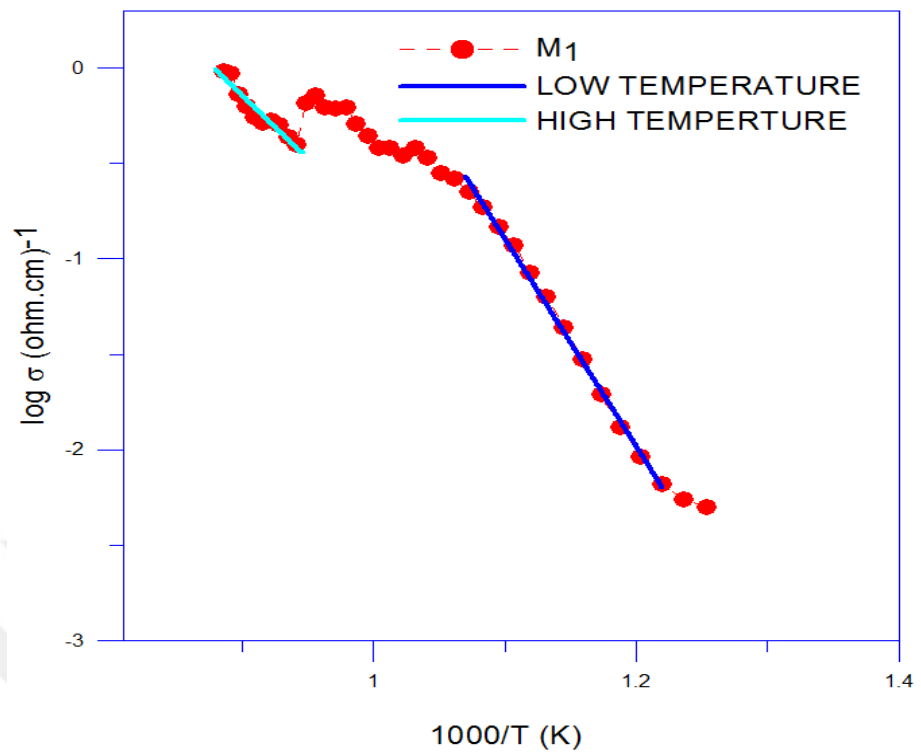
4.1.4. Calculation of Activation Energies

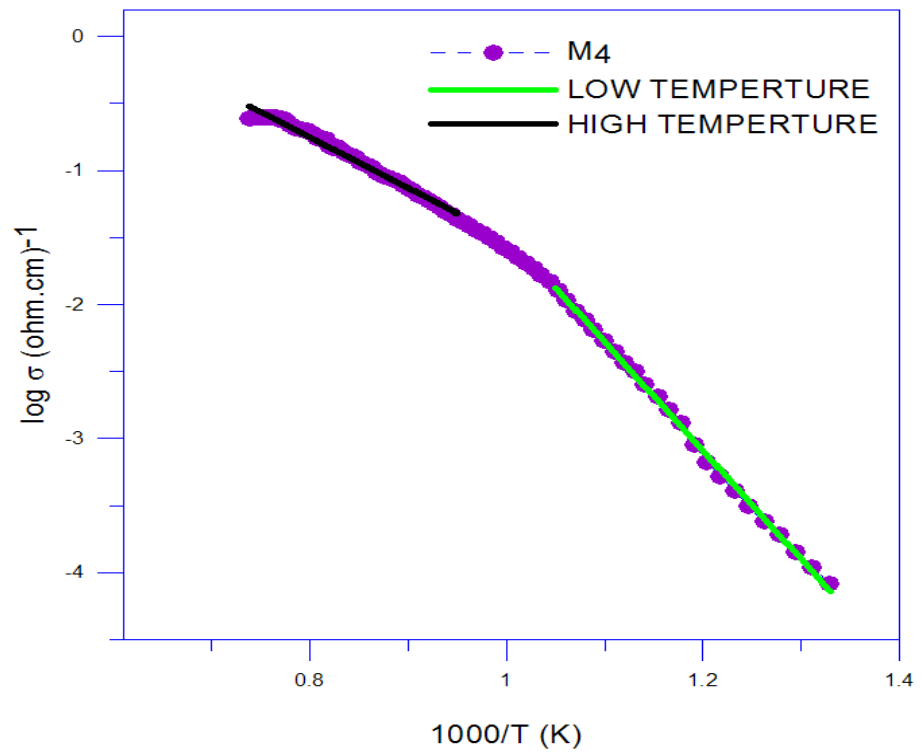
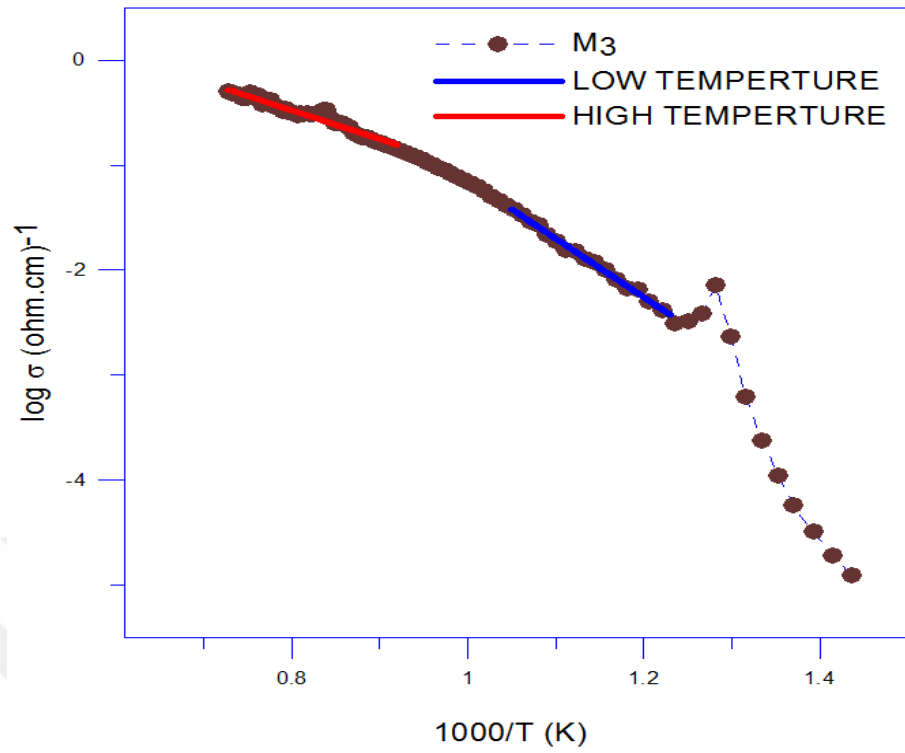
The activation energy is the threshold energies that ions need to move from one position to another vacant position. Electrical conductivity activation energies – slopes of Arrhenius plots were obtained by plotting the following equation:

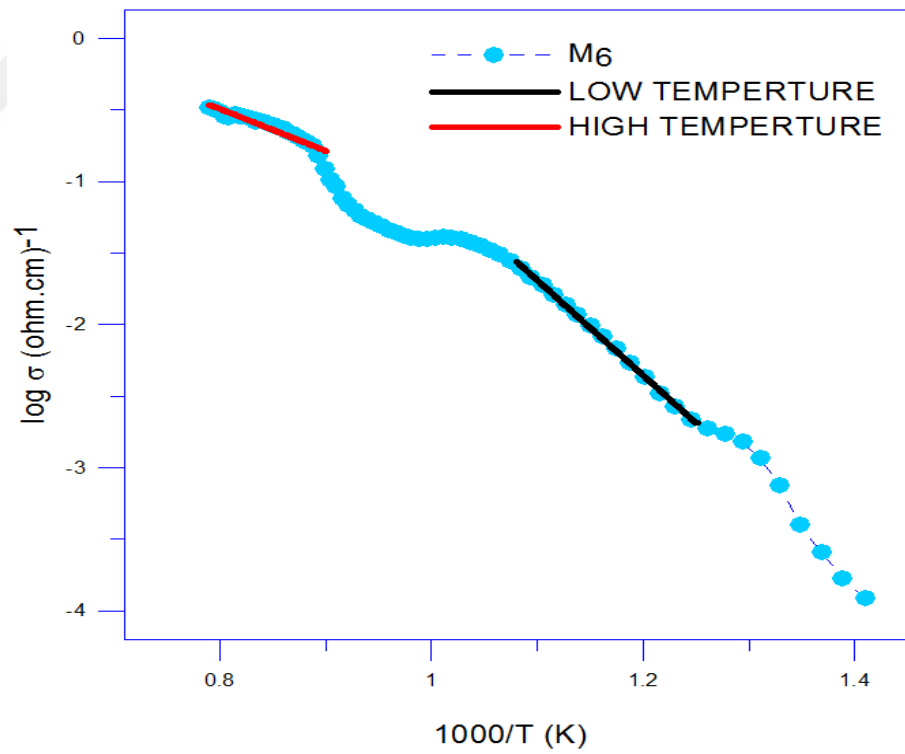
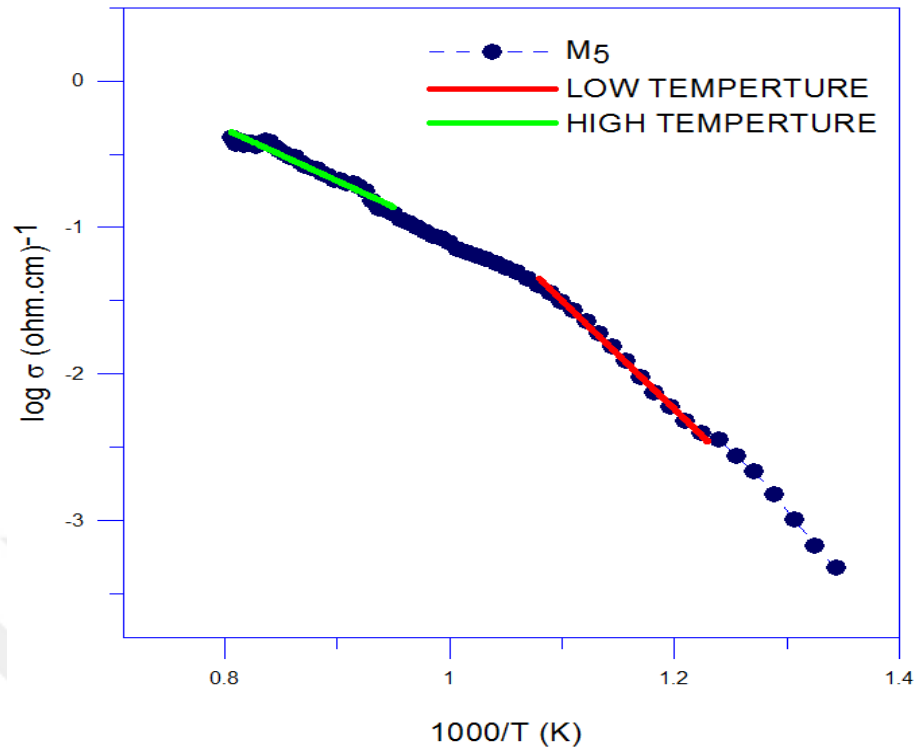
$$\ln(\sigma) = -\left(\frac{E_a}{R}\right) \cdot \frac{1}{T} + \ln \sigma_0$$

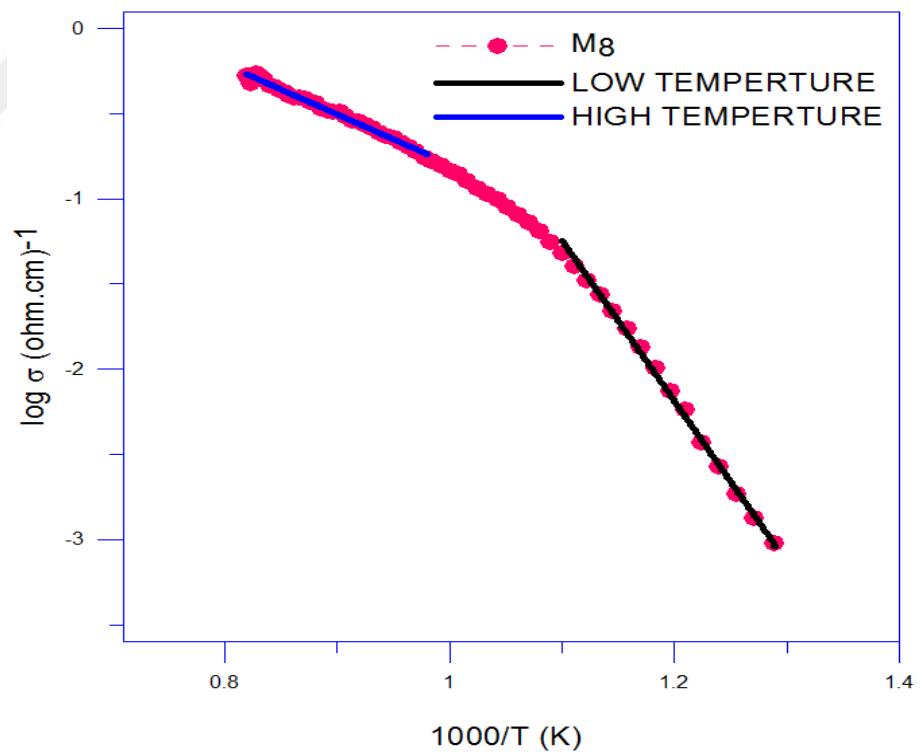
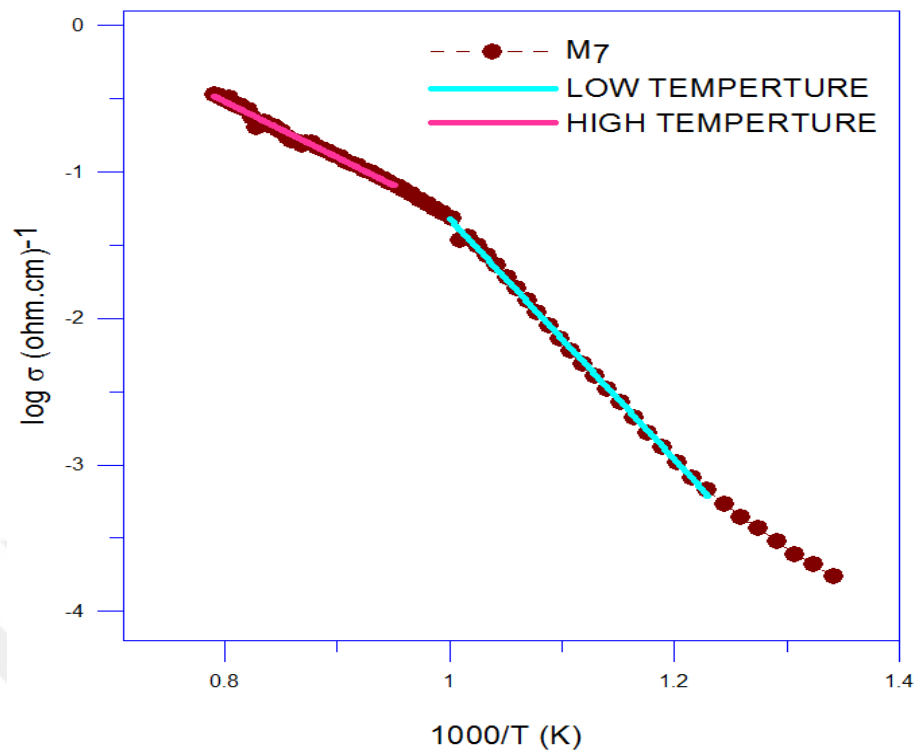
Where σ is the conductivity and σ_0 is the pre-conductivity value in units of kelven. R is the ideal gas constant ($R=8.63 \times 10^{-5}$ eV. K⁻¹.atom⁻¹) and E_a represent the activation energy in the conductivity equation. The slope of the curve is equal to $-E_a/R$.

The Arrhenius plots of electrical conductivity at low and high temperature for sample M1-M10 are given in Figure 4.28. Activation energies calculated for each sample at low and high temperature are listed in Table 4.5 and Table 4.6 respectively









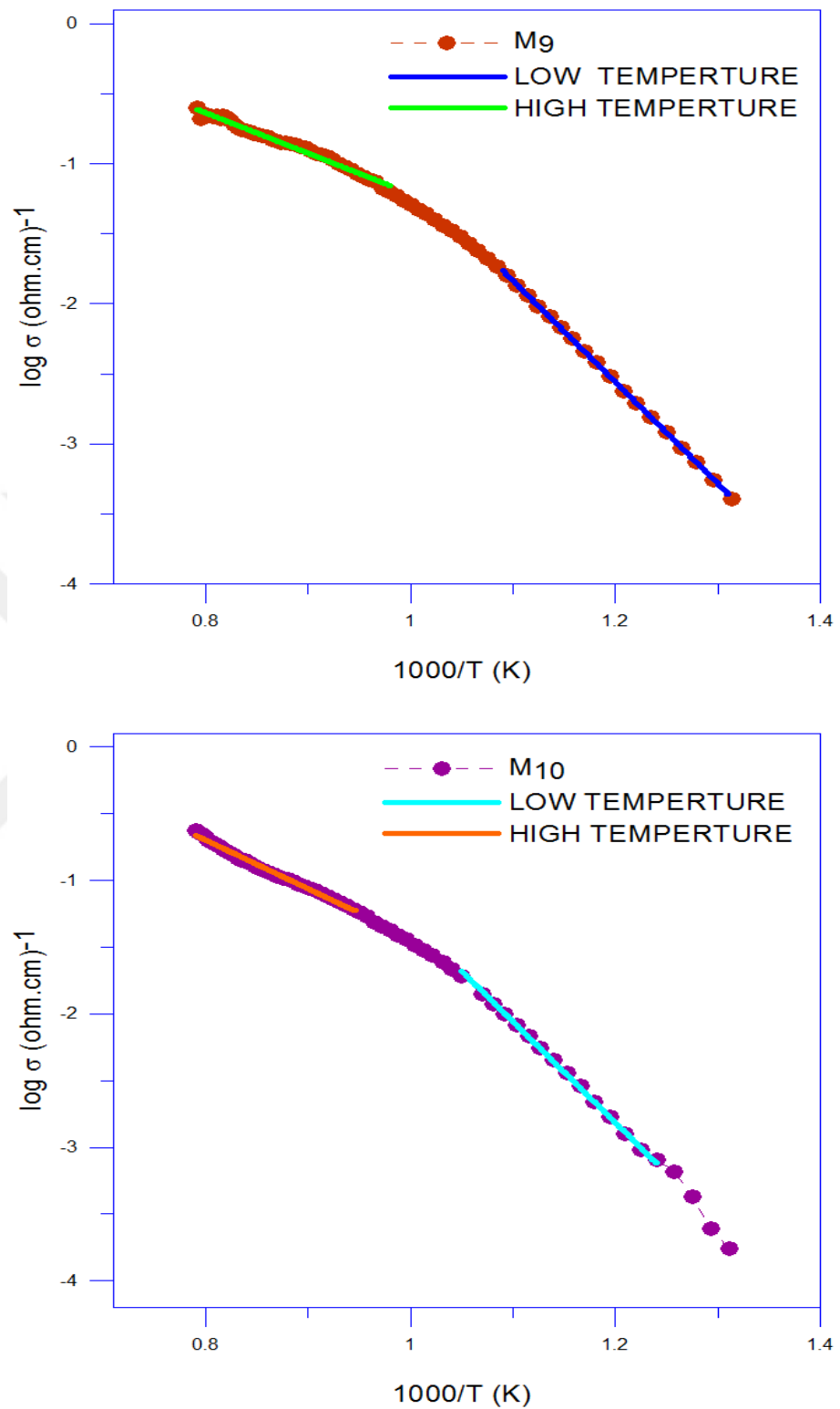


Figure 4.28. The Arrhenius plots of electrical conductivity at low and high temperature for sample M1-M10.

Table 4.5. Activation energies calculated for each sample at low temperatures.

Sample	Bi ₂ O ₃	Tm ₂ O ₃	Eu ₂ O ₃	Dy ₂ O ₃	σ_1	T ₁ (K)	σ_2	T ₂ (K)	E _a (eV)
M1	85%	5%	5%	5%	1,62E-03	741	3,81E-01	996	1,363
M2	80%	10%	5%	5%	1,31E-03	738	2,91E-02	880	1,223
M3	75%	15%	5%	5%	3.30E-03	800	1.52E-02	892	1.023
M4	70%	20%	5%	5%	6,64E-05	742	1,67E-02	966	1,526
M5	80%	5%	10%	5%	2.75E-03	797	4,51E-02	936	1,295
M6	75%	5%	15%	5%	1.73E-03	783	1,91E-02	906	1.195
M7	70%	5%	20%	5%	5.47E-04	804	3,63E-02	984	1.591
M8	80%	5%	5%	10%	9,72E-04	755	5,61E-02	918	1,488
M9	75%	5%	5%	15%	2,83E-04	740	1,59E-02	914	1,351
M10	70%	5%	5%	20%	6.62E-04	795	1,41E-02	934	1.410

Table 4.6. Activation energies calculated for each sample at high temperatures.

Sample	Bi ₂ O ₃	Tm ₂ O ₃	Eu ₂ O ₃	Dy ₂ O ₃	σ_1	T ₁ (K)	σ_2	T ₂ (K)	E _a (eV)
M1	85%	5%	5%	5%	4,40E-01	1005	9,65E-01	1136	0,5906
M2	80%	10%	5%	5%	1,44E-01	1030	5,60E-01	1351	0,5080
M3	75%	15%	5%	5%	1,13E-01	1056	5,07E-01	1374	0,5910
M4	70%	20%	5%	5%	5,61E-02	1080	2,46E-01	1356	0,6768
M5	80%	5%	10%	5%	1,14E-01	1045	4,12E-01	1241	0,7336
M6	75%	5%	15%	5%	4,21E-02	1027	2,95E-01	1389	0,6621
M7	70%	5%	20%	5%	7,05E-02	1035	5,04E-01	1366	0,7250
M8	80%	5%	5%	10%	1,28E-01	985	5,32E-01	1220	0,6286
M9	75%	5%	5%	15%	6,62E-02	1021	3,80E-01	1377	0,5955
M10	70%	5%	5%	20%	5,41E-02	1044	1,25E-01	1280	0,4092

Activation energy is being changed at between 1.023 eV for sample M3 and 1.591 eV for sample M7 at low temperature region. However, at high temperature region, activation energy is being changed at between 0.41 eV for sample M10 and 0.73 eV for sample M5 or M7. In comparison, Low temperature activation energies are nearly one third of high temperature activation energies. It can be concluded from the calculated activation energies that electrical conductivity increases with rising temperature in all samples, because of an increase in both the number of charge carriers (electron and mostly O⁻² ions in Bi₂O₃ –based electrolytes) and mobility of charge carriers with temperature.

Discontinuity in the activation energy indicates the phase transition or change in the kind of charge carriers. Discontinuity observed at about 750°C correspond to the transition from α -Bi₂O₃ phase to δ -Bi₂O₃ phase, but the discontinuity observed between the low and high temperature curve probably due to the change in the kind of charge carriers to be completely ionic.

4.2. Conclusion

The as-annealed (at 750°C for 100 hours) (Bi₂O₃)_{1-x-y-z} (Dy₂O₃)_x (Eu₂O₃)_y (Tm₂O₃)_z quaternary system, samples consist of mainly cubic fcc δ -Bi₂O₃ phase with Bi₂O₃ together small amount of monoclinic α -Bi₂O₃ phase as detected from XRD analysis. After electrical conductivity measurement, the X-ray diffraction patterns clearly indicated that all samples almost consist of single δ -Bi₂O₃ phase. Which means that a phase transition from monoclinic α -Bi₂O₃ to cubic δ -Bi₂O₃ has been taken place during heating cycle used for conductivity measurement. This phase transition clearly detected from DTA spectrums and conductivity measurement curves at about 750°C for some samples. DTA spectrum also reveals that cubic δ -Bi₂O₃ is stable during cooling between 900°C and room temperature. This indicates that doping makes cubic δ -Bi₂O₃ phase stable.

The highest electrical conductivity measured at 750°C is $6.21 \times 10^{-1} (\Omega \cdot \text{cm})^{-1}$. It was observed for composition of (Bi₂O₃)_{0.85} (Dy₂O₃)_{0.05} (Eu₂O₃)_{0.05} (Tm₂O₃)_{0.05}. The lowest electrical conductivity of about $3.39 \times 10^{-2} (\Omega \cdot \text{cm})^{-1}$ was observed for composition of (Bi₂O₃)_{0.70} (Dy₂O₃)_{0.05} (Eu₂O₃)_{0.05} (Tm₂O₃)_{0.20} and (Bi₂O₃)_{0.75} (Dy₂O₃)_{0.05} (Eu₂O₃)_{0.15} (Tm₂O₃)_{0.05} ($4.21 \Omega^{-1} \cdot \text{cm}^{-1}$) at 750°C. It is clear that electrical conductivity decreases nearly one order of magnitude with increasing concentration of doped materials. The reason of this lower conductivity can be attributed to the presence of secondary or impurity phases which are located along the grain boundaries and reduce the ionic conductivity. An increased dopant concentration increases the secondary phases and impurities.

The electrical conductivity of $0.62 (\Omega \cdot \text{cm})^{-1}$ measured for low dopant concentration at 750°C is comparable with conductivity of pure δ -Bi₂O₃ ($\sim 1 \Omega^{-1} \cdot \text{cm}^{-1}$ at 650°C).

CHAPTER 5

CONCLUSION AND FUTURE WORKS

The results obtained in this study can be summarized as follows:

- Bismuth oxide (Bi_2O_3) based $(\text{Bi}_2\text{O}_3)_{1-x-y-z} (\text{Dy}_2\text{O}_3)_x (\text{Eu}_2\text{O}_3)_y (\text{Tm}_2\text{O}_3)_z$ quaternary system has been synthesized. The crystallographic thermal and electrical conductivity properties were characterized.
- In this quaternary system, face-centered cubic (fcc) $\delta\text{-Bi}_2\text{O}_3$ phase solid solution predominantly produced (after heat treatment).
- The solids synthesized were found to have oxygen ionic conductivity.
- With the increase of the Tm_2O_3 dopant concentration, while dopant concentration of 5% mole Dy_2O_3 and 5% mole Eu_2O_3 was constant, there was no change in the phase structures and it was observed that the phase structures were (cubic) $\delta\text{-}(\text{Bi}_2\text{O}_3)$ phase.
- With the increase of the Eu_2O_3 dopant concentration, while dopant concentration of 5% mole Dy_2O_3 and 5% mole Tm_2O_3 was constant, there was no change in the phase structures and it was observed that the phase structures were (cubic) $\delta\text{-}(\text{Bi}_2\text{O}_3)$ phase.
- With the increase of the Dy_2O_3 dopant concentration, while dopant concentration of 5% mole Tm_2O_3 and 5% mole Eu_2O_3 was constant, there was no change in the phase structures and it was observed that the phase structures were (cubic) $\delta\text{-}(\text{Bi}_2\text{O}_3)$ phase.
- DTA spectrum also reveals that cubic $\delta\text{-Bi}_2\text{O}_3$ was stable on cooling between 900 °C to room temperature. This indicates that doping makes cubic $\delta\text{-Bi}_2\text{O}_3$ phase stable.

- The highest conductivity measured at 750 °C was observed for composition $(\text{Bi}_2\text{O}_3)_{0.85} (\text{Dy}_2\text{O}_3)_{0.05} (\text{Eu}_2\text{O}_3)_{0.05} (\text{Tm}_2\text{O}_3)_{0.05}$ is $6.21 \times 10^{-1} (\Omega \cdot \text{cm})^{-1}$.
- Electrical conductivity decreases nearly one order of magnitude with increasing concentration of doped materials.
- An increased dopant concentration increases the secondary phases and impurities. The presence of secondary or impurity phases which are located along the grain boundaries reduce the ionic conductivity.
- The electrical conductivity of $0.62 (\Omega \cdot \text{cm})^{-1}$ measured for low dopant concentration at 750 °C is comparable with conductivity of pure $\delta\text{-Bi}_2\text{O}_3$ ($\sim 1 \Omega^{-1} \cdot \text{cm}^{-1}$ at 650°C),
- The resulting solid electrolytes in the $(\text{Bi}_2\text{O}_3)_{1-x-y-z} (\text{Dy}_2\text{O}_3)_x (\text{Eu}_2\text{O}_3)_y (\text{Tm}_2\text{O}_3)_z$ quaternary system have been found to be an alternative to known solid electrolytes, which can be used in industrial applications (SOFC), such as other known solid electrolytes.
- Unlike other solid electrolytes are known in the literature, in this study, the conductivity and the working efficiency were increased.

Future Work

- The mechanical properties and thermal expansion coefficient of these quaternary system can be investigated
- It can be improved by doping different cations without degrading the ionic conductivity.
- Also, the solid solution limit can be investigated by increasing the value of x, y, z in the $(\text{Bi}_2\text{O}_3)_{1-x-y-z} (\text{Dy}_2\text{O}_3)_x (\text{Eu}_2\text{O}_3)_y (\text{Tm}_2\text{O}_3)_z$ quaternary system or by taking small interval value of x, y, z (nearly ≤ 0.025).

REFERENCE

1. <http://www.fuelcelltoday.com/history> (Eriřim: Eylöl 2017)
2. <http://www.doitpoms.ac.uk/tlplib/fuel-cells/history.php> (Eriřim: Eylöl 2017)
3. <http://www.horizonfuelcell.com> (Eriřim: Eylöl 2017)
4. <http://www.clearcellpower.com> (Eriřim: Eylöl 2017)
5. <http://www.fuelcellenergy.com> (Eriřim Tarihi: Eylöl 2017)
6. <http://www.doosanfuelcellamerica.com> (Eriřim Tarihi: Eylöl 2017)
7. <http://fuelcell.com> (Eriřim Tarihi: Eylöl 2017)
8. Akbulut, B., 2007.Yakıt Pili Hibrit Santralleri. Fırat Üniversitesi Fen Bilimleri Enstitüsü, Yüksek Lisans Tezi, 111s, Elazığ. 117
9. Larminie, J., and Dicks, A., 2003. Fuel Cell Systems Explained Second Edition. Oxford Brookes University, John Wiley & Sons, 978-1-59124-807- 1,418, İngiltere
10. Çetinkaya M. ve Karaosmanoglu, F., 2005. Yakıt Pilleri, Makina Mühendisleri Odası Bülteni. 98s. Ankara
11. Hidrojen Enerjisi Forumu, 2005, “Hidrojen Enerjisi”, http://sifirforum.net/forum/siyaset/hidrojen_enerjisit6557.0.html, (Eriřim Tarihi: 18 Haziran 2007)
12. Forsberg, C. W. (2007). Future hydrogen markets for large-scale hydrogen production systems. **International Journal of Hydrogen Energy**, **32**(4), 431-439.
13. Renault, S., Gottis, S., Barrès, A. L., Courty, M., Chauvet, O., Dolhem, F., & Poizot, P. (2013). A green Li–organic battery working as a fuel cell in case of emergency. **Energy & Environmental Science**, **6**(7), 2124-2133.
14. Aydın, M., 2007. PEM Yakıt Pilinin İki Boyutlu Modellemesi.İstanbul Teknik Üniversitesi Enerji Enstitüsü, Yüksek Lisans Tezi, 82s, İstanbul.
15. Yıldızbilir, F., 2006. Yakıt Pili ile Elektrik Enerjisi Üretimi. Fırat Üniversitesi Fen Bilimleri Enstitüsü, Yüksek Lisans Tezi, 46s, Elazığ

16. Fergus, J. W. (2006). Electrolytes for solid oxide fuel cells. **Journal of Power Sources**, **162**(1), 30–40.
17. Bozoklu, M., Turkoglu, O., Yılmaz, S., Arı, M., & Belenli, I. (2010). Oxide ionic conductivity and crystallographic properties of tetragonal type Bi₂O₃-based solid electrolyte doped with Ho₂O₃. **Materials Science and Technology**, **26**(10), 1239-1247.
18. Wolfstieg, U., & Macherauch, E. (1976). New Text Document. Hiirterei-TechMitt. **<https://doi.org/10.1093/rheumatology/39.3.245>**
19. Preparative methods in Solid State Chemistry", B. Gerard, G. Nowogrocki, J. Guenot, M. Figlarz, Academic press
20. "Solid State Chemistry and its Applications", Anthony R. West, Wiley, and Sons, 2005
21. **http://acta.chemscand.org/pdf/acta_vol_24_p0384-0396** (Erişim: Ekim 2017).
22. Wachsman E. D., Lee K. T., (2011). "Lowering the Temperature of Solid Oxide Fuel Cells", **Science**, 334: 935-939.
23. Zhong G. H., Wang J. L., Zeng Z., (2006). "Ionic Transport Properties in Doped δ -Bi₂O₃", **Journal of Physics: Conference Series**, **29**: 106–109.
24. Harwig, H. A., "On the structure of Bismuthsesquioxide: the α , β , γ and δ -phase", **Zeitschrift für Anorganische und Allgemeine Chemie**, **444**: 151-166, (1978).
25. Yılmaz S., (2008). "Dy₂O₃, Eu₂O₃, Sm₂O₃ Katkılanmış β -Bi₂O₃ Tipi Katı Elektrolitlerin Sentezlenmesi, Karakterizasyonları Ve Katı Hal Oksijen İyonik İletkenliklerinin Araştırılması", Gazi Üniversitesi Fen Bilimleri Enstitüsü, Doktora Tezi, 187 s..
26. Oniyama, E., Wahlbeck, P. G., (1998). "Phase equilibria in the Bismuth-Oxygen system", **Journal of Physical Chemistry**, **102**: 4418-4425.
27. Sammes N. M., Tompsett G. A., Nafe H., Aldinger F., (1999). " Bismuth Based Oxide Electrolytes – Structure and Ionic Conductivity", **Journal of the European ceramic Society**, **19**: 1801-1826.

28. Yashima, M., Ishimura, D., “Crystal structure and disorder of the fast oxide-ion conductor cubic Bi_2O_3 ”, **Chemical Physics Letter**, **378**: 395-399 (2003).
29. Yaremchenko, A. A., Kharton, V. V., Naumovich, E. N., Tonoyan, A.A., (2000). “Stability of $\delta\text{-Bi}_2\text{O}_3$ -based solid electrolytes”, **Material Research Bulletin**, **35**: 515-520.
30. Boyapati, S., Wachsman, E.D., Chakoumakos, B.C., (2001). “Neutron Diffraction Study of Occupancy, Positional Order of Oxygen Ions in Phase Stabilized Cubic Bismuth Oxide”, **Solid State Ionics**, **138**: 293-304.
31. Miyayama, M., Yanagida, H., (1986). “Oxygen Ion Conduction in $\gamma\text{-Bi}_2\text{O}_3$ Doped with Sb_2O_3 ”, **Journal of Materials Science**, **21**: 1233-1236.
32. Jiang N., Wachsman E. D., Jung S. H., (2002). “A Higher Conductivity Bi_2O_3 -based Electrolyte” **Solid State Ionics**, **150**: 347-353.
33. Azad A.M., Larose S., Akbar S.A., (1994). “Review Bismuth Oxide-Based Solid Electrolyte for Fuel Cells”, **Journal of Materials Science**, **29**: 4135-4151.
34. Ralph J.M., Scholar A.C., Krum pelt M., (2001). “Materials for Lower Temperature Solid Oxide Fuel Cells”, **Journal of Materials Science**, **36**: 1161-1172.
35. Nakayama S., (2002). “Electrical properties of $(\text{Bi}_2\text{O}_3)_{0.75}(\text{RE}_2\text{O}_3)_{0.25}$ ceramics (RE= Dy, Y, Ho, Er and Yb)”, **Ceramcis International**, **28**: 907-910.
36. Van Loon, J. C., Galbraith, J. H., & Aarden, H. M. (1971). The determination of yttrium, europium, terbium, dysprosium, holmium, erbium, thulium, ytterbium and lutetium in minerals by atomic-absorption spectrophotometry. **Analyst**, **96** (1138), 47-50.
37. Çelen Ç. (2016). Katı Oksit Yakıt Hücrelerinde Kullanılmak Üzere Yeni Ti p Üçlü Bileşiklerin Üretilmesi ve Karakterizasyonu.
38. Miyayama, M., Katsuta, S., Suenaga, Y., Yanagida, H., 1983. Electrical conduction in $\beta\text{-Bi}_2\text{O}_3$ doped with Sb_2O_3 . **Journal of the American Ceramic Society**, **66**: 585.
39. Turkoglu, O., Ari, M., Yilmaz, S., Soylak, M., Belenli, I., 2005. Synthesis and crystallographic properties of the tetragonal type $\text{Bi (III) } 2\text{-}2x\text{Ho (II)}_2x\text{O}_3\text{-}x$

solid solution. The 10th European Conference on Solid State Chemistry, Sheffield, 70

40. Miyayama, M., Yanagida, H., 1986. Oxygen ion conduction in γ - Bi_2O_3 doped with Sb_2O_3 . **Journal of Materials Science**, **21**: 1233-1236.
41. Zhereb, V. P., Skorikov, V. M., 2003. Metastable states in Bismuth-containing oxide system. **Inorganic Materials**, **39**: 121-145.
42. Good enough, J. B., 1997. Ceramic solid electrolytes. **Solid State Ionics**, **94**: 17-25.
43. Oniyama, E., Wahlbeck, P. G., 1998. Phase equilibria in the Bismuth-Oxygen system. **Journal of Physical Chemistry**, **102**: 4418-4425.
44. Turkoglu, O., Belenli, I., 2003. Electrical conductivity of γ - Bi_2O_3 - V_2O_5 solid solution. **Journal of Thermal Analysis and Calorimetry**, **73**: 1001-1012.
45. Fruth, V., Popa, M., Berger, D., Ionic a, C. M., Jitianu, M., 2004. Phases investigation in the Antimony doped Bi_2O_3 system. **Journal of European Ceramic Society**, **24**: 1295-1299.
46. Turkoglu, O., Altiparmak, F., Belenli, I., 2003. Stabilization of Bi_2O_3 polymorphs with Sm_2O_3 doping”, **Chem. Pap.**, **57** (5): 304-308.
47. Turkoglu, O., Soylak, M., Belenli, I., 2002. Synthesis and characterization of β type solid solution in the binary system of Bi_2O_3 - Eu_2O_3 . **Bulletin Material Science**, **25**: 583-588.
48. Turkoglu, O., Gumus, A., Belenli, I., 1998. Synthesis of Bi_2O_3 polymorphs doped with V_2O_5 . **Balkan Physics Letters**, **6**: 34-40.
49. Jia, Y. Q., 1991. Crystal radii and effective ionic radii of the rare earth ions. **Journal of Solid State Chemistry**, **95** (1): 184-187.
50. Shannon, R. D., Prewitt, C. D., 1969. Effective ionic radii in oxides and fluorides. **Acta Crystallographica**, **B25**: 925-946.
51. Takahashi, T., Iwahara, H., Nagai, Y., 1972. High oxide ion conduction in sintered Bi_2O_3 containing SrO , CaO or La_2O_3 . **Journal of Applied Electrochemistry**, **2**: 97-104.

52. <http://www.webelements.com/webelements/elements/text/ky.html> (Erişim: Eylül 2017).
53. <http://www.americanelements.com/hooxst.html> (Erişim: Eylül 2017).
54. [http://www.webelements.com/webelements/compounds/text/Ho/Ho₂O₃- 12055628.html](http://www.webelements.com/webelements/compounds/text/Ho/Ho2O3-12055628.html) (Erişim: Eylül 2017).
55. <http://www.metall.com> (Erişim: Eylül 2017).
56. Catherine E. Housecroft; Alan G. Sharpe (2008), "Chapter 25: The f-block metals: lanthanoids and actinoids". **Inorganic Chemistry**, 3rd Edition. Pearson. P.864. ISBN 978-0-13-175553-6
57. <https://www.webelements.com/compounds/dysprosium/didysprosium-trioxide.html> (Erişim: Eylül 2017).
58. Curzon, A. E., & Chlebek, H. G. (1973). The observation of face centred cubic Gd, Tb, Dy, Ho, Er and Tm in the form of thin films and their oxidation. **Journal of Physics F: Metal Physics**, 3(1), 1.
59. Verkerk, M. J., & Burggraaf, A. J. (1981). High Oxygen Ion Conduction in Sintered Oxides of the Bi₂O₃-Dy₂O₃ System. **Journal of the Electrochemical Society**, 128(1), 75-82.
60. Takahashi, T., Iwahara, H., & Nagai, Y. (1972). High oxide ion conduction in sintered Bi₂O₃ containing SrO, CaO or La₂O₃. **Journal of Applied Electrochemistry**, 2(2), 97-104.
61. J. M Amarilla and R. M Rojas, Chem. Mater., 8 (1996): p. 401-407.
62. Abraham, F., Boivin, J. C., Mairesse, G., & Nowogrocki, G. (1990). The BIMEVOX series: a new family of high performances oxide ion conductors. **Solid State Ionics**, 40, 934-937.
63. Yan, J., & Greenblatt, M. (1995). Ionic conductivities of Bi₄V_{2-x}M_xO_{11-x} (M= Ti, Zr, Sn, Pb) solid solutions. **Solid State Ionics**, 81(3-4), 225-233.
64. Gheno, S. M., Pimentel, V. L., Morelli, M. R., & Paulin Filho, P. I. (2013). Analysis of Influence of Voltage on Potential Barrier on BiCuVOX and BiTiVOX Ceramics. **Microscopy and Microanalysis**, 19(3), 688-692.

65. Kant, R., Singh, K., & Pandey, O. P. (2009). Ionic conductivity and structural properties of MnO-doped Bi₄V₂O₁₁ system. ***Ionics***, **15**(5), 567-570.
66. Ravi Kant, K. Singh and O. P. Pandey, *Solid State Ionics*, **16** (2010): p. 277-282.
67. F. Krok, I. Abrahams, M. Malya, W. Bogusz and J. A. G Nelstrop, ***Solid State Ionics***, **3** (1997): p. 237.
68. Srikant Ekhelkar and G. K Bichile, *Bull Mater Sci.*, **27** (2004): p. 22.
69. I. Abrahams, A. J Bush, S. C. M. Chan, F. Krok and W. Wrobel, *J. Mater. Chem.*, **11** (2001): p. 1715-1721.
70. M. J. Verkerk and A. J. Burggraaf, *J. Electrochem. Soc.*, **128** (1981): p. 75-82.
71. I. De Meaza, J. P Chapman, F. Mauvy, J. I. De Larramendi, M. I. Arriortua and T. Rojo, *Mater. Res. Bull.*, **39** (2004): p. 1841-1847.
72. Jovalekić, Č., Zdujić, M., Poleti, D., Karanović, L., & Mitrić, M. (2008). Structural and electrical properties of the 2Bi₂O₃·3ZrO₂ system. ***Journal of Solid State Chemistry***, **181**(6), 1321-1329.
73. Sood, K., Singh, K., & Pandey, O. P. (2010). Synthesis and characterization of Bi-doped zirconia for solid electrolyte. ***Ionics***, **16**(6), 549-554.
74. Jun-Young Park, Heesung Yoon and Eric D. Wachsman, *J. Am. Ceram. Soc.*, **88**(9) (2005): p. 2402-2406.
75. Zdujić, M., Poleti, D., Jovalekić, Č., & Karanović, L. (2009). Mechanochemical synthesis and electrical conductivity of nanocrystalline δ-Bi₂O₃ stabilized by HfO₂ and ZrO₂. ***Journal of the Serbian Chemical Society***, **74**(12), 1401-1411.
76. Ng, S. N., Tan, Y. P., & Taufiq-Yap, Y. H. (2009). Mechanochemical synthesis and characterization of bismuth-niobium oxide ion conductors. ***J. Phys. Sci***, **20**(1), 75-86.
77. Cheng-Yen Hsieh and Kuan-Zong Fung, *J. Solid State Electrochem.*, **13** (2009): p. 951-957.

78. Wachsman, E. D., Boyapati, S., & Jiang, N. (2001). Effect of dopant polarizability on oxygen sublattice order in phase-stabilized cubic bismuth oxides. ***Ionics***, **7**(1-2), 1-6.
79. Paydar, M. H., Hadian, A. M., Shimanoe, K., & Yamazoe, N. (2002). Microstructure, mechanical properties and ionic conductivity of BICUVOX-ZrO₂ composite solid electrolytes. ***Journal of materials science***, **37**(11), 2273-2278.
80. Singhal, S. C., & Kendall, K. (Eds.). (2003). High-temperature solid oxide fuel cells: fundamentals, design and applications. Elsevier.



CURRICULUM VITAE

Name and Surname: Mustafa Aldoori

Father's Name: Neamah

Place of Birth: Iraq / Baghdad

Date of Birth: 09.11.1985

I have began in primary school in 1990 and went to the Secondary School in Iraq Diyala Governorate, then I have finished Preparatory education in 2003. After that, I have graduated from Diyala University Faculty of Science, Department of Physics in 2007. In 2015, I have taken to study of master degree in Physics Department at Erciyes University. I am a teacher currently in the Ministry of Higher Education and Scientific Research in Iraqi University

E-mail: mn_200422@yahoo.com

Tel: 0537 7337723